

INFORMATION TO USERS

This manuscript has been reproduced from the microfilm master. UMI films the text directly from the original or copy submitted. Thus, some thesis and dissertation copies are in typewriter face, while others may be from any type of computer printer.

The quality of this reproduction is dependent upon the quality of the copy submitted. Broken or indistinct print, colored or poor quality illustrations and photographs, print bleedthrough, substandard margins, and improper alignment can adversely affect reproduction.

In the unlikely event that the author did not send UMI a complete manuscript and there are missing pages, these will be noted. Also, if unauthorized copyright material had to be removed, a note will indicate the deletion.

Oversize materials (e.g., maps, drawings, charts) are reproduced by sectioning the original, beginning at the upper left-hand corner and continuing from left to right in equal sections with small overlaps.

ProQuest Information and Learning
300 North Zeeb Road, Ann Arbor, MI 48106-1346 USA
800-521-0600

UMI[®]

.

A COMPREHENSIVE STUDY OF THE RADIATED SEISMIC ENERGY

A DISSERTATION
SUBMITTED TO THE DEPARTMENT OF GEOPHYSICS
AND THE COMMITTEE ON GRADUATE STUDIES
OF STANFORD UNIVERSITY
IN PARTIAL FULFILLMENT OF THE REQUIREMENTS
FOR THE DEGREE OF
DOCTOR OF PHILOSOPHY

Xyoli Pérez-Campos
August 2002

UMI Number: 3067915

UMI[®]

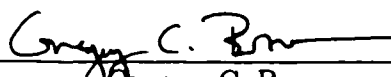
UMI Microform 3067915

Copyright 2003 by ProQuest Information and Learning Company.
All rights reserved. This microform edition is protected against
unauthorized copying under Title 17, United States Code.

ProQuest Information and Learning Company
300 North Zeeb Road
P.O. Box 1346
Ann Arbor, MI 48106-1346

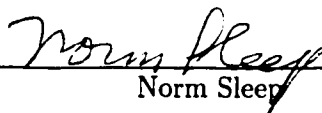
© Copyright by Xyoli Pérez-Campos 2002
All Rights Reserved

I certify that I have read this dissertation and that, in my opinion, it is fully adequate in scope and quality as a dissertation for the degree of Doctor of Philosophy.



Gregory C. Beroza
(Principal Adviser)

I certify that I have read this dissertation and that, in my opinion, it is fully adequate in scope and quality as a dissertation for the degree of Doctor of Philosophy.



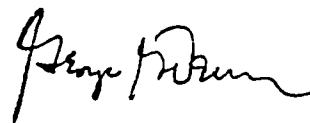
Norm Sleep

I certify that I have read this dissertation and that, in my opinion, it is fully adequate in scope and quality as a dissertation for the degree of Doctor of Philosophy.



John Boatwright
(U.S.G.S.)

Approved for the University Committee on Graduate Studies:



Abstract

Seismic energy, by itself, allows one to analyze many important characteristics of earthquakes, and the processes associated with them. These processes include how faults rupture, how waves propagate, attenuate, or disperse through the Earth, and how local conditions where an earthquake is felt or recorded affect seismic waves.

Seismic energy, one of the most fundamental parameters of earthquake size, is estimated using the whole frequency bandwidth and, in contrast to other size measurements, is concentrated at and above the corner frequency. This characteristic relates seismic energy to the damage caused by an earthquake and helps in understanding the frequency-dependent processes involved in it. However, its estimation has many uncertainties that have lead, among other difficulties, to discrepancies between estimates obtained using different data and techniques. These discrepancies have obscured previous observations about seismic energy, for example the way it scales with moment, or its dependence on focal mechanism. The aims of this work are to reduce the uncertainty of seismic energy estimations; to resolve the discrepancy between regional and teleseismic estimates; and to describe some earthquake characteristics based on improved estimates of seismic energy.

The seismic energy is only a fraction of the total energy liberated by an earthquake, but this is the only fraction that we can estimate directly from seismograms. We can use either regional or teleseismic recordings in the estimation process; however, we need to be careful on the corrections we apply. In the estimation of seismic energy from teleseismic data, I model the uncertainties in geometrical spreading, radiation pattern, and energy flux, by taking into account the uncertainties in earthquake location, focal mechanism, and corner frequency. Furthermore, I use a variance-weighting technique to estimate the total seismic energy from various stations. Working with data from Mexican subduction events I found that to reduce the observed discrepancy between regional and teleseismic estimates, a frequency-dependent site-effect correction is crucial, especially for the regional estimates. Also, I found that the teleseismic attenuation correction had to be stronger, in particular at

high frequencies (above ~ 0.3 Hz) for subduction zones. Since the site effect can overpredict seismic energy, I modelled this correction for 49 GSN stations. By using these modelled site corrections, I found that the mean value of seismic energy reduces by a factor of ~ 1.6 and its uncertainty is $\sim 4\%$ smaller.

I analyze different aspects of earthquakes using these improved teleseismic estimates of seismic energy. First, I check for a focal mechanism dependence of seismic energy; I find that the strike-slip events are ~ 3.3 times more energetic than the reverse events and ~ 1.7 times more energetic than the normal events. A controversial result from several other studies has been the scaling of seismic energy with seismic moment. Using 244 events with seismic moment between 1×10^{17} and 1×10^{22} , I observe no statistically significant scaling.

I use seismic energy to compute the apparent stress, and use these values together with the centroid time shift as a discriminant for slow earthquakes. I analyzed 70 strike-slip events, identified some with anomalously large centroid time shift given their seismic moment, and distinguished four of them that also had a low apparent stress. These events were classified as slow earthquakes, having a low content of high frequency. They occurred on ridge-ridge transform faults, which suggests a different frictional behavior for this type of fault; however, when these slow events are included in the calculation of the average apparent stress of ridge transforms, the value is not different than for other populations. I followed the same procedure for 88 shallow reverse events, including the 1992 Nicaragua tsunami earthquake as a previously recognized slow event. I conclude that the apparent stress in conjunction with the centroid time shift can be used as discriminant for slow earthquakes.

Finally, I analyzed how seismic energy is distributed on the fault, using strong ground motion rupture models. I followed *Ide's* [2002] approach to estimate the energy distribution for the 1984 Morgan Hill, the 1992 Landers, and the 1999 Hector Mine earthquakes. I observe that seismic energy is mainly released at the principal regions of high slip and that it is absorbed at the edges of these regions. The apparent stress distribution is correlated to the seismic energy distribution, having high apparent stresses at regions of high energy and negative values of apparent stress at regions of energy absorption.

Acknowledgements

First I thank Gregory C. Beroza for his great work as my advisor, always supportive and understanding. He not only guided me through my research and my life as a graduate student but he also helped me directly and indirectly to find my path in life and supported me in various aspects, especially when I needed the most.

I am also very thankful to Jack Boatwright for his helpful comments, advise, and endless chats about seismic energy. Also, to Shri K. Singh for his support and involvement in part of this project.

I thank my committee members and professors Paul Segall and Norm Sleep, who not only revised this work and gave substantial suggestions but also who taught me more about what Geophysics could be.

Special thanks to Jeff McGuire, whose interest in oceanic transform earthquakes motivated part of this work, and also to Satoshi Ide for sharing his codes with me making one of the chapters possible.

I thank my colleagues for sharing with me not only office space and seismology stuff but also good times: Eva, who is always enthusiastic and shares with me endless chats and good times; Patti, who not only explained seismology stuff that I could not understand but also inspired me to follow the statistics path; David for sharing the Schaff Syndrome with me; Martin for his great help for the development of this work and his great organization skills, Dave, Justin, and Seok Goo, great officemates.

During the time of this work, I met lots of people that I need to thank for their help, support, advise, and most important their friendship. Liliana, thanks for not only being a great roommate but for being like a sister to me. Andrés, thanks for sharing the good

and the bad times, and sharing from dawn to dusk countless anecdotes and experiences. Rolando thanks for being always there. Oscar, Bolivia, Sandra, Francisco, José Luis, and Cynthia thanks for being more than friends and becoming my Stanford family. Jorge thanks for your advise in Statistics and more important your friendship. Naser, Manuel, Gabriel, Toño, Martin, Aarón, Juan Pablo, Ramón, Edgar, Ciria, ... thanks for sharing with me great moment and cheer me up when I needed the most.

I am also very grateful to Carlos Valdés for his support and trust on me, that took me to the end of another goal. Also, thanks to my Mexican friends who from the distance always were there for me.

Financial support during my first three years at Stanford was provided by the Chamberlain, the Littlefield, the Blaustein, and the Robert G. Kirby Fellowships. My research was largely funded by the NSF Grant NSF EAR-9909479 and the NSF Grant NSF EAR-0208499. Also, I was partially supported by DGAPA-UNAM, Mexico, and the Ministry of Education of Mexico (SEP).

I thank the Pérez-Campos family for always being there for me, supporting me from the distance, making the miles between us shorter with their love. Nahúm Pérez Paz who is not only a great father but also a great example as a professional and human being. Yolanda Campos Campos, the greatest woman whose love and strength have guided my path. Nahúm Pérez Campos, best friend, and wonderful brother, and a great cushion to lean on, available at all times regardless the distance. Last but not least, Quetzalcóatl Pérez Campos, my baby brother who has taught me more life lessons than anyone else.

Contents

Abstract	iv
Acknowledgements	vi
1 Introduction	1
2 An Apparent Mechanism Dependence of Radiated Seismic Energy	15
2.1 Abstract	15
2.2 Introduction	16
2.3 Estimating Seismic Energy From Seismograms	18
2.4 Apparent Stress	21
2.5 Discussion	26
2.6 Conclusions	30
2.7 Acknowledgements	31
3 Reconciling Teleseismic and Regional Estimates of Seismic Energy	32
3.1 Abstract	32
3.2 Introduction	33
3.3 Data	35
3.4 Analysis	37
3.4.1 Site Correction	39
3.4.2 Teleseismic Attenuation	41
3.4.3 Regional Attenuation	42
3.4.4 Geometrical Spreading	42
3.5 Discussion	43
3.6 Conclusions	46
3.7 Acknowledgments	46

4	Cumulative Energy Flux: Site Effect	47
4.1	Abstract	47
4.2	Introduction	47
4.3	Data: Cumulative Seismic Energy	49
4.4	Ratio: Site Effect	50
4.5	Simulated Annealing: Best Site Effect Correction	54
4.6	Discussion	55
4.7	Conclusions	57
4.8	Acknowledgments	57
5	Apparent Stress and Centroid Time Shift: Slow Earthquakes	61
5.1	Abstract	61
5.2	Introduction	62
5.3	Large Centroid Time Shift	63
5.4	Low Apparent Stress	64
5.5	Signal Characteristics	66
5.6	Discussion	67
5.7	Tsunami Earthquakes: Slow?	72
	5.7.1 Tsunami Earthquakes: Data	73
	5.7.2 Tsunami Earthquakes: Results	73
	5.7.3 Tsunami Earthquakes: Discussion	75
5.8	Conclusions	77
5.9	Acknowledgments	77
6	Seismic Energy Distribution From Strong Motion Models: Scenarios	78
6.1	Abstract	78
6.2	Introduction	79
6.3	Energy Balance	80
6.4	Seismic Energy from Rupture Models	81
6.5	Energy Distribution: Real Earthquakes	83
	6.5.1 1984 Morgan Hill Earthquake	84
	6.5.2 1992 Landers Earthquake	86
	6.5.3 1999 Hector Mine Earthquake	92
6.6	Discussion	99

6.7	Conclusions	100
6.8	Acknowledgments	101
A	Focal Mechanism Dependence and Scaling: Revisited	102
A.1	Focal Mechanism Dependence	102
A.2	Scaling of Apparent Stress	103
A.3	Tectonic Setting	103
A.4	Discussion	106
B	Bibliography	108

List of Tables

2.1	Best Fit Results.	26
3.1	Mexican stations used in the analysis.	36
3.2	Mexican earthquakes analyzed.	36
4.1	GSN stations analyzed.	51
4.2	Velocity model for a hard rock.	55
5.1	Ridge-transform earthquakes.	63
5.2	Tsunami earthquakes.	73
A.1	Best Fit Results.	103

List of Figures

1-1	Slip weakening. Δu is the slip, D_c is the critical distance, σ_0 is the initial stress, and σ_f is the final stress, and $\Delta\sigma$ is the static stress drop, seismic energy is represented by the red area, fracture energy by the yellow area, and the heat energy by the green area.	2
1-2	Energy integration. Upper panel is the squared corrected spectrum. The thick red line is the integral path, the gray line is the true corrected spectrum. Bottom panel is the cumulative energy flux from the integration of the path described in the upper panel. The vertical blue dashed line represents the location of the corner frequency, f_0 , and the vertical magenta dashed line represents the cut-off frequency, $f_{cut-off}$ up to where the real corrected spectrum is integrated and where the extrapolation starts.	5
1-3	Slip weakening. Δu is the slip, D_c is the critical distance, σ_0 is the initial stress, and σ_f is the final stress, and $\Delta\sigma$ is the static stress drop, seismic energy is represented by the red area, fracture energy by the yellow area, and the heat energy by the green area. $\bar{\tau}$ is the average shear stress, $\hat{\tau}_k$ is the fault shear resistance, and τ_α is the apparent stress. Modified from <i>Beeler et al.</i> [2002]	7
2-1	Log ratio tests for difference in variance. Histograms show the logarithm of the ratio of the variance of E_s estimated with equation 2.4 and the variance of E_s estimated with equation 2.7. Our weighted estimates have lower variance than NEIC-weighted estimates when the log ratio is positive.	22
2-2	Comparison of seismic energy estimates, using equations 2.4 and 2.7. Histograms show the logarithm of the ratio of E_s estimated with equation 2.4 and E_s estimated with equation 2.7. There is a tendency toward positive values indicating that our estimates tend to be lower than those found using the NEIC weighting.	23

2-3	Seismic energy versus seismic moment. (left) Best fit using NEIC weighting (equation 2.4) and (right) best fit using variance weighting (equation 2.7). The solid line represents the average apparent stress, and the dashed lines indicate the 95% confidence interval for the mean. The dash-dotted lines indicate an apparent stress of 0.01, 0.1, 1.0, and 10.0 MPa. The triangles denote strike-slip events; the squares indicate reverse events; and the circles indicate normal events.	25
2-4	Best fit for average apparent stress using variance weighting. (left) Bootstrap replications for the best fit assuming a fixed slope equal to one and (right) pair-wise bootstrap replications for the best fit, varying both slope and intercept. The solid lines represent the best fit, and the dashed lines indicate the 95% confidence interval for the mean.	27
2-5	Apparent stress versus seismic moment for regional and teleseismic studies. Regional estimates are from <i>Abercrombie</i> [1995] (A95), <i>Kanamori et al.</i> [1993] (KA93), <i>Singh and Ordaz</i> [1994] (SO94), <i>Mayeda and Walter</i> [1996] (MW96), and <i>Prejean and Ellsworth</i> [2000] (PE00). Teleseismic estimates are from <i>Kikuchi and Fukao</i> [1988] (KF88), <i>Newman and Okal</i> [1998] (NO98), this study (PB01).	29
2-6	E_s teleseismic estimates versus regional estimates. The teleseismic estimates were both obtained from the NEIC catalog (solid symbols) and using variance weighting (equation 2.7) (open symbols), while the regional estimates are from regional studies [<i>Mayeda and Walter</i> , 1996; <i>Kanamori, et al.</i> , 1993]. The solid line would be followed if both estimates were equal. The dashed line indicates that the regional estimates are 10 times larger than the teleseismic estimates.	31
3-1	Regional estimates of seismic energy vs teleseismic estimates. The open symbols represent strike-slip events; the black symbols, reverse events; and the gray symbols, normal events. The regional estimations were obtained from <i>Mayeda and Walters</i> [1996] and <i>Kanamori et al.</i> [1993], and the corresponding teleseismic values were obtained from the NEIC catalog. For the Mexican events, the regional values were calculated using the technique outlined by <i>Singh and Ordaz</i> [1994], and the teleseismic values using the technique described by <i>Pérez-Campos and Beroza</i> [2001]. . . .	34

3-2	Teleseismic attenuation model. The gray dashed line is the original attenuation model (Equation 3.5) from <i>Choy and Cormier</i> [1986]; the gray solid line is the model described by equation (3.7); the black dashed line is given by equation (3.5) plus a $\Delta t^* = 0.17$; and the black dashed line is the preferred model, expressed by equation (3.7) plus a $\Delta t^* = 0.17$	38
3-3	Difference between the regional and teleseismic source spectra. The gray lines represent the ratio between the regional and the teleseismic source spectra after applying the site effect correction. The black lines represent the same ratio after applying the preferred corrections. The thick lines in the top panel represent the 95% confidence interval for the mean of the ratios. The ratios have been smoothed using a loess function [<i>Cleveland, 1993</i>].	40
3-4	Regional vs teleseismic estimates of seismic energy for the Mexican earthquakes. The open symbols are the original values, obtained using the corrections given by equations (3.3), (3.4), and (3.5) and without applying any site effect correction. The green dashed arrows represent the site effect for the regional estimates and the red dashed arrows represent the attenuation effect for the teleseismic estimates. The filled symbols are the values after applying the preferred corrections. The number next to the symbol corresponds the event number on Table 3.2. The black solid arrows represent the total effect after applying the preferred corrections to both regional and teleseismic estimates.	44
3-5	Measure of discrepancy. The squares are for the original estimates; the circles are after applying the site effect correction; and the triangles are after applying all the preferred corrections. The open symbols are the difference for each event and the filled symbols are the mean of the difference. The solid line represents that the estimates from regional and teleseismic data are equal.	45
4-1	Location of Global Seismic Network (GSN) stations analyzed.	49
4-2	Hard-rock site correction [<i>Boore and Joyner, 1997</i>]. The velocity model used for the amplification calculation is given on Table 4.2 and κ was assumed to be 0.01.	52
4-3	Distribution of log-ratio before site correction. Each plot represents a station. The horizontal black line represents the median of the distribution and the black dashed lines represent the 5% and 95% of the distribution. The horizontal green dashed line represents a good agreement between the cumulative energy estimates.	53

4-4	Density (dashed lines) and velocity (solid lines) models. The thin green lines represent the initial model (hard rock) and the black thick lines represent the final model. Each plot represents a station.	56
4-5	Site effect. The green lines represent the squared ratio of equation (4.1), after including the site correction modelled (Figure 4-4), and equation (4.2), and the thick black lines represent the modelled site correction. The red dashed lines represent no site effect. Each plot represents a station.	58
4-6	Distribution of log-ratio after applying the modelled site correction. Each plot represents a station, the number of the station corresponds to the one listed on Table 4.1. The horizontal black line represents the median of the distribution and the black dashed lines represent the 5% and 95% of the distribution. The horizontal green dashed line represents a good agreement between the cumulative energy estimates.	59
4-7	Log-ratio distribution. The thick solid lines represent the mean log ratio, the thick dashed lines are the one standard deviation of the mean, and the thin dashed lines represent the values of E_s are equal. The number on the left is the percentage of events (per station) that are under estimated. The top panel is the ratio between the cumulative energy before site correction, the middle panel is after a generic hard-rock correction, and the bottom panel is after the modelled site correction. .	60
5-1	Scaling of centroid time shift with moment. The outlined symbols are the events identified as slow. The events are color coded based on their apparent stress, where red is high τ_α and blue is low τ_α . Those events with high Δt given their M_0 are labelled with their source region.	64
5-2	Moment normalized centroid time shift vs apparent stress. Triangles are for continental earthquakes; squares are for oceanic events, excluding those at ridge or rise transforms, which are given on circles; the outlined symbols are for the identified slow events. The symbols are color coded proportional to the seismic moment of the event. The solid lines represent the best fit for the respective population and the dashed line is the $\sim 95\%$ confidence intervals of the regression. The thin red lines are for the continental events; the thin blue lines are for the oceanic events excluding the ridge and rise transforms; and the thick dark blue lines are for the ridge and rise transform events, including the slow events.	66

5-3	Options for having a long centroid time shift. The panels on the left are on the time domain and the right panels are in the frequency domain. The centroid time shift is larger for the multiple and the slow event in contrast to the regular event, but the corner frequencies are different, being $fc_1 \approx fc_2 \gg fc_3$. This is assuming an omega-square model for the spectral decay [Aki, 1967].	68
5-4	Location of the two events on the Owen fault and the location of station ATD. . .	69
5-5	The top panel is the comparison of the smoothed source spectrum of the slow event (black) and the regular event (gray) and the bottom panel compares the accumulation of the seismic energy released by each event with respect to frequency. The smoothed spectra were obtained using a loess function, with a linear interpolation for a 0.5 neighborhood parameter [Cleveland, 1993].	70
5-6	Comparison of the slow event (thick black line) and the regular event (thin gray line) at the same station ATD. The left panels are the time domain signals and the right panels are the cumulative seismic energy with frequency. The top panels are the original signals, then after applying a low pass filter at 2 seconds, at 10 seconds and at 20 seconds at the bottom. The original signals are aligned at the arrival times.	71
5-7	Scaling of centroid time shift with moment for shallow reverse earthquakes. The outlined symbols are events identified in the literature as tsunami earthquakes. The events are color coded based on their apparent stress, where red is high τ_a and blue is low τ_a	74
5-8	Moment normalized centroid time shift vs apparent stress. The outlined symbols are for the tsunami events. The symbols are color coded proportional to the seismic moment of the event. The solid lines represent the best fit for the respective population and the dashed line is the $\sim 95\%$ confidence intervals of the regression.	75
5-9	Moment normalized centroid time shift vs apparent stress for tsunamigenic earthquakes. The outlined symbols are for the tsunami events. The symbols are color coded proportional to the tsunami magnitude [Iida et al, 1967]. The solid lines represent the best fit and the dashed line is the $\sim 95\%$ confidence intervals of the regression.	76
6-1	Domains of integration for the energy balance.	80
6-2	Slip-weakening model. The gray area represents the energy released as seismic waves by an earthquake.	82

6-3	1984 Morgan Hill earthquake. The top panel is the moment density distribution, the center panel is the static stress drop distribution, and the bottom panel is the apparent stress distribution.	85
6-4	1984 Morgan Hill earthquake. The radiated energy density (bottom panel) can be obtained by summing the potential energy change (upper panel) with the energy loss density (middle panel).	87
6-5	1992 Landers earthquake, Johnson Valley Fault segment. The top panel is the moment density distribution, the center panel is the static stress drop distribution, and the bottom panel is the apparent stress distribution.	89
6-6	1992 Landers earthquake, Homestead Valley Fault segment. The top panel is the moment density distribution, the center panel is the static stress drop distribution, and the bottom panel is the apparent stress distribution.	90
6-7	1992 Landers earthquake, Camp Rock-Emerson Fault segment. The top panel is the moment density distribution, the center panel is the static stress drop distribution, and the bottom panel is the apparent stress distribution.	91
6-8	1992 Landers earthquake, Johnson Valley Fault segment. The radiated energy density (bottom panel) can be obtained by summing the potential energy change (upper panel) with the energy loss density (middle panel).	93
6-9	1992 Landers earthquake, Homestead Valley Fault segment. The radiated energy density (bottom panel) can be obtained by summing the potential energy change (upper panel) with the energy loss density (middle panel).	94
6-10	1992 Landers earthquake, Camp Rock-Emerson Fault segment. The radiated energy density (bottom panel) can be obtained by summing the potential energy change (upper panel) with the energy loss density (middle panel).	95
6-11	1999 Hector Mine earthquake. The top panel is the moment density distribution, the center panel is the static stress drop distribution, and the bottom panel is the apparent stress distribution.	97
6-12	1999 Hector Mine earthquake. The radiated energy density (bottom panel) can be obtained by summing the potential energy change (upper panel) with the energy loss density (middle panel).	98

A-1	Best fit for average apparent stress using enhance teleseismic technique. (left) Bootstrap replications for the best fit assuming a fixed slope equal to one and (right) pair-wise bootstrap replications for the best fit, varying both slope and intercept. The solid lines represent the best fit, and the dashed lines indicate the 95% confidence interval for the mean.	104
A-2	Continental vs Oceanic. (left) Best fit for continental earthquakes. (right) Best fit for oceanic earthquakes. The solid lines represent the best fit, and the dashed lines indicate the 95% confidence interval for the mean.	105
A-3	Shallow vs Intermediate. (left) Best fit for shallow earthquakes (depth ≤ 30 km). (right) Best fit for intermediate depth earthquakes (depth between 30 and 70 km). The solid lines represent the best fit, and the dashed lines indicate the 95% confidence interval for the mean.	106
A-4	Tectonic Setting. The solid lines represent the best fit, and the dashed lines indicate the 95% confidence interval for the mean.	107

Chapter 1

Introduction

Earthquakes are one of the most devastating natural hazards producing costly damage and human fatalities. It is the task of a seismologist to understand and describe their behavior with the ultimate goal of preventing destruction and losses of life. An earthquake needs to be described from its source, through the path the seismic waves follow, to the site where it is registered or felt. In this study, I explain some earthquake characteristics that can be analyzed using a single source parameter: the seismic energy.

Historically, earthquake size has been measured using different magnitudes, with each of these measurements related to the largest amplitude on a wave group recorded by a seismograph, which relates them to a specific frequency. For example, the surface magnitude, M_S , is based on the amplitude of 20-second period Rayleigh waves. However, since the frequency content of earthquakes changes as a function of their size, magnitude scales can saturate for large earthquakes. A better measure of earthquake size is the seismic moment, M_0 , which has a physical interpretation since it is defined as the product of the shear modulus, the slip caused by the earthquake, and the area of the fault. It is measured as the asymptote to the zero frequency of the far-field displacement spectrum. In contrast, the seismic energy is concentrated around the corner frequency and for its estimation the whole frequency bandwidth is used. This characteristic suggests it is more closely related to the damage produced by an earthquake. It is also likely to lead to a better understanding of the processes involved in an earthquake, since some of these processes, such as attenuation, are frequency dependent.

The seismic energy is only a fraction of the total energy liberated when an earthquake occurs, but it is directly related to the stress drop and the destructive power of an earthquake. We can consider an earthquake as a running shear crack, where the energy involved

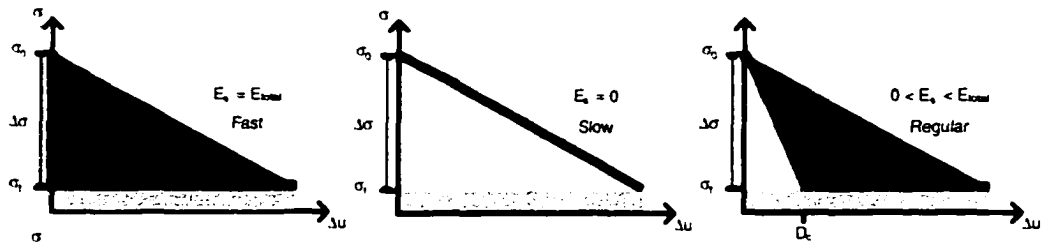


Figure 1-1: Slip weakening. Δu is the slip, D_c is the critical distance, σ_0 is the initial stress, and σ_f is the final stress, and $\Delta\sigma$ is the static stress drop, seismic energy is represented by the red area, fracture energy by the yellow area, and the heat energy by the green area.

is given by the work done by external forces, the change in internal strain energy, the surface energy involved in creation of the crack, the work done against friction, and the kinetic energy. Unfortunately, we can only measure directly from seismograms the energy radiated as seismic waves, E_s , which is proportional to the kinetic energy involved in the process [Rudinicki and Freund, 1981].

We can have two extreme cases which are represented in Figure 1-1 assuming a slip-weakening model [Ida, 1972; Andrews, 1976a; Andrews, 1976b; Day, 1982] where we can represent how energy is partitioned depending on the friction law that regulates the fault rupture. The first one (left panel of figure 1-1) occurs when the stress drops instantaneously, producing all the energy radiated as seismic waves. The second case occurs when the stress drops slowly (e.g. creeping) (middle panel of figure 1-1) having no radiated seismic energy. A third, intermediate case, is shown in the right panel.

The first attempts to estimate the seismic energy were based on empirical relations with magnitude [Gutenberg and Richter, 1942; Gutenberg and Richter, 1956]. They assumed a point source for earthquakes in California and a spherically symmetric earth where the radiation was equal in all directions, neglecting absorption and assuming a constant seismic velocity for the crust. The seismic energy was then estimated from the squared ratio between the maximum amplitude and the duration of the pulse, leading to a relationship between seismic energy and local magnitude. However, these studies recognized that the magnitude was not a complete description of ground motion. With improvements of seismic networks and digital recordings, seismic energy estimation was done either from modelling the source time function [e.g. Kikuchi and Fukao, 1988] or from the direct integration of the squared velocity seismograms, in the time domain [e.g. Kanamori, et al., 1993] or the frequency

domain [e.g. *Boatwright and Choy*, 1986].

Attempts to estimate the seismic energy have been made based on integration of the squared modelled moment-rate function. For example, *Haskell* [1964] and *Haskell* [1966] used a ramp time function of finite duration, and *Vassilou and Kanamori* [1982] used a symmetric trapezoidal far-field time function. *Shoja-Taheri and Anderson* [1988] estimated the seismic energy for the 1978 Tabas, Iran, earthquake using accelerograms within 350 km from the source to model synthetic velocity seismograms following *Haskell* [1964] and then integrated the squared synthetic seismograms. *Kikuchi and Fukao* [1988] used the far-field long-period *P* waves to estimate the time history of faulting at the source, describing the earthquake as a sequence of point dislocations with the same fault mechanism and the same source time function. With this source description and assuming a trapezoidal source time function, they estimated low values of seismic energy relative to other studies, which might be related to the bandlimited nature of their data. *Mayeda and Walter* [1996] used Coda waves from regional broadband records, corrected for path and site effects, to estimate the moment-rate spectrum, extrapolating it to lower frequencies using the seismic moment, and to higher frequencies using an omega-square fall-off, then estimating the seismic energy from this moment-rate spectrum.

Seismic energy can also be estimated from the direct integration of seismograms. In this case, investigators have used data from teleseismic distances (between 30 and 90°) or regional stations (distances < 1000 km). Teleseismic studies include *Boatwright and Choy* [1986], who used the teleseismic *P* wave group, assuming that when estimating the energy flux, the direct and depth phases add incoherently, leading to a generalization of the radiation pattern coefficient. The measurements of energy flux are then corrected by attenuation and the frequency band of the recording. *Smith et al.* [1989] constructed the attenuation-corrected far-field spectra for some moderate earthquakes, using the moment to include the low frequencies and near-source recording at high frequencies to minimize attenuation effects. They also used a correction for site effect. *Boatwright and Choy's* [1986] formalism was followed by *Newman and Okal* [1998] who assumed that neither the depth nor the focal geometry of the source was known accurately, using a distance-dependent focal mechanism correction. *Pérez-Campos and Beroza* [2001] also followed the *Boatwright and Choy* [1986] technique, assuming uncertainty in the location, and focal geometry of the source, but in this case, the uncertainty was included using variance-weighted least squares, reducing a possibly biased overestimate due to a low radiation pattern coefficient produced

by station, close to a nodal plane. Teleseismic estimates are particularly useful for large earthquake, for which regional records are often saturated.

To estimate the seismic energy, for small earthquakes, the attenuation of seismic waves requires regional or local records. *Thatcher and Hanks* [1973] used S -wave data from Southern California earthquakes with a wide range of local magnitudes ($2 \leq M_L \leq 7$). They computed the seismic energy from integration of the body-wave spectrum. The spectra were corrected for both attenuation and instrument response. *Bolt* [1986] used regional data to estimate the energy flux in the time domain for six California earthquakes. *Cocco and Rovelli* [1989] integrated the square of the corrected ground velocities in the time domain for earthquakes in Italy, using regional recordings for S waves. *Kanamori et al.* [1993] used broadband regional S wave train data for earthquakes in Southern California, they integrated the squared ground-motion velocity corrected for attenuation and station effects, assuming a point source and an average radiation pattern for all stations. *Singh and Ordaz* [1994] used the regional S wave train for shallow, thrust Mexican subduction zone earthquakes. They neglected stations with large site effects, and ignored the P waves as they contained only 4% of the total seismic energy. They considered that the point-source far-field assumption was valid and ignored the radiation pattern and directivity. *Abercrombie* [1995] used the sum of the three components of P and S wave from borehole data, assuming four source models based on the omega-square model, and integrated the squared velocity spectra of earthquakes in Southern California. *Prejean and Ellsworth* [2001] calculated E_s using both P and S waves from borehole data in the Long Valley Caldera, California. *Shi et al.* [2000] used the root mean square of Lg wave ground velocity to estimate the energy flux, assuming a circular fault, where the rupture begins at the center and grows symmetrically with a constant rupture velocity.

Figure 1-2 shows an example of how the integration of the squared corrected spectrum is performed in this thesis. After applying corrections for attenuation and site effect, I select a cut-off frequency, $f_{cut-off}$, up to which I integrate over the true spectrum. Beyond this frequency, I integrate over an extrapolation of an omega-squared model [Aki, 1967]. This extrapolation avoids problems with the noise present at high frequencies, while still including the energy thought to be present at high frequency, avoiding an underestimation of the seismic energy as discussed by *Ide and Beroza* [2002]. This effect can be more drastic for small earthquakes for which the corner frequency is high and close to the frequency range above which noise predominates.

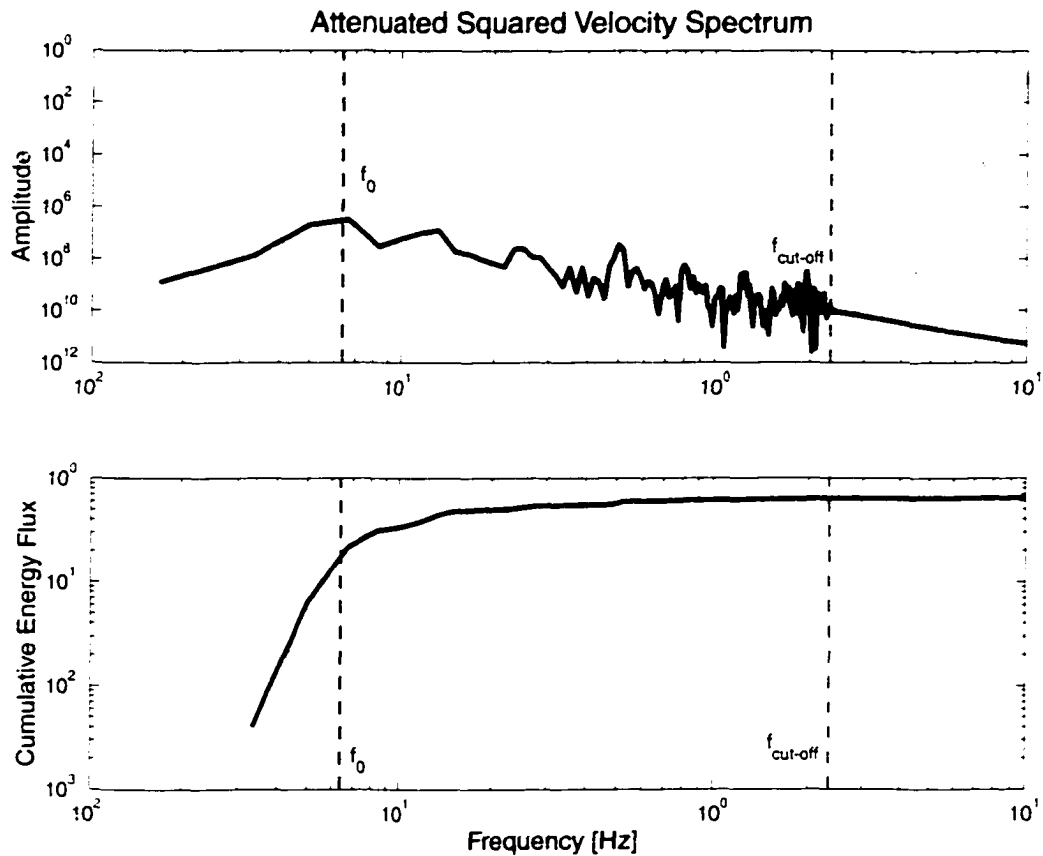


Figure 1-2: Energy integration. Upper panel is the squared corrected spectrum. The thick red line is the integral path, the gray line is the true corrected spectrum. Bottom panel is the cumulative energy flux from the integration of the path described in the upper panel. The vertical blue dashed line represents the location of the corner frequency, f_0 , and the vertical magenta dashed line represents the cut-off frequency, $f_{cut-off}$ up to where the real corrected spectrum is integrated and where the extrapolation starts.

The total seismic energy will be given by the sum of the P -wave energy and the S -wave energy. As described in the previous paragraphs, some studies only used either the P - or the S -wave group. For those using only S waves, the difference between the total energy and the estimated energy will be a minimum since about 95% of the seismic energy is radiated as S waves. However, those studies using the P -wave group needed to use a correction factor that takes into account the relative proportion of the total energy and the P waves. In this respect, *Boatwright and Fletcher* [1984] estimated the ratio of the total S -wave energy to the P -wave energy, both from integrating the velocity power spectra and for the average corner

frequency shift. From the first method, they obtained values of 27.4 ± 3.3 and 23.7 ± 3.0 ; from the second method, they got 13.7 ± 7.3 . Later, *Boatwright* [1985] estimated this ratio as 14.7 ± 2.2 from aftershocks of the Borah Peak earthquake, and *Boatwright and Choy* [1986] used a value of 15.6 which corresponds to 1.5 times the ratio between normalized rms pulse energies of the *P*- and *S*-waves. 15.58 is the value of the ratio preferred by the National Earthquake Information Center (NEIC) and assumed in this work.

There has been a large uncertainty in seismic energy estimates. Depending on the earthquake and the network conditions, high quality records at teleseismic distances or at regional or local distances are not always available. Discrepancies between estimates obtained using different techniques of up to an order of magnitude are commonly observed [*Singh and Ordaz*, 1994], leading to different conclusions regarding earthquake characteristics. For example, some authors, such as *Kanamori et al.* [1993], *Abercrombie* [1995] or *Prejean and Ellsworth* [2001], have reported scaling of the seismic energy with seismic moment, which would imply a different behavior between small and large earthquakes; however, other studies, such as *Ide and Beroza* [2001] and *Pérez-Campos and Beroza* [2001], have reported no clear scaling. These differences emphasize the importance of reconciling the discrepancy between the estimates from different data and techniques and the need to characterize and reduce the uncertainty in the estimates.

In this work I will not only attempt to reconcile the discrepancy between estimates obtained at teleseismic and regional distances, but also, I will seek to reduce the uncertainty in the seismic energy estimate. The resulting techniques will produce a more accurate estimate that will allow us to reach conclusions regarding earthquake behavior with more confidence.

An important source parameter that will tell us how energetic the earthquake was relative to its size is the apparent stress, which is related to the stress drop. The apparent stress, τ_a , is the rigidity modulus, μ , times E_s , divided by M_0 , so in order to have an accurate apparent stress estimate we need to improve the estimates of the seismic energy. Since earthquakes that are more energetic are also likely to be more destructive [*Boatwright et al.*, 2002], this parameter can help evaluate earthquake hazard.

Figure 1-3 shows a representation of the apparent stress assuming a slip-weakening model. The apparent stress is the difference between the average shear stress and the fault shear resistance [*Mori et al.*, 2000]. The average stress is given by the average of the initial and the final stresses. The difference between them gives the static stress drop. The amount

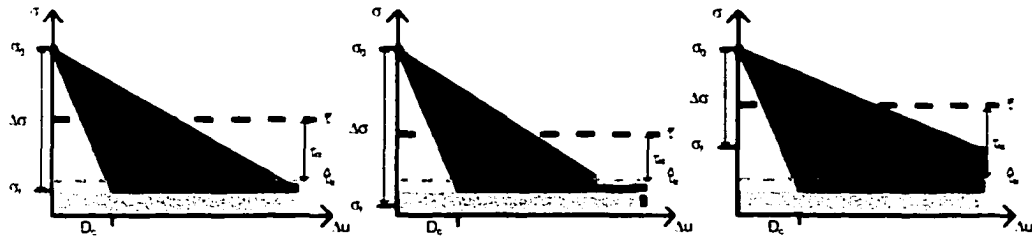


Figure 1-3: Slip weakening. Δu is the slip, D_c is the critical distance, σ_0 is the initial stress, and σ_f is the final stress, and $\Delta\sigma$ is the static stress drop, seismic energy is represented by the red area, fracture energy by the yellow area, and the heat energy by the green area. $\bar{\tau}$ is the average shear stress, τ_k is the fault shear resistance, and τ_α is the apparent stress. Modified from *Beeler et al.* [2002]

of seismic energy released will depend on the frictional behavior of the fault. According to the slip-weakening model there are three possible cases: the Orowan model [*Orowan*, 1960] (left panel of Figure 1-3), where after reaching a critical distance the stress remains constant; an overshoot model (middle panel of Figure 1-3), where the stress remains constant after a critical distance but then it drops further; and an undershoot model (right panel of Figure 1-3), which is opposite to the previous case the stress increases.

This thesis includes five chapters that develop improvements in seismic energy estimation and describe how these developments illuminate some aspects of earthquake behavior. In chapter 2, I improved the teleseismic estimation to avoid bias due to the outliers, which might result from radiation pattern effects. This technique allows us to determine whether previously reported mechanism dependencies of seismic energy are real or artifacts. Chapter 3 reconciles the teleseismic and regional estimates of seismic energy for a set of shallow and intermediate depth earthquakes in Mexico, finding the need for calibration of the teleseismic attenuation operator and highlighting the importance of the site effect. In Chapter 4, I investigate further the site effect at the teleseismic stations, obtaining the site corrections for 49 Global Seismic Network (GSN) stations. Failure to include the site effect usually produces an over prediction in the seismic energy, and by applying this correction we reduce the uncertainty in the E_s estimate at a single station by $\sim 4\%$. In chapter 5, I used all the enhancements from previous chapters in the teleseismic estimation, to calculate τ_α and by comparing it with the centroid time shift (centroid time minus origin time) I identify four "slow" earthquakes that originated on oceanic ridge-transform faults, from a dataset of 70 shallow strike-slip events. Also, from 88 shallow reverse events, one tsunami earthquake was

identified as slow earthquake. The tsunami earthquakes are those that generate a tsunami larger than predicted [Kanamori, 1972]. Finally, in chapter 6, from a rupture model and following Ide [2002], I estimate the spatial distribution of the radiated seismic energy on the fault for the 1984 Morgan Hill, the 1992 Landers, and the 1999 Hector Mine earthquakes.

The first enhancement to the seismic energy estimation is outlined in chapter 2. I revised the teleseismic technique described by Boatwright and Choy, [1986] and use a covariance weighted least-squares technique to estimate the seismic energy using teleseismic P wave data. This technique not only overcomes the possible bias due to an over estimation produced by a low value of radiation pattern correction produced by a station located close to a nodal plane, but it also includes the uncertainty in each of the parameters involved in the seismic energy estimation, such as the earthquake location and focal mechanism, translating into uncertainties in the geometrical spreading or the radiation pattern; this technique gives less weight to outliers.

A low value of the radiation pattern is most commonly present for strike-slip events where there are more stations located close to a nodal plane in the focal sphere at teleseismic distances. Since the radiation pattern coefficient is squared and appears in the denominator, this effect could produce an over estimation on the seismic energy. Newman and Okal [1998] suggested that this bias could lead to the observation previously made by Choy and Boatwright [1995] that strike-slip events were more energetic than dip-slip events of the same seismic moment. Since the improved technique addresses this potential problem, I used it to analyze a population of 204 earthquakes around the world, recorded at teleseismic distances by GSN stations.

Comparing the mean apparent stress for the three different fault mechanisms, I observed that strike-slip earthquakes are more energetic than reverse events by an average factor of ~ 4.8 and more energetic by an average factor of ~ 1.8 than normal events. Later in Appendix A, I revise the focal mechanism dependence for a set of 244 events, using teleseismic data and the enhancements outlined in other chapters of this thesis. With these improvements, the strike-slip events are more energetic than the reverse events by a lesser factor of ~ 3.3 and ~ 1.7 than normal events. The reduction in the difference between the strike-slip events and the reverse events is mostly a result of the different teleseismic attenuation correction for subduction zones.

The scaling of the apparent stress with seismic moment has been reported by various authors using regional data [Kanamori, et al., 1993; Abercrombie, 1995; Prejean and

Ellsworth, 2001]. On the other hand, other authors, have reported no resolvable scaling [*Pérez-Campos and Beroza, 2001*]. *Ide and Beroza [2001]* also reported that the scaling observed for small earthquakes by other authors might be the result of the bandlimited spectrum used for the seismic energy estimation, and when correcting for this, they observed no scaling of the apparent stress with moment. I also explore this issue, in chapter 2. In my case, the velocity spectrum used was extrapolated to high frequencies using an omega-squared model [*Aki, 1967*]. I conclude that there is no statistically significant scaling. However, the large discrepancy between estimates of seismic energy for the same event [*Singh and Ordaz, 1994*], adds some uncertainty to the significance of this discrepancy. Later in Appendix A, I revisit this result, finding again no statistically significant scaling.

Furthermore, in Appendix A, using an average shear modulus of 30,000 MPa, I compared the mean apparent stress for continental ($0.97+0.35/-0.25$ MPa) versus oceanic earthquakes ($0.82+0.21/-0.17$ MPa), and observed no significant difference between them. Also, I divided the events according to their hypocentral depth, those shallower than 35 km and those deeper; despite the difference in the mean values $0.87+0.17/-0.15$ MPa and $0.49+0.24/-0.16$ MPa respectively, the two populations are not significantly different. When comparing the mean apparent stress of different tectonic settings: subduction ($0.77+0.21/-0.16$ MPa), continental collision ($1.29+5.46/-1.04$), ridge and rise ($0.96+1.22/-0.54$ MPa), interplate ($1.01+0.41/-0.29$ MPa), and intraplate ($1.12+3.12/-0.82$ MPa); despite the previous result of focal mechanism dependence, the populations are statistically indistinguishable from each other. This is the result of including different mechanisms when estimating the average apparent stress for each tectonic setting.

As mentioned previously, estimates of seismic energy differ depending on the technique used. With the goal in mind of reconciling the discrepancy between teleseismic and regional estimates, in chapter 3, I explore the estimation of seismic energy using regional *S*-wave data (following *Singh and Ordaz [1994]*), and using teleseismic *P*-wave data (as described in chapter 2).

The discrepancy has been observed through all tectonic settings and fault mechanisms. To resolve it we need to use well-recorded events, both at regional and teleseismic distances. Mexico has experienced earthquakes that have produced costly damage and left thousands of people dead or homeless. Due to the hazards posed by earthquakes, Mexico maintains a 300 station accelerograph network. I used nine earthquakes in the Mexican subduction zone that were well recorded at both teleseismic and regional distances. Three of these were shallow

reverse-faulting earthquakes and the other six were intermediate-depth, normal-faulting earthquakes within the subducting Cocos-North America plate boundary. For the regional estimation I only used those stations that were located on rock sites and disregarded those stations that are known to have strong site effect.

Since the seismic energy can be calculated from the squared velocity spectrum, as described in chapter 2, we can compare corrected velocity spectra obtained with different data and using different corrections. As shape and amplitude of the spectra get closer to each other, the seismic energy estimations will get closer too. This analysis allowed me to check for a frequency dependent correction that can be due to attenuation, geometrical spreading, or site effect.

From this analysis, I conclude that it is important to include a site correction when estimating the seismic energy. In this case, despite the selection of stations located on rock sites, the regional stations are more strongly affected by site amplification than the teleseismic ones. The site correction usually leads to an over prediction of the seismic energy, because ground motions are typically amplified. This site effect is the result of the upper crust close to the station, which points out the importance of having a good velocity model of the station region.

Another correction that has to be calibrated is the teleseismic attenuation, especially at high frequencies (above 0.3 Hz). I concluded in chapter 3 that the teleseismic attenuation needs to be chosen according to the source region based on the agreement accomplished by *Boatwright et al.* [2002] for the 1999 Hector Mine earthquake using a different attenuation model than in this work, and the observation from *Boatwright and Choy* [1989] of a stronger attenuation for subduction zones.

As found in chapter 3, correction of the site effect at the station is needed for an accurate value of E_s . This correction is especially problematic for studies using a single station or when only few stations are available. While routine cataloging of source parameters requires techniques that are fast and simple, it is important to realize that using a generic correction may lead to a greater uncertainty if only few stations are used.

Previous works have estimated the site effect, mostly using the Horizontal-to-Vertical (H/V) ratio [e.g. *Atkinson*, 1993, *Lermo and Chávez-García*, 1993, *Theodulidis et al.*, 1996, *Huang and Teng*, 1999, *Yuncha and Luzon*, 2000, and *Chen and Atkinson*, 2002]. Others, such as *Ordaz et al.* [1988] have used the ratio between stations located at soft sediments and a station on a rock site. However, in chapter 4, I use the ratio of the cumulative seismic

energy with respect to frequency of each event at the station before site correction, and after applying a generic correction. This ratio allows me to delineate frequency dependent differences, which might reflect source, path, or site effects. From this analysis I identify a frequency dependent discrepancy, starting at around a frequency of 0.3 Hz, clearly pointing to a site effect.

Using the square root of this ratio as the site effect, and employing a simulated annealing technique, I modelled a site effect correction for 49 GSN stations. For those stations that consistently over predict E_s , the site correction leads to them over- or under-predicting it half the time, reducing the mean E_s by a factor of ~ 1.6 . Also, in general, it slightly reduces the uncertainty in the E_s estimate at a single station by about $\sim 4\%$. This uncertainty is not reduced significantly since the distribution of a particular station was only corrected to be centered at zero; i.e., to equally over- or under-predict E_s .

After including all the enhancements mentioned in chapters 2, 3, and 4, in chapter 5, I used teleseismic data to estimate the seismic energy for a global dataset of 70 strike-slip earthquakes. Various authors have observed that slow earthquakes are more common on oceanic transform faults. This observation comes from comparing different types of magnitudes for the same earthquake. *Okal and Stewart* [1982] observed discrepancies between magnitudes measured at long and short periods for events on transform faults. *Prozorov and Hudson* [1983] defined creepex as the deviation of an earthquake from the orthogonal regression of surface and body magnitudes, a positive creepex denotes similarity to the creep phenomenon. They observed a higher creepex for strike-slip earthquakes than for reverse events; furthermore, they observe high values of creepex in mid-ocean ridges. *Beroza and Jordan* [1990] detected slow earthquakes, with anomalously large characteristic durations, that were enriched in low-frequency mode excitations. Many of these occurred on oceanic transform faults. *Stein and Pelayo*, [1991] observed that transform-fault events had a larger M_S compared to their body magnitude, m_b ; also *Shearer* [1994] noticed that some transform events were anomalously strong relative to their M_S . These observations suggest that these events have released more energy at longer periods.

The term "slow earthquake" has been used for events with abnormally long duration of the rupture process. Some studies have observed a very slow rupture component of the order of 100 s for events located on ocean transforms [e.g., *Ihmlé and Jordan*, 1994; *McGuire, et al.*, 1996]. However, it has been argued that this result was dependent on the crustal structure assumed in the source region and the uncertainties in the modelling procedure

suggesting that the conclusion that earthquakes on oceanic transforms are slow needs to be re-evaluated [Abercrombie and Ekström, 2001]. In this work, I use an oceanic-crust velocity model for earthquakes originated in oceanic crust and the IASPEI 1991 velocity model [Kennett, 1991] for events originated in continental crust. Furthermore, I based my analysis of slow earthquakes in the frequency content of the event, reflected on the value of the apparent stress, as in Chapter 5.

In contrast to the findings of slow earthquakes located on ocean transforms, *Choy and Boatwright* [1995] observed that the oceanic transforms have high values of apparent stress. Most of the seismic energy comes from above and around the corner frequency, but observation that oceanic transform events are slow is based on their spectra being depleted at high frequencies, so there appears to be a contradiction.

To resolve this discrepancy, I retrieved the centroid time shift from the Harvard CMT Catalog of the 70 strike-slip earthquakes analyzed in this thesis, and computed their seismic energy and apparent stress using the technique described on chapter 2 and the corrections described on chapters 3 and 4. I observed that events with an anomalously large centroid time shift, given their seismic moment, also have a low apparent stress, and form a distinct population from the others. These four identified events are located on oceanic ridge transform faults. These events are excluded from the NEIC seismic energy analysis due to their low signal to noise ratio at ~ 1 Hz. When these slow events are included in the estimation of the mean apparent stress of the ridge-oceanic transforms, the value obtained is smaller than previously reported [*Choy and Boatwright*, 1995]. Also, this mean value is not significantly different than for populations of other tectonic settings.

A way to verify the difference in energy content with frequency is comparing two events with similar focal mechanism, moment, and location. For this purpose I analyzed how seismic energy accumulates with frequency for two events at the Owen transform fault, one slow and the other one regular, and observed that at low frequencies, up to 0.05 Hz, the seismic energy accumulates similarly for both; after that, the slow event is strongly depleted in energy. The difference between a multiple event and a slow earthquake will be well represented in the spectrum; with different corner frequency and possibly different spectral decay than observed. So, we conclude that the four events identified can be classified as slow earthquakes.

Since it has also been observed that tsunami earthquakes have a slow component and are depleted at high frequencies [Kanamori, 1972; Kanamori and Kikuchi, 1993], I also

analyzed, using the same technique and parameters, 88 shallow events with reverse mechanism in study the characteristics of known tsunami earthquakes. These are defined as earthquakes that generate tsunamis significantly larger than predicted from their magnitude [Kanamori, 1972]. Three events, previously identified tsunami earthquakes by other authors [Kanamori and Kikuchi, 1993; Newman and Okal, 1998; Abercrombie et al., 2001; Polet and Kanamori, 2000] also have both low τ_α and large Δt . However, only the 1992 Nicaragua earthquake can be classified as slow.

Finally, in chapter 6, I focus on the character of the spatial distribution of the radiated seismic energy on the fault plane. By understanding this we will be able to understand better how the fault behaves and how the seismic energy is generated at the source.

From rupture models I estimated the seismic energy distribution for three Californian earthquakes, using *Ide's* [2002] method. First, using the rupture model as a constraint, the time dependent stresses are estimated on each subfault and then used together with the slip model for the estimation of the seismic energy. The first model analyzed is for the 1984 Morgan Hill earthquake [Beroza and Spudich, 1988]. This earthquake had its largest slip concentrated far from the hypocenter. I observe that the largest amount of seismic energy radiated coincides with the largest slip and is not focused closer to the hypocenter. The second model analyzed is of the 1992 Landers earthquake [Cohee and Beroza, 1994]. This earthquake occurred along three fault segments, the Johnson Valley fault, the Homestead Valley fault, and the Camp Rock-Emerson faults. Similar to the previous event, the largest amount of energy was released from the area where the largest slip occurred, far from the hypocenter. Again, the maximum seismic energy was released from the region with the largest slip. The third event analyzed was the 1999 Hector Mine earthquake [Dreger and Kaverina, 2000]. This event also occurred on three fault segments; however, the rupture model used was projected to a single plane fault for my analysis. For this event, both the slip and the seismic energy were mostly concentrated around the epicentral region, downdip from the hypocenter. From these three events we observe similar features, previously observed by *Ide* [2002] for other events. Seismic energy is concentrated close to the hypocentral region. We also observe energy sinks at the boundaries of the asperities; however, if slip was concentrated away from the hypocentral region, the energy closely follows its distribution - being higher at the asperities and absorbed at their edges.

The total seismic energy was estimated from these models. These results in lower values than previously reported by other authors, by up to an order of magnitude, for the 1992

Landers earthquake, and as low as a factor of two, for the 1999 Hector Mine earthquake. This may be a result of the frequency resolution of the rupture modelling.

Furthermore, I analyzed the spatial distribution of the apparent stress for these earthquakes. It shows that the high slip regions present the highest values of apparent stress and negative values at their edges.

Chapter 2

An Apparent Mechanism Dependence of Radiated Seismic Energy

Pérez-Campos, X., and G.C. Beroza (2001), *J. Geophys. Res.*, **106**, 11,127-11,136.

2.1 Abstract

We develop an extension to the method of *Boatwright and Choy* [1986] for determining the radiated seismic energy E_s that accounts for factors that bias the estimate. We apply our technique to 204 events worldwide during the period 1992-1999 and find that the apparent stress is on average largest for strike-slip events (0.70 MPa), while for reverse and normal events it is significantly smaller (0.15 and 0.25 MPa, respectively). These results support the mechanism dependence of E_s reported by *Choy and Boatwright* [1995], although we find that once likely sources of bias are accounted for, the mechanism dependence is not as strong as found previously. The source of the mechanism dependence is unclear, but one possibility is that it reflects a mechanism-dependent difference in the stress drop. This hypothesis is suggested by the scaling of slip with width in large strike-slip earthquakes and makes two predictions, which could be used to test it. The first is that the discrepancy should disappear for the very largest dip-slip earthquakes as the length of the fault greatly exceeds the downdip extent. The second is that the discrepancy ought to disappear for smaller earthquakes. The first can not yet be tested due to a lack of recent, very large dip-slip earthquakes. The second is supported by the lack of mechanism dependence to E_s for smaller earthquakes. An alternative hypothesis is that the apparent mechanism dependence could result if faults are opaque during rupture, blocking seismic radiation across them [*Brune*, 1996]. This could cause radiated seismic energy to be trapped preferentially in the

crust near the source volume for dipping faults. There remains, however, a large discrepancy between estimates of E_s obtained from teleseismic versus regional data. This discrepancy indicates a problem with teleseismic and/or regional estimates of the seismic energy and must be resolved before a definite conclusion can be drawn.

2.2 Introduction

Elastic strain energy accumulates gradually for as long as thousands of years before being released suddenly, in a matter of seconds, during an earthquake. As an earthquake occurs, energy is expended in overcoming the surface energy to extend the rupture front, in work against friction as slip continues, and in seismic waves that are radiated away from the source and ultimately attenuated throughout the Earth [e.g., *Dahlen*, 1976]. It is this last component of the energy budget that is referred to as the seismic energy E_s . Attempts to measure the seismic energy date back over half a century [*Gutenberg and Richter*, 1942]; yet it remains one of the more poorly constrained source parameters. Estimates of seismic energy determined by different investigators for the same earthquake frequently differ by more than an order of magnitude [e.g., *Singh and Ordaz*, 1994; *Mayeda and Walter*, 1996].

Seismic energy estimates are based on point measurements of the energy flux under various assumptions [*Haskell*, 1964; *Thatcher and Hanks*, 1973; *Boatwright*, 1980; *Kanamori, et al.*, 1993]. The energy flux is usually calculated as an integral of the squared ground velocity with correction factors for density and the velocity of wave propagation. To relate this measurement to the total radiated energy, it must be corrected for both source excitation and propagation effects over a wide frequency range centered on the corner frequency. The inherent difficulty in making these corrections accurately is likely a major source of uncertainty in estimating E_s .

While there are very large uncertainties in the seismic energy, there are also hints that it may have interesting properties that could lead to important insights into earthquake physics. *McGarr* [1999] uses seismic energy estimates to conclude that the seismic efficiency, defined as the ratio of the radiated seismic energy to the total energy released, is quite low over the entire observable range in earthquake size. Several studies have reported that the apparent stress τ_α defined as $\tau_\alpha = \mu E_s / M_0$ [*Wyss and Brune*, 1968], where μ is the shear modulus, increases with increasing seismic moment M_0 [*Abercrombie*, 1995; *Mayeda and Walter*, 1996]. This scaling has been cited as evidence for thermally activated fault

weakening in earthquakes that experience large slip [Kanamori and Heaton, 2000]. Choy and Boatwright [1995] found that the apparent stress of strike-slip earthquakes was on average an order of magnitude larger than the apparent stress of dip-slip earthquakes. This last result is surprising in that it runs contrary to expectations based on simple notions of the state of stress in strike-slip versus reverse faulting environments [McGarr, 1984]. As pointed out by Newman and Okal [1998], however, the mechanism dependence of apparent stress may be an artifact that results from the dependence of seismic energy estimates on the inverse square of the generalized radiation pattern coefficient. Since the theoretical radiation pattern is typically much smaller for strike-slip events than for dip-slip events at teleseismic distances, it may bias estimates of E_s for strike-slip events to high values.

In this paper we present an extension to the method of Boatwright and Choy [1986] for estimating E_s that takes into account estimated uncertainties in focal mechanism, anelastic attenuation, takeoff angle, corner frequency, and spectral decay at high frequency. We perform parametric sampling to obtain empirical distributions of the energy flux, generalized radiation pattern coefficient, and geometrical spreading and use these distributions to develop a variance-weighted estimate of energy flux for each station. This in turn is used to obtain a more robust estimate of E_s .

Our technique confirms that there is bias in estimates of the seismic energy that is introduced by the radiation pattern; however, we find that the size of the bias is not nearly as large as the size of the effect reported by Choy and Boatwright [1995]. Thus we too find that the average apparent stress of strike-slip earthquakes is larger than the average apparent stress of dip-slip events.

The source of the observed mechanism dependence is not clear. Assuming it is a real effect, it may reflect a mechanism dependence to the stress drop. This hypothesis is supported by the scaling of slip versus fault width in large strike-slip earthquakes, for which stress drop appears to increase with increasing seismic moment [e.g., Mai and Beroza, 2000]. Our interpretation is clouded, however, by the large discrepancy between regional and teleseismic estimates of E_s , which typically differ by an order of magnitude. This discrepancy could indicate a shortcoming of either teleseismic or regional estimates of the seismic energy, or both. It could also arise if the inertial-detachment/opaque-fault hypothesis of Brune [1996] is correct. In this scenario, radiation from a reverse fault could be trapped in the near field rather than radiated to the far field. In any case, the source of the regional versus teleseismic discrepancy needs to be understood before possible scaling or mechanism dependence

to seismic energy can be uniquely interpreted.

2.3 Estimating Seismic Energy From Seismograms

Following *Boatwright and Choy* [1986], we calculate the seismic energy flux ε from the velocity spectrum determined at teleseismic distances as

$$\varepsilon = \frac{\rho\alpha}{\pi} \int_0^{\infty} |\dot{u}(\omega)|^2 \exp(\omega t_{\alpha}^*) d\omega, \quad (2.1)$$

where ρ is density; α is the P wave velocity, and the exponential term t_{α}^* corrects for anelastic attenuation. We use the same frequency-dependent t_{α}^* as *Choy and Boatwright* [1995] for the P wave group (P , pP , and sP waves). For those events with information about the duration of the moment rate function (MRF) (<http://www.geo.lsa.umich.edu/SeismoObs/STF.html>), we used a time window length given by the total duration of the MRF plus the difference between the travel time of the sP wave and the travel time of the P wave. For those events with no information about the MRF we used a constant time window of 30 s. In both cases, we included 15 s of taper before the P wave arrival and 15 s of taper at the end.

We correct for attenuation using a simple t_{α}^* operator. After the attenuation correction the spectrum is distorted at high frequencies where the inverse attenuation operator amplifies ground noise. We follow *Boatwright and Choy* [1986] by extrapolating the observed spectrum above a cut frequency ω_c with the spectrum of an ω^{-2} source model [*Aki*, 1967].

Following *Boatwright and Choy* [1986], we corrected the energy flux for the generalized radiation pattern coefficient F under the assumption that the phase between the different arrivals is random such that the power spectra add. We also corrected for the geometrical spreading R [*Aki and Richards*, 1980], where R in this case includes a correction for the free surface amplification coefficient [*Boatwright and Choy*, 1986]. The seismic energy estimated from a given station, i , is calculated as

$$E_{s_i}^P = 4\pi \langle F \rangle^2 \frac{R_i^2}{F_i^2} \varepsilon_i, \quad (2.2)$$

where $\langle F \rangle$ is the mean radiation pattern coefficient. F^2 is given by

$$F^2 = (F_P)^2 + (PP F_{pP})^2 + \frac{2\alpha}{2\beta} q (CSP F_{sP})^2, \quad (2.3)$$

and F_P , F_{pP} , and F_{sP} are the radiation pattern coefficients for the P wave, the pP wave, and the sP wave, respectively [Aki and Richards, 1980]; $q = 15.6$ is the assumed ratio of the total S wave to the P wave energy [Boatwright and Fletcher, 1984]; PP and SP are the reflection coefficients for the pP and sP reflections at the free surface, respectively; and C represents a correction for wave front sphericity [Boatwright and Choy, 1986]. We explored the effect of varying the factor q between 12 and 18 [Boatwright and Fletcher, 1984]. The resulting variation in energy estimates was 15%, suggesting that it is a second-order effect.

Boatwright and Choy [1986] averaged the energies for all stations as

$$E_s^P = 4\pi \langle F \rangle^2 \frac{\sum R_i^2 \varepsilon_i}{\sum F_i^2}. \quad (2.4)$$

This averaging will tend to reduce any bias introduced in the seismic energy calculation by small errors in F^2 for near-nodal stations because the ratio is taken after summation. Thus the effect of a single small value of the generalized radiation pattern coefficient in the denominator will be diminished. Equation (2.4) does not, however, take into account the error in the estimation of ε , R , and F . This can be demonstrated by the propagation of error or δ method [Rice, 1995]. If the standard deviation of $\sum R_i^2 \varepsilon_i$ and the standard deviation of $\sum F_i^2$ are large, then the difference between the true value of E_s and the expected value estimated from the right-hand side of (2.4) could be also large. In particular, E_s will be overestimated if the mean value of $\sum F_i^2$ is small. Moreover, the correlation between $\sum R_i^2 \varepsilon_i$ and $\sum F_i^2$ affects this difference, and if the correlation coefficient is negative, the variance of E_s will increase.

To correct for this, we need to account for the uncertainty in each of the parameters involved in the estimation. We express the seismic energy estimation as an inverse problem of the form

$$\mathbf{d} = \mathbf{G}\mathbf{m}, \quad (2.5)$$

i.e.,

$$\varepsilon_i = \frac{1}{4\pi \langle F \rangle^2} \left[\frac{F_i^2}{R_i^2} \right] E_s^P, \quad (2.6)$$

where the model in our case is simply a scalar quantity, the radiated seismic energy. The data are the energy flux for each station and \mathbf{G} is given by the ratio between F^2 and R^2 for each station divided by the factor $4\pi \langle F \rangle^2$. Using covariance-weighted least squares, we

estimate the seismic energy as

$$E_s^P = \mathbf{G}^{-g} \varepsilon, \quad (2.7)$$

where \mathbf{G}^{-g} is defined as

$$\mathbf{G}^{-g} = \left[\mathbf{G}^T (\Sigma_\varepsilon + \Sigma_{\mathbf{G}})^{-1} \mathbf{G} \right]^{-1} \mathbf{G}^T (\Sigma_\varepsilon + \Sigma_{\mathbf{G}})^{-1} \quad (2.8)$$

[*Tarantola and Valette, 1982*] and Σ denotes the covariance matrix. The problem with this approach is that the covariances in (2.8), which result from uncertainties in the energy flux estimation and the R and F corrections, are unknown.

We estimated the variances using parametric bootstrap resampling [*Efron and Tibshirani, 1993*] on the strike ϕ_s , dip δ , rake λ , and depth d of the event, as well as the distance Δ and azimuth ϕ between the stations and the earthquake, and the corner frequency f_o . All of them are assumed to be a linear combination of the catalog data or the value calculated and a random error that follows a normal distribution with mean equal zero and variance depending on the parameter. We used 200 resamples of these parameters to estimate the distribution for ε , R , and F :

$$\begin{aligned} \varepsilon &= f(f_o), \\ R &= f(d, \Delta), \\ F &= f(\phi, \phi_s, \delta, \lambda). \end{aligned} \quad (2.9)$$

From the resulting distributions on (2.9) we calculated the diagonal elements of the covariance matrix (the variances) for \mathbf{G} and ε and constructed Σ_ε and $\Sigma_{\mathbf{G}}$ under the assumption that uncertainties were uncorrelated, i.e., diagonal covariance matrices.

We analyzed 204 earthquakes (58 strike slip, 101 reverse, and 45 normal) recorded teleseismically by Global Seismic Network (GSN) stations. Locations of earthquakes were obtained from the National Earthquake Information Center (NEIC). Focal mechanisms were obtained from both the NEIC for those events with reported seismic energy estimates, and the Harvard moment tensor catalog (CMT) for those without. *Choy and Boatwright [1995]* reported that even though the focal mechanism solutions differ between the two catalogs, seismic energy estimates based on the different mechanisms varied by less than a factor of 2. The subset of global seismicity that we chose to analyze is not uniform. We intentionally included events that occurred in areas where focal mechanisms were diverse in order to

minimize possible source-location biases in the energy estimates.

In order to compare the stability of the energy estimates as proposed in this paper with that of the standard estimate used by the NEIC, we performed a bootstrap hypothesis test for the variance [Efron and Tibshirani, 1993]. We tested the null hypothesis using the logarithm of ratio between the variance obtained using (2.4) and the variance obtained using equation (2.7). If this quantity is positive, it means that the variance of our estimate is smaller than the variance of the estimate obtained with the NEIC weighting. We found that 50% of the strike-slip events, 57% of the reverse events, and 58% of the normal events have a higher variance using (2.4). For the entire data set, 54% of the events show lower variance (Figure 2-1). This suggests some advantage to our weighted estimate. Also, we note that there is a population of events with very high variance using (2.4) compared to that using (2.7). This suggests that estimates using (2.7) are more robust. Moreover, as discussed below, there is evidence for bias independent of a difference in variance.

Figure 2-2 shows the histograms of the logarithm of the ratio between NEIC-weighted E_s estimate determined from (2.4) and our variance-weighted E_s estimate determined from (2.7). The advantage of using (2.7) and the parametric bootstrap to estimate the seismic energy is that we include in the estimation the variability in the focal mechanism, geometric spreading, attenuation, takeoff angle, corner frequency, and decay of the spectra at high frequencies for each station. There is a clear tendency seen in Figure 2-2 for the logarithm of the ratio to be positive. That is, our estimates of seismic energy are systematically smaller than the NEIC-weighted estimates. This suggests that there is some degree of bias in the NEIC estimates. Although the effect is present for all mechanism types, the fact that the median of the distribution is higher for strike-slip events, while closer to zero for dip-slip events, indicates that small values of the generalized radiation pattern coefficients leads to estimates of E_s that are biased to be high for strike-slip events [Newman and Okal, 1998]. The bias, while clearly present, is not nearly large enough to explain the mechanism-dependent difference in the apparent stress found by Choy and Boatwright [1995]. Thus our analysis supports their finding.

2.4 Apparent Stress

Figure 2-3 shows the seismic energy estimate plotted against seismic moment, both using the NEIC weighting (Figure 2-3, left) and using our variance weighting (Figure 2-3, right).

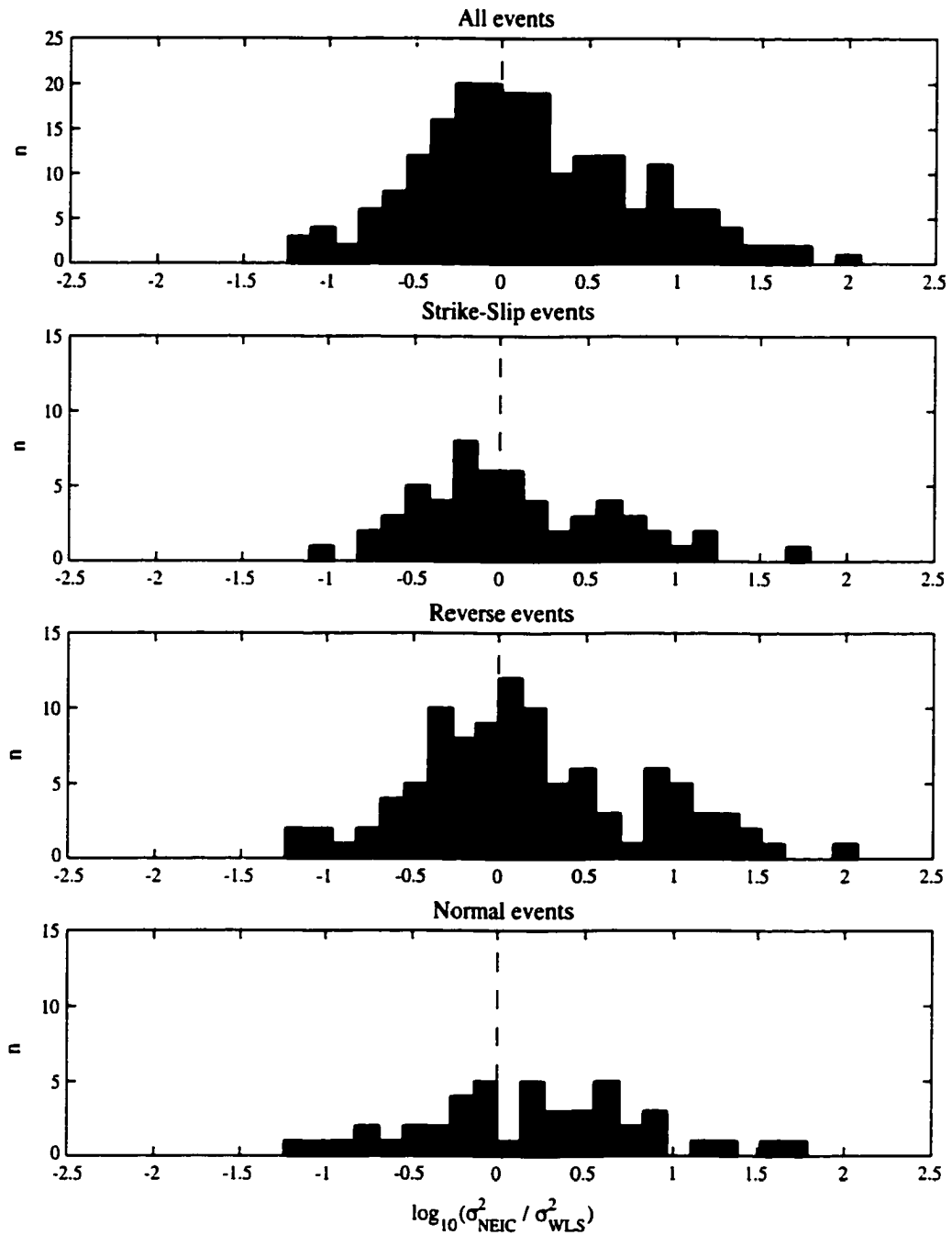


Figure 2-1: Log ratio tests for difference in variance. Histograms show the logarithm of the ratio of the variance of E_s estimated with equation 2.4 and the variance of E_s estimated with equation 2.7. Our weighted estimates have lower variance than NEIC-weighted estimates when the log ratio is positive.

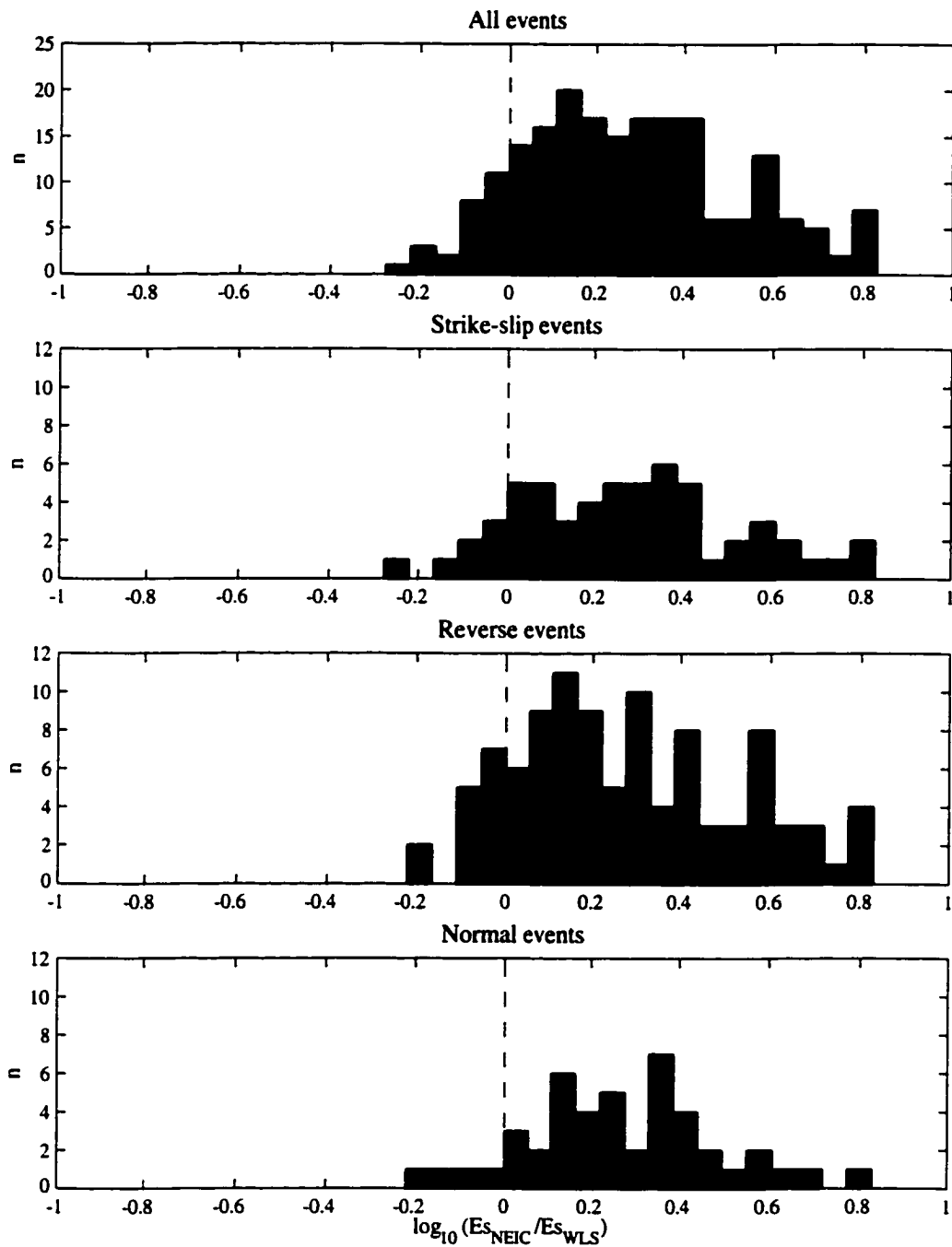


Figure 2-2: Comparison of seismic energy estimates, using equations 2.4 and 2.7. Histograms show the logarithm of the ratio of E_s , estimated with equation 2.4 and E_s , estimated with equation 2.7. There is a tendency toward positive values indicating that our estimates tend to be lower than those found using the NEIC weighting.

The average apparent stress for dip-slip events, estimated using (2.4), is comparable to those from *Choy and Boatwright* [1995]; however, for strike-slip events it is smaller by approximately a factor of 2. Despite the reduced E_s estimates for strike-slip earthquakes relative to that found using NEIC weighting, the tendency for strike-slip events to have larger seismic energy than reverse events with the same moment remains and persists over the entire range of seismic moment considered (10^{18} Nm $\leq M_0 \leq 10^{21}$ Nm).

We calculate the average apparent stress using least squares, with the following model:

$$\log E_s = \log M_0 + b, \quad (2.10)$$

where

$$\tau_\alpha = \mu 10^b, \quad (2.11)$$

and we assume $\mu = 30,000$ MPa. We find that the average τ_α for strike-slip events is 0.70 +0.31/-0.21 MPa at 95% confidence intervals for the mean [*Weisberg*, 1985]; for reverse events it is 0.15 +0.04/-0.03 MPa; and for normal events it is 0.25 +0.05/-0.04 MPa. So, the average apparent stress for strike-slip events is ~ 5 times larger than for reverse events. Figure 2-3 shows the regression line (solid) and its 95% confidence interval for the mean (dashed lines) for each mechanism.

There is a suggestion of moment-dependent scaling of seismic energy in our data set (Figure 2-3). To examine this, we fit the data in Figure 2-3 with the following three models:

$$\log(E_s) = \beta_0 + \beta_1 \log(M_0) + error, \quad (2.12)$$

$$\log(E_s) = \beta_{0S}S + \beta_{0R}R + \beta_{0N}N + \log(M_0) + error, \quad (2.13)$$

$$\begin{aligned} \log(E_s) = & \beta_{0S}S + \beta_{0R}R + \beta_{0N}N \\ & + \beta_{1S}S \log(M_0) + \beta_{1R}R \log(M_0) + \beta_{1N}N \log(M_0) + error. \end{aligned} \quad (2.14)$$

Three dummy variables are given to indicate the focal mechanism of the earthquake (S for strike-slip, R for reverse, and N for normal). We used 200 bootstrap pair-wise replications to test the best fit for each model [*Weisberg*, 1985; *Efron and Tibshirani*, 1993]. Equation (2.12) assumes the null hypothesis that the populations of earthquakes with different focal mechanism represent a single population and allows variation in both the intercept and the slope. The second model (equation (2.13)) keeps the slope constant and equal to one but varies the intercept for the three different populations. The last model (equation (2.14))

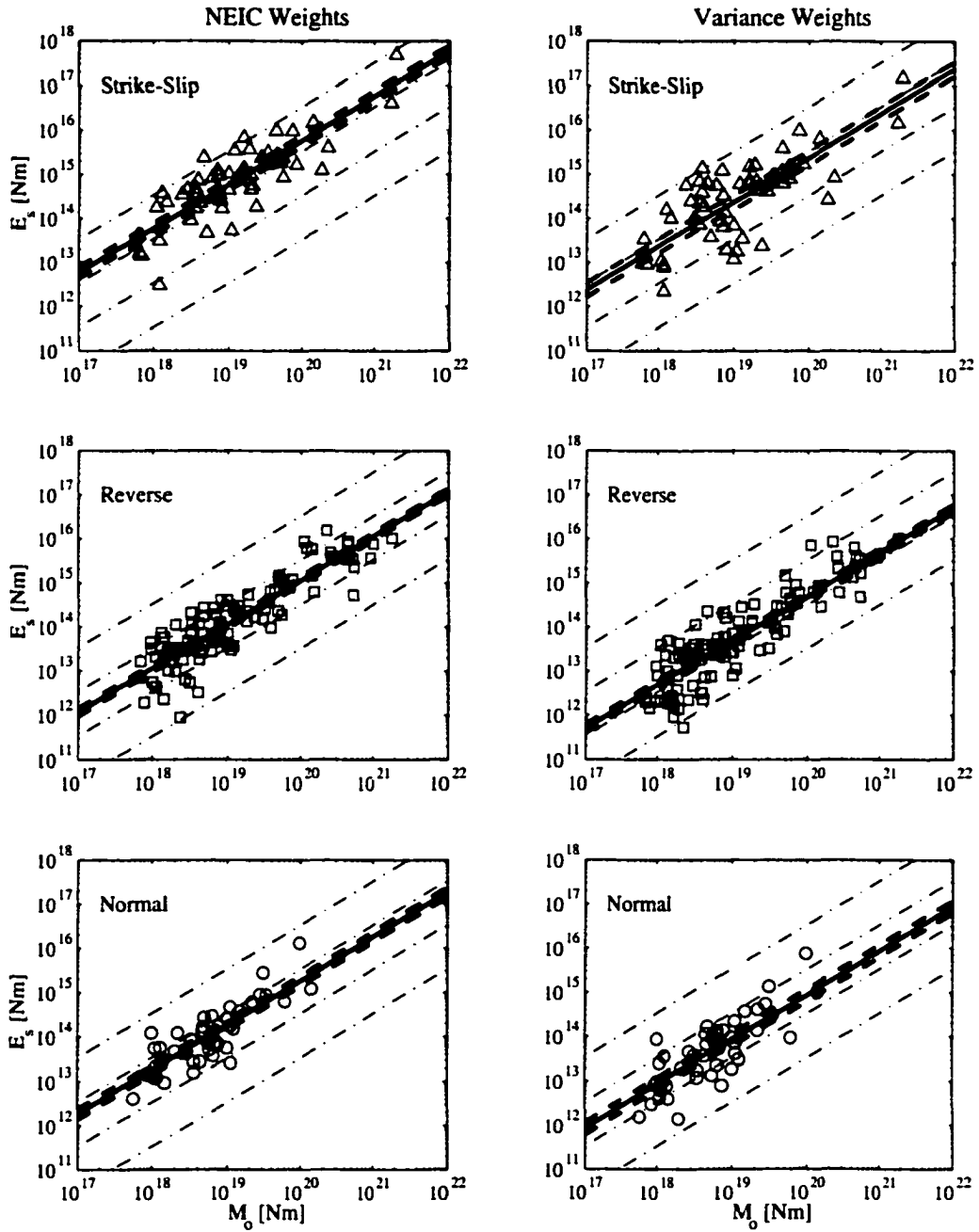


Figure 2-3: Seismic energy versus seismic moment. (left) Best fit using NEIC weighting (equation 2.4) and (right) best fit using variance weighting (equation 2.7). The solid line represents the average apparent stress, and the dashed lines indicate the 95% confidence interval for the mean. The dash-dotted lines indicate an apparent stress of 0.01, 0.1, 1.0, and 10.0 MPa. The triangles denote strike-slip events; the squares indicate reverse events; and the circles indicate normal events.

Table 2.1: Best Fit Results.

Variable	Estimates (Standard Error)		
	Model 1	Model 2	Model 3
β_0	-5.71(1.01)		
β_1	1.03(0.05)		
β_{0S}		-4.65(0.07)	-3.12(1.75)
β_{0R}		-5.33(0.05)	-6.73(1.16)
β_{0N}		-5.08(0.08)	-7.07(2.54)
β_{1S}			0.92(0.09)
β_{1R}			1.07(0.06)
β_{1N}			1.11(0.14)
RSS	70.25	53.39	52.61
Degrees of freedom	202	201	198

assumes that the three populations have different slope and intercept. The results of the fits for the three models are given in Table 2.1.

We find that for a constant slope equal to one (equation (2.13)) we can reject the null hypothesis at a 95% confidence level that reverse, normal, and strike-slip events come from the same population (Figure 2-4). The results for normal events have a larger standard error. This is attributable to the relatively few normal events with large seismic moment, which reduces the effectiveness of the hypothesis tests involving that population. We revisit this question in appendix A with a larger data set.

For the full model (equation (2.14)) we find that the strike-slip events scale as $M_0^{0.92}$, reverse events as $M_0^{1.07}$, and normal events as $M_0^{1.11}$ (Figure 2-4). An F test between models based on (2.12) and (2.14) reveals that the three populations are inconsistent with mechanism independent constant apparent stress

Comparing models (2.13) and (2.14), we cannot reject the null hypothesis of the slope being equal one for the strike-slip events (p value equal to 0.81), for the normal events (p value equal to 0.21), and for the reverse events (p value equal to 0.13).

2.5 Discussion

Choy and Boatwright [1995] found that the average apparent stress for strike-slip events was ~ 1 order of magnitude higher than for dip-slip events (3.62 MPa for strike-slip events and 0.31 and 0.48 MPa for thrust and normal faults, respectively). In this study we have developed an estimate of the seismic energy that is less subject to focal mechanism-dependent bias. We find that the average apparent stress for strike-slip earthquakes is ~ 4.8 times higher than for reverse events and only ~ 1.8 times higher than for normal events (0.70 MPa

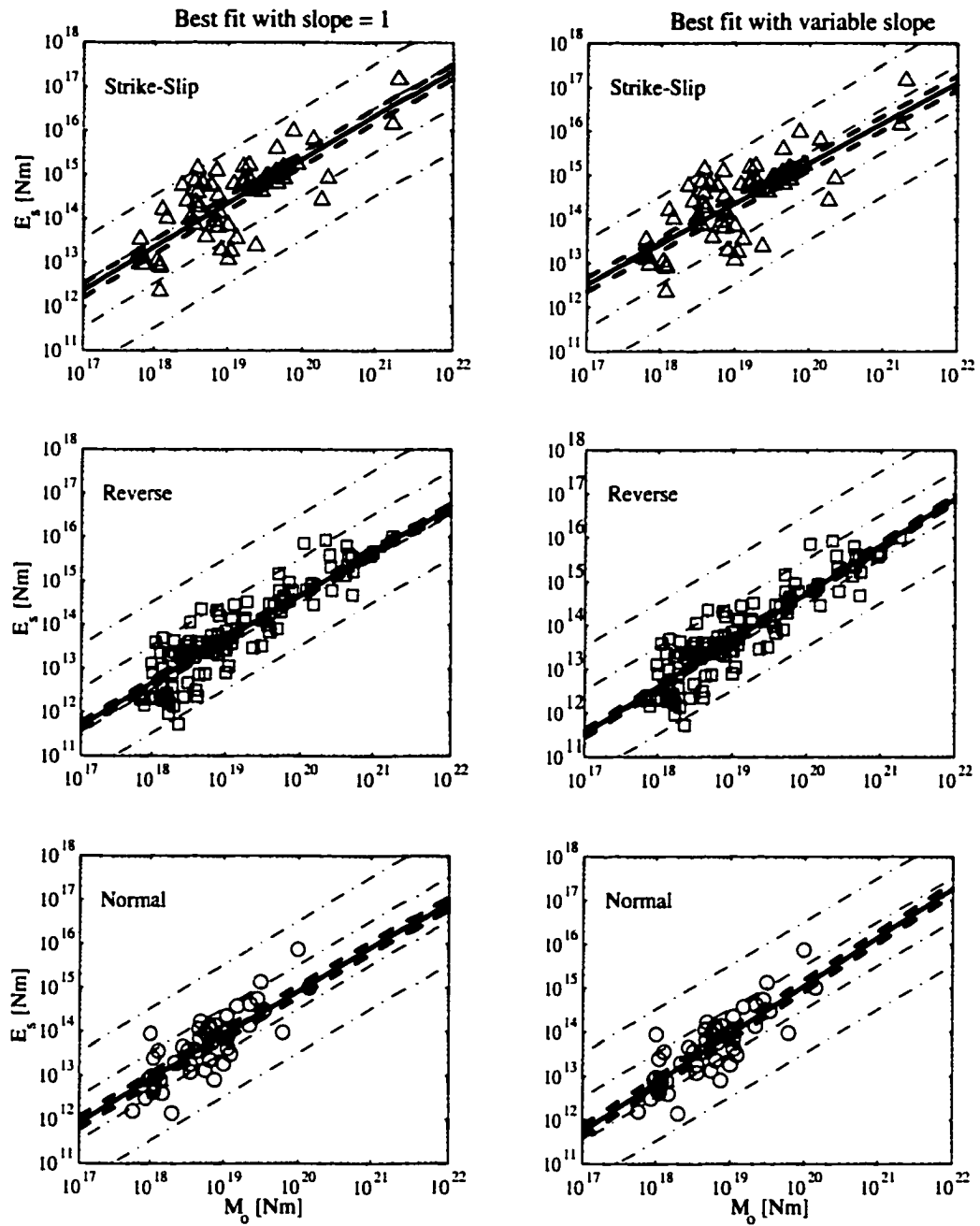


Figure 2-4: Best fit for average apparent stress using variance weighting. (left) Bootstrap replications for the best fit assuming a fixed slope equal to one and (right) pair-wise bootstrap replications for the best fit, varying both slope and intercept. The solid lines represent the best fit, and the dashed lines indicate the 95% confidence interval for the mean.

for strike-slip events and 0.15 and 0.25 MPa for thrust and normal faults, respectively).

Studies to date of seismic energy based on local data have not shown any mechanism dependence [Abercrombie, 1995; Mayeda and Walter, 1996]; however, the number of earthquakes included in these studies in the higher moment range is too limited to allow an informative comparison with our results.

Abercrombie [1995] and Mayeda and Walter [1996] reported that the value of E_s relative to M_0 changes with earthquake size. Both studies found that τ_α increases with increasing seismic moment. Abercrombie [1995] suggested that the apparent scaling she observed might be an artifact arising from errors in calculating the seismic energy. Mayeda and Walter [1996], however, discounted that possibility for their data set and found that E_s varies as $M_0^{1.25}$. We observe no significant variation of apparent stress with seismic moment. Neither Abercrombie [1995] nor Mayeda and Walter [1996] present enough data over the range of seismic moment ($10^{18} \text{ Nm} \leq M_0 \leq 10^{21} \text{ Nm}$) to compare with our observations (Figure 2-5). The intercept of the scaling relation is quite different for the two sets of estimates so that they are not consistent with a continuous scaling of E_s with M_0 over the entire range of seismic moment.

The source of the apparent mechanism dependence is unclear. One possibility is that it reflects a mechanism-dependent difference in the stress drop. This hypothesis is suggested by the scaling of slip in large strike-slip earthquakes [e.g., Mai and Beroza, 2000] and makes two predictions, which could be used to test it. The first is that the discrepancy should disappear for the very largest dip-slip earthquakes as the length of the fault greatly exceeds the downdip extent. The second is that the discrepancy ought to disappear for smaller earthquakes. The first cannot yet be tested due to a lack of recent, very large dip-slip earthquakes. The second is supported by the lack of mechanism dependence to τ_α for smaller earthquakes.

Another possibility is suggested by Brune [1996], who argues that the fault surface might be opaque to seismic waves during rupture. There is evidence from strong ground motion data that this effect might be important [Ni, et al., 1999]. In our estimates of the radiated seismic energy we have assumed that the fault is transparent; however, if the rupturing fault is opaque to seismic waves, then the radiated energy will be preferentially trapped in the hanging wall of dip-slip faults and less will be radiated to teleseismic distances. This effect is likely to be most important for reverse faults, and the sense of the discrepancy is consistent with the mechanism dependence of seismic energy that we observe. In this model

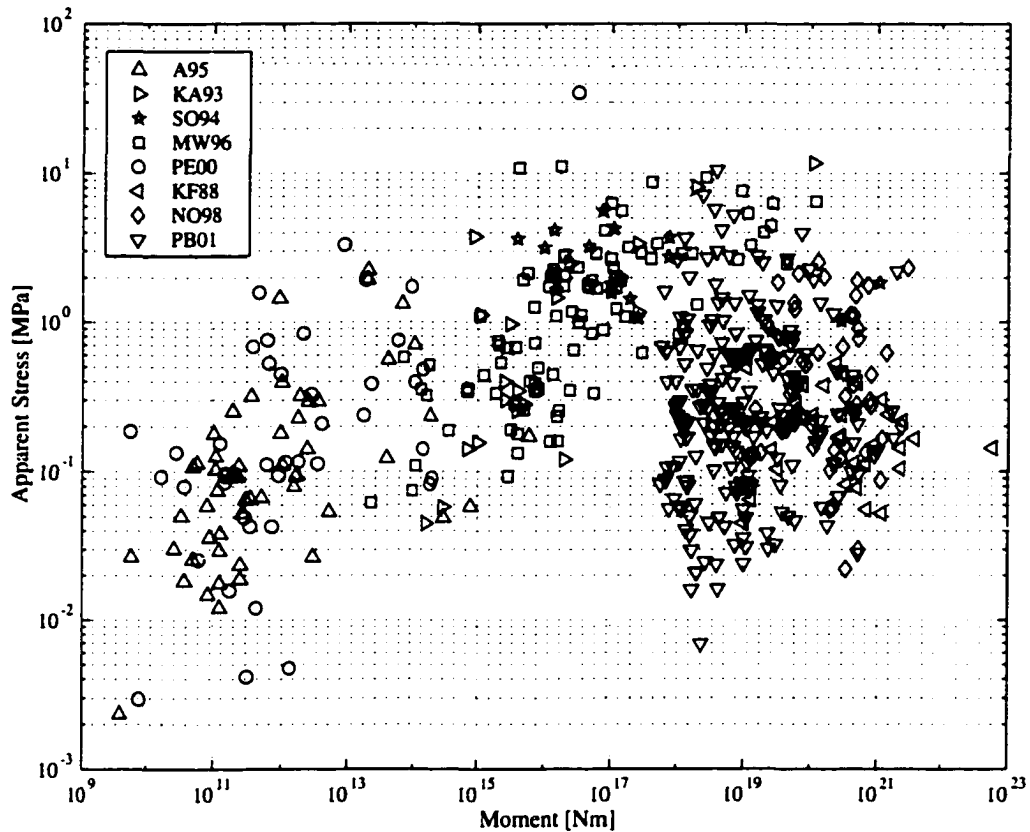


Figure 2-5: Apparent stress versus seismic moment for regional and teleseismic studies. Regional estimates are from *Abercrombie [1995]* (A95), *Kanamori et al. [1993]* (KA93), *Singh and Ordaz [1994]* (SO94), *Mayeda and Walter [1996]* (MW96), and *Prejean and Ellsworth [2000]* (PE00). Teleseismic estimates are from *Kikuchi and Fukao [1988]* (KF88), *Newman and Okal [1998]* (NO98), this study (PB01).

the opacity of the fault is likely to diminish with depth due to an increase in normal stress. Thus the persistence of the mechanism dependence of seismic energy, or the lack of it, with increasing depth would provide an important test of this possibility.

Our estimates of apparent stress are quite low. Apparent stress for individual events is even lower (Figure 2-5). In some cases this is not surprising. The large reverse fault event with the smallest apparent stress is the 1994 Java event, which was previously identified as a tsunami earthquake [*Newman and Okal, 1998*]. Many of the other events with low apparent stress occur at smaller values of the seismic moment ($10^{18} \text{ Nm} \leq M_0 \leq 10^{19} \text{ Nm}$) for which the signal to noise ratio will be lowest and for which the corner frequency will be highest. Both of these effects will contribute to increase variance of estimates of the seismic

energy.

Low values of apparent stress have also been found in other studies that have used teleseismic data to estimate E_s [Kikuchi and Fukao, 1988; Choy and Boatwright, 1995; Newman and Okal, 1998]. This brings up the important unresolved issue of the teleseismic regional discrepancy in estimates of E_s . Estimates of the radiated seismic energy have been reported to be ~ 10 times larger when estimates are made from local versus teleseismic observations [Singh and Ordaz, 1994; Mayeda and Walter, 1996]. Figure 2-6 shows a compilation of teleseismic E_s estimates versus regional E_s estimates for the same earthquake from two studies [Kanamori, et al., 1993; Mayeda and Walter, 1996]. This discrepancy indicates a problem with teleseismic and/or regional estimates of the seismic energy and must be eliminated before reliable conclusions can be drawn. An alternative explanation for the mechanism dependence that we observe is that the amount of energy partitioned to regional versus teleseismic distances is mechanism dependent. This is suggested by the results of Shi et al. [2000], who show that for seismic energy estimates made with regional distance data, dip-slip events have higher apparent stress than strike-slip events. It should be possible to resolve this issue by studying large events with diverse mechanisms for which both regional and teleseismic recording is sufficient to allow a comparison of the two estimates of the seismic energy.

2.6 Conclusions

We have used parametric bootstrap resampling to account for uncertainty in the focal mechanism, depth of the event, geometrical spreading, and corner frequency in estimating the radiated seismic energy. Although the values of seismic energy that we found are smaller than those found using Boatwright and Choy's [1986] technique, we find that a significant difference of a factor of ~ 5 persists in the apparent stress between strike-slip events and reverse events. Thus our results support those of Choy and Boatwright [1995] and indicate that the effects of focal mechanism-dependent bias [Newman and Okal, 1998], while present, do not explain this variation. We find that normal faulting events have intermediate values of apparent stress, between strike-slip and reverse events. The population of normal faulting earthquakes with large seismic moments that we considered, however, was too small to conclude that these differences are significant.

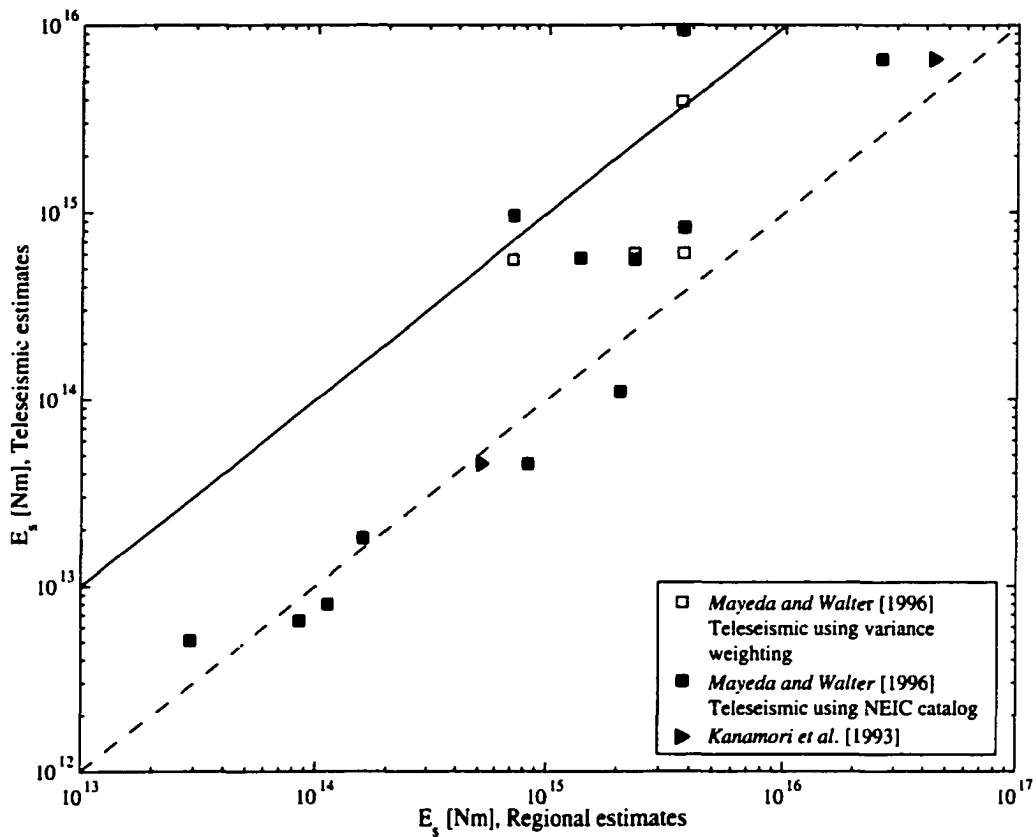


Figure 2-6: E_s teleseismic estimates versus regional estimates. The teleseismic estimates were both obtained from the NEIC catalog (solid symbols) and using variance weighting (equation 2.7) (open symbols), while the regional estimates are from regional studies [Mayeda and Walter, 1996; Kanamori, et al., 1993]. The solid line would be followed if both estimates were equal. The dashed line indicates that the regional estimates are 10 times larger than the teleseismic estimates.

2.7 Acknowledgements

We are thankful to J. Boatwright and P. Segall for their suggestions, J. Brune, A. McGarr, and R. Harris for their reviews, K. Mayeda and S. Prejean for sharing their data, and to J. Picazo in particular for his advice on statistics. Xyoli Pérez-Campos was partially supported by a Chamberlain fellowship; the Littlefield fellowship; SEP, Mexico; and DGAPA, UNAM. This research was supported by NSF grant EAR9909479.

Chapter 3

Reconciling Teleseismic and Regional Estimates of Seismic Energy

Pérez-Campos, X, S. K. Singh, and G.C. Beroza (2002).

3.1 Abstract

Estimates of the radiated seismic energy based on teleseismic and regional data often differ by up to an order of magnitude, with a tendency for regional estimates to be larger than teleseismic estimates for the same event. In this study we use the velocity spectrum determined from teleseismic data after correction for radiation pattern and propagation effects, and the velocity spectrum from regional data, after the corresponding corrections, for nine earthquakes in the Middle American subduction zone in Mexico. We compare the corrected spectra to identify and reduce the sources of the regional vs. teleseismic energy discrepancy, and find that the teleseismic attenuation operator needs to be calibrated. In our case, for the tectonic environment of the Middle America Trench in Mexico, we require teleseismic attenuation that is stronger at high frequencies than the global average. A larger factor, however, is the correction needed to account for site amplification. This correction has an impact on both regional and teleseismic data, but it has a larger impact on regional estimates because the angle of incidence for teleseismic waves is quite steep and the stations are located on more consolidated rocks. By modifying the teleseismic attenuation operator and applying site corrections based on a generic site model, we essentially eliminate the order of magnitude discrepancy between teleseismic and regional estimates of the radiated seismic energy for these events.

3.2 Introduction

The seismic energy is a fundamental parameter of the strength of seismic waves generated by an earthquake that has been estimated seismologically for over 50 years. It has become a routine measurement for large earthquakes to the point where it is used as the basis of an energy magnitude, M_E by the National Earthquake Information Center (NEIC) [Choy and Boatwright, 1995]. In contrast to the seismic moment, measurement of the seismic energy requires observations over a wide range of frequencies and the energy is concentrated at high frequencies, primarily at and above the corner frequency. A number of studies have reported interesting dependencies of the radiated energy with: earthquake size [eg. Abercrombie, 1995; Kanamori et al., 1993] or mechanism [e.g. Choy and Boatwright, 1995; Pérez-Campos and Beroza, 2001]; however, large discrepancies in energy measurements for the same earthquake using different datasets suggest that large uncertainties remain. Such uncertainties cloud the picture and make it difficult to interpret the possible size scaling or mechanism dependence reported in these studies.

The seismic energy can be estimated using regional or teleseismic data. Some authors have used teleseismic P -wave data [Boatwright and Choy, 1986; Kikuchi and Fukao, 1988; Newman and Okal, 1998; Pérez-Campos and Beroza, 2001]. Others have used local or regional data such as Kanamori et al. [1993] and Singh and Ordaz [1994] who used the regional S -wave train for Californian and Mexican earthquakes, respectively; Abercrombie [1995] and Prejean and Ellsworth [2001] who used P and S waves from borehole data; Mayeda and Walter [1996] who used Coda wave from regional records; and Shi et al. [2000] who used Lg waves. Singh and Ordaz [1994] first noted that regional estimates of the seismic energy were larger than the teleseismic estimates by up to an order of magnitude for the same event. Figure 3-1 demonstrates that this discrepancy persists over earthquake mechanism types and tectonic regimes.

Different approaches have been taken in order to resolve this discrepancy. The Hector Mine earthquake in 1999 provided good regional and teleseismic data to address this problem for a shallow strike-slip event. Venkataraman et al. [2002] used empirical Green's function deconvolution to obtain the source spectrum, then, used this source spectrum to estimate the seismic energy. Boatwright et al. [2002], estimated the seismic energy of the same event from the integral of the squared velocity spectrum. They used a geometrical spreading correction that is both frequency and distance dependent for the regional estimation. For

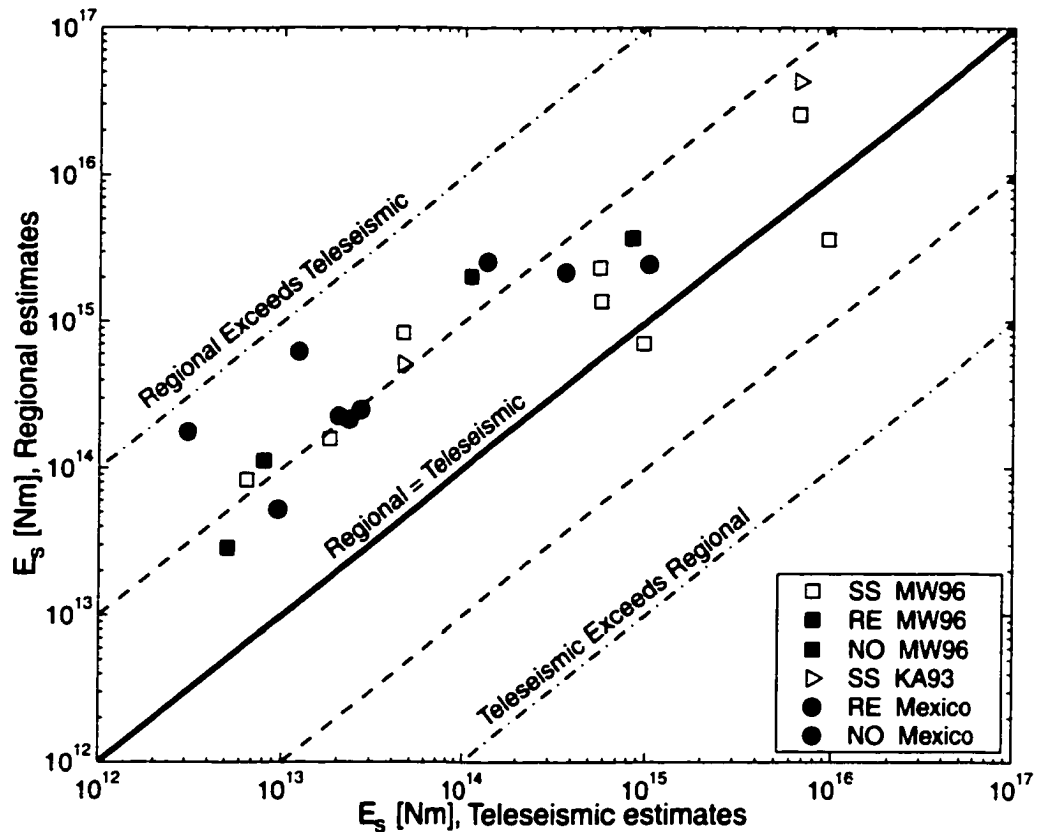


Figure 3-1: Regional estimates of seismic energy vs teleseismic estimates. The open symbols represent strike-slip events; the black symbols, reverse events; and the gray symbols, normal events. The regional estimations were obtained from *Mayeda and Walters* [1996] and *Kanamori et al.* [1993], and the corresponding teleseismic values were obtained from the NEIC catalog. For the Mexican events, the regional values were calculated using the technique outlined by *Singh and Ordaz* [1994], and the teleseismic values using the technique described by *Pérez-Campos and Beroza* [2001].

the teleseismic data, they adjusted the attenuation correction for shallow earthquakes in the western United States and estimated the regional attenuation factor for the region. Also, for both estimates, they corrected the spectrum for a site effect at the recording station. Both studies found an agreement between the teleseismic and the regional estimates and their estimates are very similar to each other. While this agreement is impressive, it only represents one earthquake. Rupture in this event was bilateral, and at relatively low rupture velocity [*Dreger and Kaverina*, 2000], so it may represent an especially favorable situation. In any case, it is important to see if the agreement holds for diverse events in other tectonic environments.

In this study we attempt to reconcile the regional and teleseismic estimates of the radiated seismic energy from nine Mexican earthquakes $5.9 < M_w < 7.4$. We follow the approach used by *Singh and Ordaz* [1994] for the regional estimate and the technique described by *Boatwright and Choy* [1986], as revised by *Pérez-Campos and Beroza* [2001], for the teleseismic estimate (described in chapter 2 of this thesis). We used data from the subduction zone in Mexico, which provides us with good station coverage at both teleseismic and regional distances. Furthermore, we can analyze data for both shallow, reverse-faulting, interplate events and the intermediate-depth, normal-faulting, intraplate events.

We use corrected velocity spectra to identify and reduce the sources of the regional vs teleseismic energy discrepancy. First, we calibrate the teleseismic attenuation operator and replace it with one that is somewhat stronger than that found for other regions. A second, and more significant correction, accounts for site effects. This correction affects both regional and teleseismic data, but has a larger impact on regional data. Together these corrections account for the teleseismic vs regional seismic energy discrepancy for these events.

3.3 Data

Since the 1957 Acapulco earthquake, Mexico has installed more than 300 accelerographs, distributed mainly close to the most seismically active regions such as the Middle America trench and the San Andreas fault system at the northern end of the Baja California Peninsula. There is also a large concentration of stations in Mexico City [*Quass et al.*, 1993] due to the considerable seismic hazard faced by the country's capital. The National Seismological Service of Mexico also operates a broadband seismic network that currently consists of 25 stations. For this study, we used only the accelerograph stations listed in Table 3.1. We choose these stations because they are all located on rock sites [*Quass et al.*, 1993], which will minimize site effects and allow us to use a simplified correction due to a generic rock site for all the data.

We analyzed nine events (Table 3.2) occurring during the period 1993-1999 and located in the Middle America Trench in Mexico. Three of these are reverse, shallow, and interplate; while the other six are normal, intermediate-depth, and intraplate. They range in depth from 22 to 64 km and in magnitude from 5.9 to 7.4. In each case the earthquakes are well recorded both regionally and teleseismically. Standard estimates of the seismic energy for

Table 3.1: Mexican stations used in the analysis.

Station Code	Institution	Name	Lat. [deg]	Long. [deg]	Altitude [m]	κ [s]
ACAJ	CENAPRED	Acapulco	16.8400	-99.8900	60	0.0306
ATYC	II	Atoyac	17.2100	-100.4310	40	0.0250
CAIG	IGF	Cayaco	17.0480	-100.2670	80	0.0306
CALE	II	Caleta de Campos	18.0730	-102.7550	10	0.0387
CHIL	CENAPRED	Chilpancingo	17.4660	-99.4520	1350	0.0306
COPL	II	Copala	16.6050	-98.9740	40	0.0358
COYC	II	Coyuca	16.9690	-100.0840	30	0.0428
HUIG	IGF	Huatulco	15.7680	-96.1080	150	0.0306
IGUA	CENAPRED	Iguala	18.3990	-99.5061	1350	0.0306
MEZC	CENAPRED	Mezcala	17.9300	-99.5900	1660	0.0306
OCLL	II	Ocotillo	17.0380	-99.8750	700	0.0266
OXIG	IGF	Oaxaca	17.0720	-96.7330	1600	0.0306
PET2	II	Petatlán	17.5420	-101.2710	30	0.0237
PETA	II	Petatlán	17.5420	-101.2710	30	0.0237
PLIG	IGF	Iguala	18.3920	-99.5020	875	0.0306
PNIG	IGF	Pinotepa	16.3923	-98.1271	350	0.0306
POZU	II	Pozuelos	17.1000	-99.6300	450	0.0306
SLUI	II	San Luis de la Loma	17.2720	-100.8910	20	0.0221
TEAC	II	Teacalco	18.6280	-99.4530	1000	0.0486
TNLP	II	Tonalapa del Sur	18.0980	-99.5590	740	0.0368
UNIO	II	La Unión	17.9820	-101.8050	50	0.0273
VILE	II	Villita (right)	18.0160	-102.2050	60	0.0414
VNTA	II	La Venta	16.9230	-99.8160	60	0.0245
YAIG	IGF	Yautepec	18.8620	-99.0670	1340	0.0306
ZIIG	IGF	Zihuatanejo	17.6070	-101.4650	50	0.0306

CENAPRED: National Center for National Disaster Prevention; IGF, UNAM: Institute of Geophysics; II, UNAM: Institute of Engineering, UNAM. These stations are located on rock sites [Quass *et al.*, 1993].

Table 3.2: Mexican earthquakes analyzed.

No	Date	Mech.	Long. [deg]	Lat. [deg]	Depth [km]	ϕ_s [deg]	δ [deg]	λ [deg]	M_0 [10^{18} Nm]	M_w
1	930515	RE	16.70	-98.40	21	314	18	90	1.70	6.0
2	931024	RE	16.76	-98.72	21	303	15	90	12.00	6.6
3	960715	RE	17.50	-101.12	22	297	21	93	9.95	6.6
4	990930	NO	16.03	-96.96	47	299	49	-79	140.00	7.4
5	991229	NO	18.00	-101.63	50	122	74	-78	0.86	5.9
6	940523	NO	18.02	-100.57	50	273	39	-76	3.60	6.2
7	970522	NO	18.37	-101.82	54	269	63	-96	6.53	6.5
8	990615	NO	18.13	-97.54	61	309	40	-83	22.00	6.9
9	980420	NO	18.35	-101.19	64	290	60	-85	1.01	5.9

Location and focal mechanism for the normal intermediate events were obtained from local data. The other parameters were obtained from the CMT Harvard Catalog.

these events [Pérez-Campos and Beroza, 2001; Singh, personal communication] reveals that regional estimates are uniformly higher than teleseismic estimates sometimes by more than an order of magnitude (Figure 3-1). A similar tendency was observed by Singh and Ordaz [1994].

3.4 Analysis

We follow *Singh and Ordaz* [1994], in analyzing the *S*-wave train from records of stations within 700 km for the regional analysis. The energy flux of each component, ϵ_i , is estimated in the frequency domain,

$$\epsilon_i = 2\rho\beta \int_0^\infty \dot{u}_i^2(f) e^{\frac{2\pi fR}{\beta Q(f)}} df, \quad (3.1)$$

and then all three components are summed to obtain the total seismic energy:

$$E_s = \frac{4\pi R^2 [G^2(R)/R^2]}{F_s^2} \cdot [\epsilon_N^2 + \epsilon_E^2 + \epsilon_S^2] \quad (3.2)$$

[*Singh and Ordaz*, 1994]. For the teleseismic estimate, we selected the *P*-wave group (*P*, *pP*, and *sP* waves), from stations at distances between 30 and 90°, using only the vertical component and assuming the same proportion between *S*- and *P*-wave energy as *Boatwright and Choy* [1986], $q = 15.58$, to estimate the total seismic energy [*Boatwright and Fletcher*, 1984]. The estimate was obtained using the technique described in chapter 2, using equations (2.1), (2.3), (2.7), and (2.8).

In both cases, we applied corrections for attenuation, geometrical spreading, and radiation pattern. For the regional estimate (equation 3.1), the attenuation is characterized by $e^{-\pi fR/\beta Q(f)}$, where:

$$Q(f) = 273f^{0.66} \quad (3.3)$$

[*Ordaz and Singh*, 1992]; the geometrical spreading correction in this case is given by

$$G(R) = \begin{cases} R & R \leq R_0 = 100 \\ \sqrt{R_0 R} & R > R_0 = 100 \end{cases}, \quad (3.4)$$

where R_0 is a crossover distance before which body waves and after which surface waves are assumed to dominate, and R is the hypocentral distance to the station [*Singh and Ordaz*, 1994]. *Boatwright et al.* [2002] used a frequency-dependent geometrical spreading correction, with a constant crossover distance of 27.5 km for the regional estimation of the 1999 Hector Mine earthquake. However, as discussed later in the chapter, we preferred the correction given by equation (??).

At teleseismic distances (Equation 2.1), the attenuation is characterized by the factor

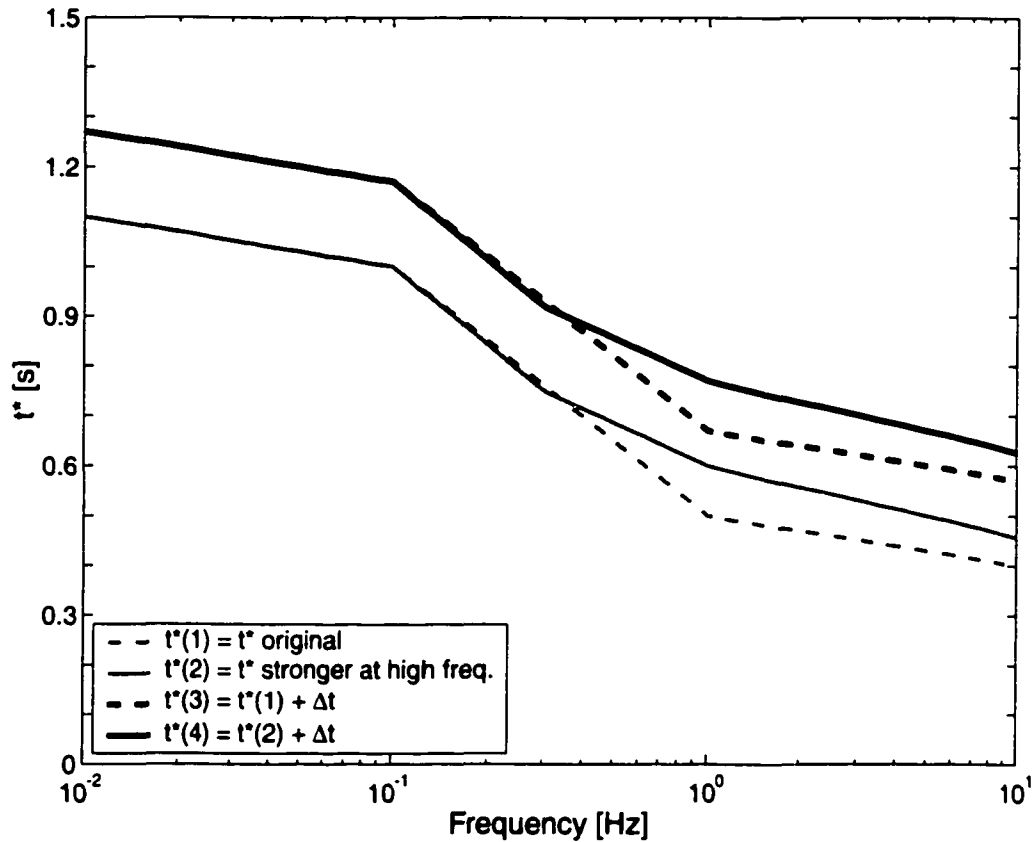


Figure 3-2: Teleseismic attenuation model. The gray dashed line is the original attenuation model (Equation 3.5) from *Choy and Cormier* [1986]; the gray solid line is the model described by equation (3.7); the black dashed line is given by equation (3.5) plus a $\Delta t^* = 0.17$; and the black dashed line is the preferred model, expressed by equation (3.7) plus a $\Delta t^* = 0.17$.

$e^{-\pi\omega t^*/2}$, where we assumed a frequency dependent t^* model given by

$$t^* = \begin{cases} 0.9 - 0.1\log(f) & f < 0.1 \\ 0.5 - 0.5\log(f) & 0.1 < f < 1.0 \\ 0.5 - 0.1\log(f) & 1.0 < f, \end{cases} \quad (3.5)$$

(Figure 3-2) [*Choy and Cormier*, 1986].

The fundamental measurement from which we estimate the seismic energy is the integral of the squared velocity seismogram. For this reason, we compare the corrected velocity spectrum determined from regional data with that obtained from teleseismic data. We correct each of the spectra for attenuation, geometrical spreading, and radiation pattern

effects. The parts of the spectrum with large deviations of the spectral ratio from unity should point to possible sources of the regional vs teleseismic discrepancy. This is assuming that there is no other effect, such as directivity, that would make the spectra to differ.

We then take the ratio of the mean corrected spectra for the regional and teleseismic data (Figure 3-3). We find the largest discrepancies between the spectra at the high frequencies; however, some events show discrepancies at low frequencies as well. Given our assumptions such as that the source spectrum appears essentially the same teleseismically and regionally, are sound, the differences in the E_s estimates and presumably the source spectra, are most likely attributable to problems with the corrections we apply. There is considerable uncertainty in both spectra used to form the ratio due to: site effects, the attenuation correction (at both regional and teleseismic distances); and the geometrical spreading factor. We now investigate whether reasonable changes to these corrections can explain the observed discrepancy in energy.

We gauge the improvement by the extent to which the new corrections result in a convergence of the two estimates. While introducing these degrees of freedom into the problem will naturally decrease the discrepancy, and hence yield a more precise set of measurements, we have no guarantee that the result is more accurate; however, we believe it is more accurate because there is independent evidence that the new corrections are warranted. The precision can be tested by future earthquakes; however, the degree to which the corrections result in a more accurate estimate of the radiated seismic energy is more difficult to gauge.

3.4.1 Site Correction

The spectrum comparison above leads us to a frequency dependent difference that can be partially attributed to site effects produced by the material in the shallow crust. We kept the same attenuation and geometrical spreading corrections given by equations (3.3) and (3.4) for the regional estimates and by equation (3.5) for the teleseismic attenuation correction. We then applied site corrections, using the combined effect of frequency-dependent site amplification and site attenuation,

$$A(f) = A_0(f)e^{-\pi\kappa f}, \quad (3.6)$$

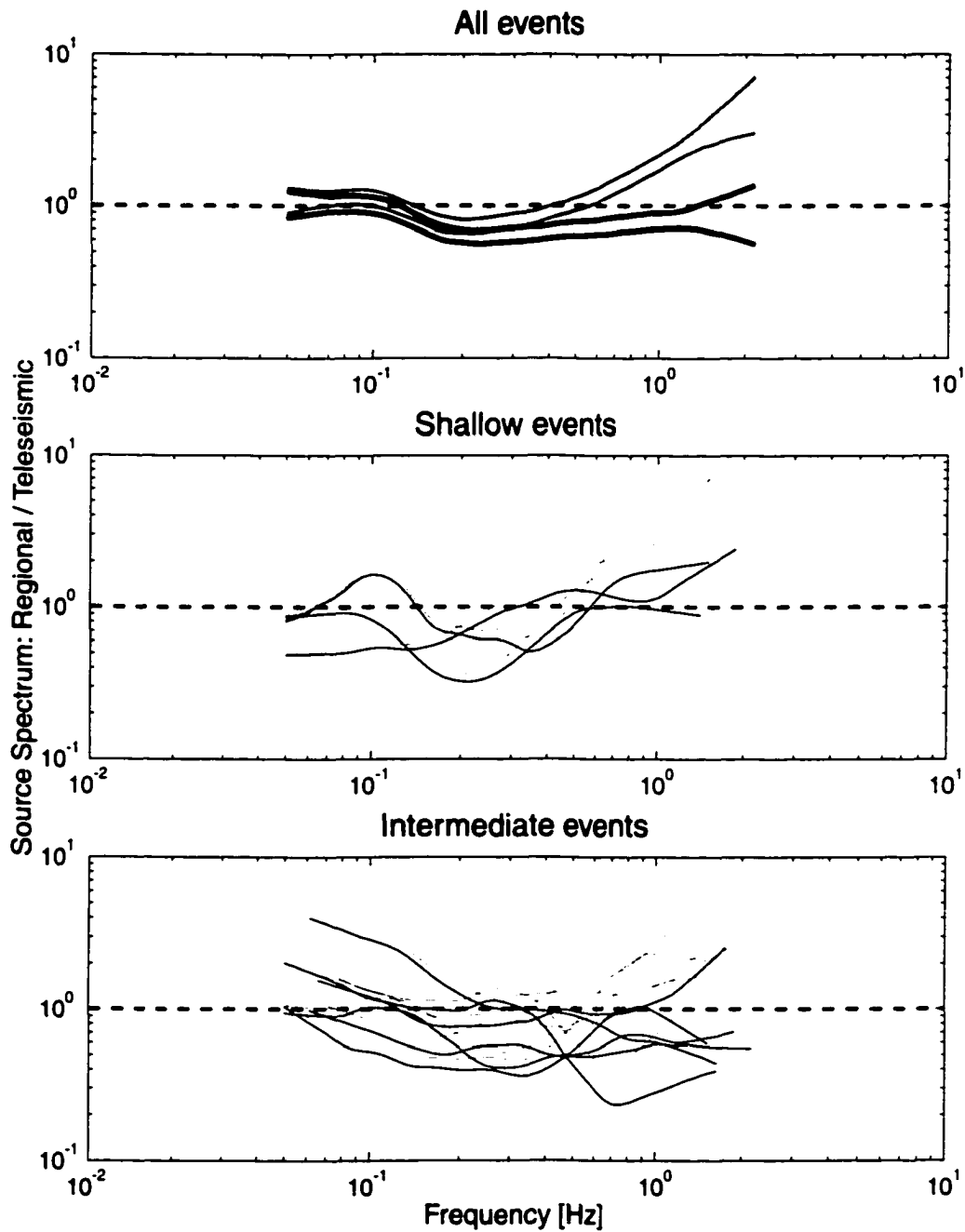


Figure 3-3: Difference between the regional and teleseismic source spectra. The gray lines represent the ratio between the regional and the teleseismic source spectra after applying the site effect correction. The black lines represent the same ratio after applying the preferred corrections. The thick lines in the top panel represent the 95% confidence interval for the mean of the ratios. The ratios have been smoothed using a loess function [Cleveland, 1993].

where $A_0(f)$ is the amplification factor and κ is the attenuation parameter [Boore, 1996; Boore and Joyner, 1997]. This is an attenuation-site effect, since it is meant to account for attenuation in the near surface associated with a particular site [Anderson and Hough, 1984].

For a more accurate estimate of the seismic energy, the site amplification would ideally be estimated from the velocity model of the crust at the particular station. We did not have that information available, so for the regional data we used only stations located on hard rock, as specified on Quass *et al.*, [1993], and adopted the generic rock type amplification factor of Boore and Joyner [1997]. In addition we used an average attenuation parameter appropriate for the station as listed in Table 3.1. The values of κ were obtained from previous studies of the region [Castro *et al.*, 1990; Humphrey and Anderson, 1992]. If the value of κ was unknown, we used an average $\kappa = 0.036$ [Castro *et al.*, 1990; Humphrey and Anderson, 1992]. For the teleseismic stations we used a hard rock amplification factor to correct for the site effect, and $\kappa = 0.01$ [Boore and Joyner, 1997].

3.4.2 Teleseismic Attenuation

The E_s values and the spectra became closer after applying the site correction (Figure 3-5); however, the ratio of the spectra still exhibit discrepancies, especially at high frequencies, suggesting that a modification of t^* may be necessary as well. We tested a second attenuation model, given by the upper bound of the model from Choy and Cormier [1986], which is stronger at high frequencies above 0.3 Hz:

$$t^* = \begin{cases} 0.9 - 0.1 \log(f) & f < 0.1 \\ 0.476 - 0.524 \log(f) & 0.1 < f < 0.3 \\ 0.6 + \frac{0.6}{\log(0.3)} \log(f) & 0.3 < f < 1.0 \\ 0.6 - \frac{0.1}{\log(5)} \log(f) & 1.0 < f \end{cases} \quad (3.7)$$

[Choy and Cormier, 1986]. Boatwright and Choy [1989] observed that the attenuation was stronger for subduction zones, such as Japan, which is consistent with our need of a stronger attenuation correction at high frequencies. However, the correction given by equation (3.7) still appears to be deficient over most of the spectrum frequency band, leading us to the third and fourth models, given by equations (3.5) and (3.7) plus a $\Delta t^* = 0.17$ s (Figure 3-2). Boatwright *et al.* [2002] used $\Delta t^* = 0.14$ to account for the discrepancy between

regional and teleseismic estimates of seismic energy for the 1999 Hector Mine earthquake. The difference between attenuation models was concentrated at the high frequencies, above 0.3 Hz. The fourth model brings the spectral ratio at high frequencies closer to unity (Figure 3-3). As a result, the values of E_s estimated from the two data sets become closer as well.

3.4.3 Regional Attenuation

The frequency-dependent ratio of regional to teleseismic source spectrum, after correcting for site effect, is well explained by changes to the t^* operator. For the regional estimate we retained the $Q(f)$ given by equation (3.3) for the shallow events analyzed in this paper. These three events are along the coast of Guerrero and recorded at stations also located both along the coast and inland in Guerrero, resulting in similar propagation paths to the events used by *Ordaz and Singh* [1992] to obtain their estimate of $Q(f)$. The intermediate depth events, however, are inland and the propagation paths are mutually different than those analyzed by *Ordaz and Singh* [1992]. *García Jiménez* [2001] obtained a $Q(f)$ model for intraplate events in Central Mexico, using the six intraplate events analyzed in this work plus several others. He obtained a frequency dependent model for $Q(f)$ given by

$$Q(f) = 276f^{0.57}, \quad (3.8)$$

which we used for the intermediate depth events. This attenuation factor is different than that given by equation (3.3), having a weaker frequency dependence translated in a smaller attenuation correction at low frequencies (above ~ 1 Hz) but slightly larger at high frequencies.

3.4.4 Geometrical Spreading

Boatwright et al. [2002] noted that the mode of wave propagation at regional distances is a strong function of frequency and suggested a frequency-dependent correction to the geometrical spreading factor that uses a fixed crossover distance, R_0 , to account for this. By making that correction and adjusting the teleseismic attenuation to the third model described above, they were able to reconcile the discrepancy between regional and teleseismic estimates of the radiated seismic energy for the Hector Mine earthquake.

We have accounted for the frequency discrepancy in the spectra already, by using the frequency dependence of $Q(f)$ and the frequency dependent site correction. Analyzing

single-station energy estimates with respect to the distance from the hypocenter to the station, we found that the use of a constant crossover distance, $R_0 = 100$ km, and a geometrical spreading correction that is frequency independent, produces no systematic variation of the residuals with distances suggesting that the same crossover distance works well for both the shallow and intermediate depth events in Mexico. The crossover distance of 100 km was originally estimated empirically by *Street et al.* [1975] for Lg waves from earthquakes in the Central United States. It is worth noting that the estimate of $Q(f)$, both for shallow and intermediate depth events, was done under the assumption of $R_0 = 100$ km, such that the two corrections have been closely intertwined in previous analyses.

3.5 Discussion

Comparing the source spectra using the corrections detailed above for site amplification and attenuation, the discrepancy between the spectra is greatly reduced, especially at high frequencies (Figure 3-3). Also, the difference between the regional and teleseismic energy estimate is much smaller (Figures 3-4 and 3-5). The most significant correction is the one due to the site amplification at regional distances (green arrows in Figure fig:3x4). By correcting for that we reduced the difference between estimates from a factor of ~ 12 to a factor of ~ 5 (Figure 3-5). Neglecting site effects lead to strongly over-predicting the energy based on regional data; while for the teleseismic estimates the effect was smaller. The choice of a teleseismic attenuation model that attenuates waves more strongly at frequencies above 0.3 Hz, further reduces the difference between estimates to the point where they are almost identical (Figure 3-5). The selection of this model is supported by the observations from *Boatwright and Choy* [1989] for the subduction zone of Japan, where they found that the attenuation was stronger. The attenuation effect was stronger for the smaller events and very small for the larger event (red arrows in Figure 3-4), this is related to the low corner frequency of large earthquakes and high corner frequency of the small earthquakes. The combined effect of the site correction and the attenuation correction at teleseismic distances, in general, increases the value of E_s estimated from teleseismic data; because the attenuation correction is visually somewhat larger than the site effect for these data.

Humphrey and Anderson [1992] and *Castro et al.* [1990] explored the effect of the geometrical spreading correction, and found that $R_0 = 100$ km was appropriate for events in Mexico. We also found that $R_0 = 100$ km was a suitable crossover distance. This may be

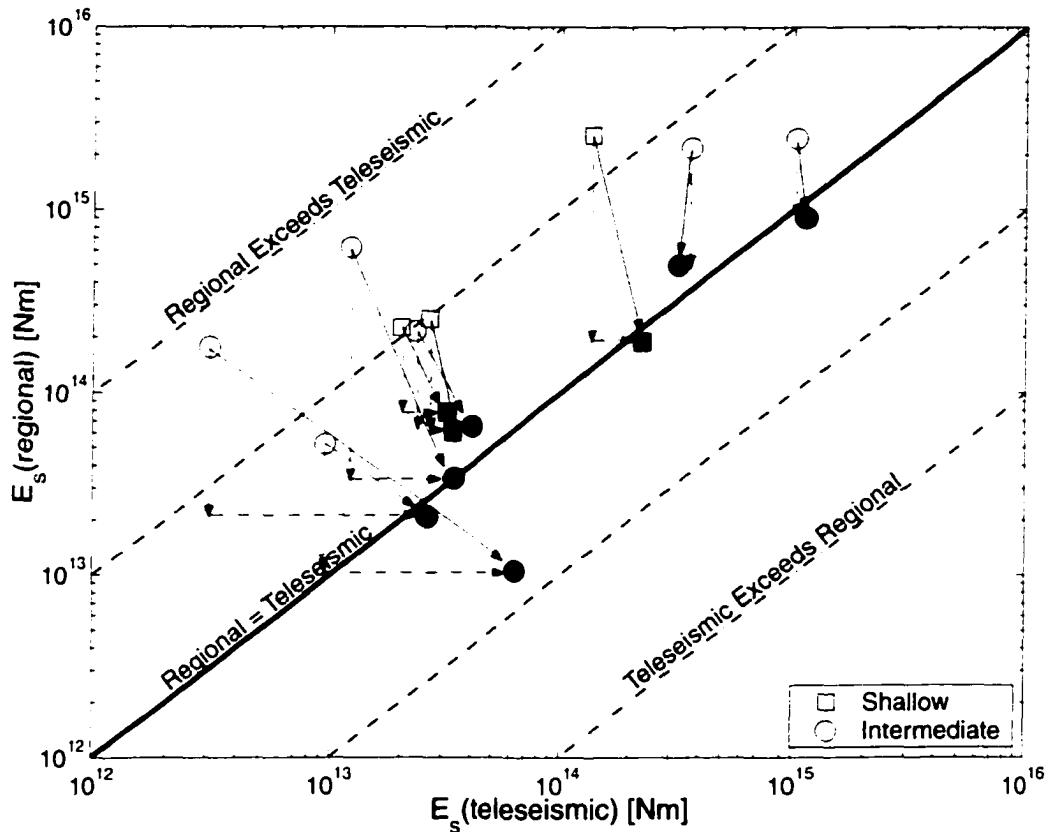


Figure 3-4: Regional vs teleseismic estimates of seismic energy for the Mexican earthquakes. The open symbols are the original values, obtained using the corrections given by equations (3.3), (3.4), and (3.5) and without applying any site effect correction. The green dashed arrows represent the site effect for the regional estimates and the red dashed arrows represent the attenuation effect for the teleseismic estimates. The filled symbols are the values after applying the preferred corrections. The number next to the symbol corresponds the event number on Table 3.2. The black solid arrows represent the total effect after applying the preferred corrections to both regional and teleseismic estimates.

due to the fact that the anelastic attenuation, $Q(f)$, that we used, was estimated previously by other investigators under the assumption of $R_0 = 100$ km and a frequency-independent geometrical spreading factor, at least for the shallow earthquakes. *García Jiménez* [2001] assumed a geometrical spreading equal to the inverse of the distance for all distances. We found no need to include a frequency dependent geometrical spreading correction since the site correction and the different teleseismic attenuation model, both frequency dependent, explained the discrepancy.

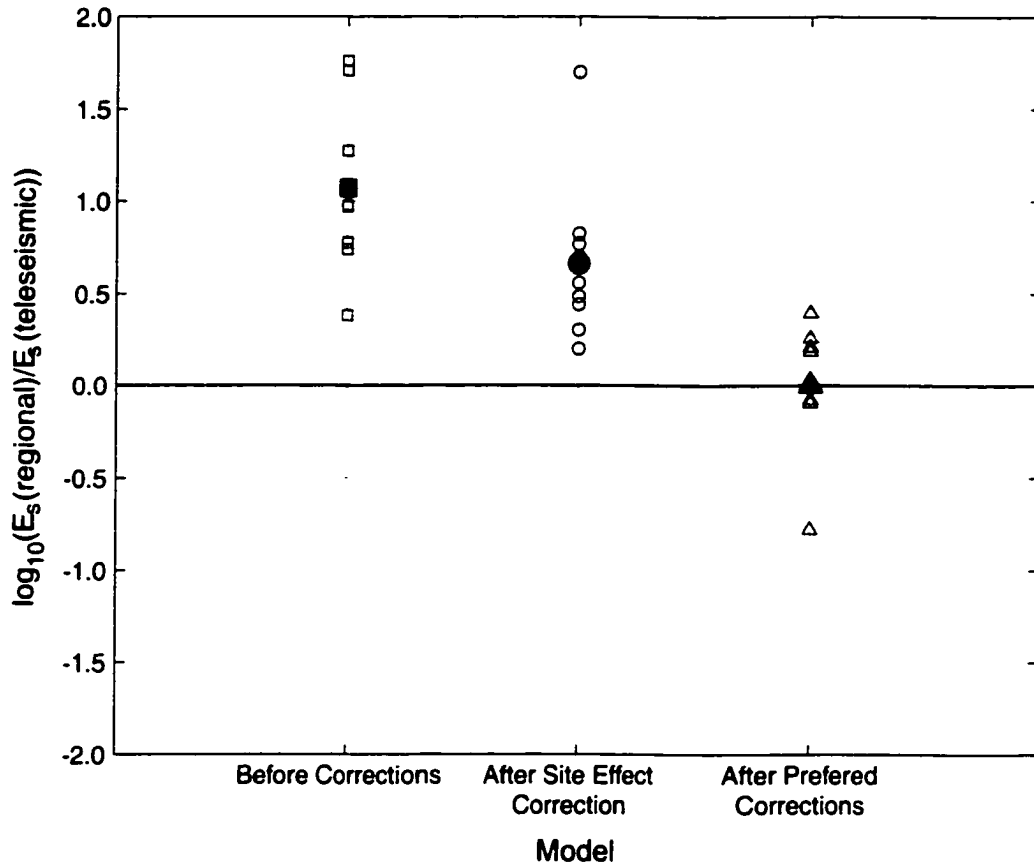


Figure 3-5: Measure of discrepancy. The squares are for the original estimates; the circles are after applying the site effect correction; and the triangles are after applying all the preferred corrections. The open symbols are the difference for each event and the filled symbols are the mean of the difference. The solid line represents that the estimates from regional and teleseismic data are equal.

Then the corrected energy flux is given by

$$\varepsilon = 2\rho c \int_0^{\infty} |\dot{u}(f)|^2 A^{-2}(f) \exp(2\pi f \cdot a) df, \quad (3.9)$$

where c is the wave velocity, $A(f)$ is given by equation (3.6) and a is the attenuation function preferred for each case, teleseismic or regional.

There are still some differences between the spectra reflected in the discrepancies in the seismic energy estimates. These might be attributed to particular site effects or to directivity. In general, the discrepancy was resolved by reducing the regional estimates more than increasing the teleseismic estimates. In the original data set, the discrepancy

was larger for smaller events (e.g., event 5 in table 3.2), which is attributable to the strong effect of our corrections at high frequencies, since smaller events will have higher corner frequencies. The largest difference now corresponds to the deepest event (event 9 in table 3.2), which is also among the smaller analyzed in this study; however, now the sense of the discrepancy is reversed, with the teleseismic estimate exceeding the regional estimate by a factor of approximately 6.

3.6 Conclusions

The site amplification effect is an important factor and must be taken into account when estimating the seismic energy, especially for those stations that are located on soft rock or soils or for stations that are known to have strong site effects for other reasons. Overestimation of the seismic energy can be significant if the site effect is not accounted for.

The attenuation correction is also important and needs to be calibrated both for teleseismic and regional estimates. Ideally, the attenuation model should come from independent data appropriate to the source-receiver path. By our corrections we were able to reduce the difference between the regional and teleseismic estimates of the seismic energy from a mean factor of ~ 12 to a mean factor of ~ 1.1 . Thus, our results suggest that more precise estimates of the seismic energy are now attainable. This can be tested with data from future earthquakes, which will be better recorded both locally, and globally. The question of how to be sure we are obtaining more accurate estimates of the seismic energy is more difficult, but the improved data coverage will help there too.

3.7 Acknowledgments

We thank J. Boatwright for his inspiring discussions and suggestions. This research was supported by NSF grant EAR 9909479. Xyoli Pérez-Campos was partially supported by the Blaustein fellowship; the Robert G. Kirby fellowship; SEP, Mexico; and DGAPA, UNAM.

Chapter 4

Cumulative Energy Flux: Site Effect

4.1 Abstract

The Site effect has been neglected from most studies of seismic energy. Because the seismic energy is calculated using a wide range of frequencies, proper frequency dependent corrections, such as anelastic attenuation and site effect are crucial. In this study, we model the site correction for 49 stations of the Global Seismic Network (GSN), using the teleseismic recordings of 244 earthquakes. We obtained the observed site effect from the squared ratio of the cumulative seismic energy with respect to frequency of each event at the station before site correction, and after applying a generic correction for a hard-rock site. Based on this ratio, some stations show a frequency dependent discrepancy starting at around 0.3 Hz, which we model as a site effect. We use simulated annealing to obtain a model that best corrects for site effects at each station. Using these models, reduces the mean E_s by a factor of ~ 1.6 and the uncertainty of seismic energy estimates by about 4%.

4.2 Introduction

Nowadays, various catalogs report different source parameters such as magnitude or seismic moment, some of them (e.g. NEIC) also report the seismic energy. Seismic energy has become an important parameter to describe an earthquake since it is estimated using the whole frequency band. However, the broadband nature of seismic energy measurements requires frequency dependent corrections to the analyzed signal.

The corrections applied to calculate the seismic energy include: instrument response, radiation pattern, attenuation, and geometrical spreading. Recently *Boatwright et al.* [2002] found that a frequency dependent site correction was extremely important (also described

in chapter 3). Site effects have been widely explored for earthquake hazards, but tend to be used in seismic hazard analysis (e.g. *Singh et al.*, 1988; *Hough et al.*, 1990) where there is large damage potential and where strong ground motion is likely to occur. Some studies have used the H/V spectral ratio [e.g. *Atkinson*, 1993; *Lermo and Chávez-García*, 1993; *Theodulidis et al.*, 1996; *Huang and Teng*, 1999; *Yucha and Luzon*, 2000; *Chen and Atkinson*, 2002], or the ratio between stations at the soft sediments and stations at the hard rock [e.g. *Ordaz, et al.*, 1988] to characterize site amplifications. However, many sites used for other seismological purposes have not been studied thoroughly. *Singh et al.* [1995] observed that for stations that were thought to be on hard rock sites, some amplification is still present. For seismic energy estimates, few authors have corrected for site effect. *Shoja-Taheri and Anderson* [1988] noticed the importance of site effects at some stations when estimating E_s for the 1978 Tabas, Iran earthquake. *Smith, et al.* [1989] used a factor to account for amplification at sedimentary sites. *Boatwright et al.* [2002] used a frequency dependent correction to estimate E_s for the 1999 Hector Mine earthquake; for the regional estimate, they grouped the stations in NEHRP site classes to calculate the site corrections; while for the teleseismic estimate, they used a generic correction for hard rock, from *Boore and Joyner* [1997]. By correcting for site effects, they were able to obtain values for the seismic energy for teleseismic and regional data that agreed with one another.

If enough stations contribute to E_s estimate, then using a generic site correction is probably sufficient; however, we observe that for some stations this correction does not work well and the values of E_s are drastically over or under predicted. Even though the technique described in chapter 2 gives less weight to outliers, having a station that over estimates E_s produces higher uncertainty and can bias the estimate. This problem is greater for studies or conclusions drawn from single-station estimates or estimates obtained from only a few stations.

Since seismic energy is calculated from the squared velocity spectrum, to observe the frequency dependent discrepancies, we analyzed the ratio between the cumulative seismic energy of each event observed at a given station; both before applying the site correction and after using a generic hard-rock site correction. If the ratio is larger than one, E_s would be over estimated and it would be underestimated if the ratio is smaller than one. The square root of the ratio represents the net site effect. Since we ignore the velocity and density model below the station, we used the ratio to invert for the density and velocity, using simulated annealing [*Kirkpatrick et al.*, 1983] to find the best site effect correction

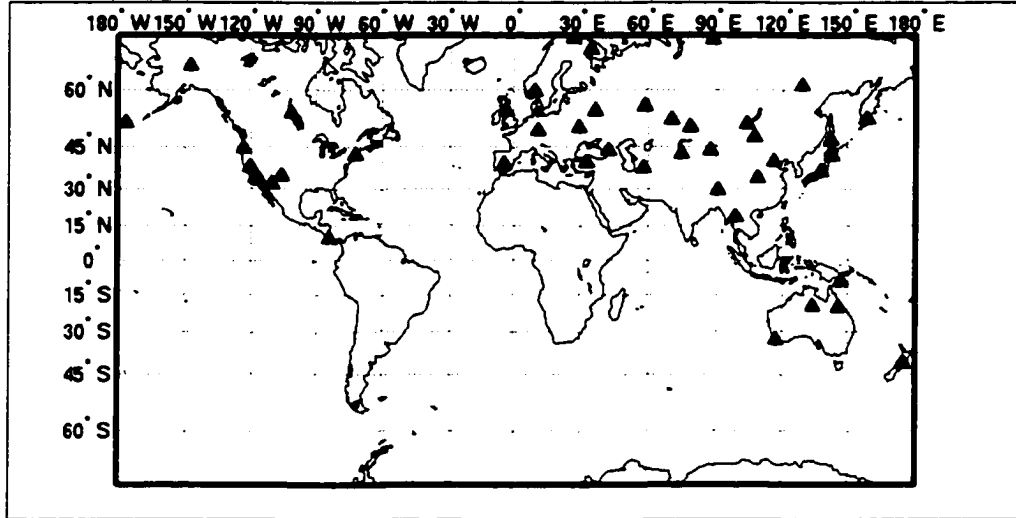


Figure 4-1: Location of Global Seismic Network (GSN) stations analyzed.

for each station.

For some stations, it is absolutely critical to correct for site effect while for other the site effect would be minimum. In this study, we estimate the site effect for 49 GSN stations. Using this correction, we find the mean E_s is reduced by a factor of ~ 1.6 and the uncertainty in the seismic energy estimates is reduced by $\sim 4\%$ on average.

4.3 Data: Cumulative Seismic Energy

Based on *Boatwright et al.* [2002] and our results from chapter 3, we need to include a site effect correction into the seismic energy estimation. We used the recordings for 244 events around the world, from 1992 to 2002, 108 of them have reverse mechanism, 67 are normal, and 70 are strike-slip. For each event we used only those stations of the Global Seismic Network (GSN) that recorded the event at teleseismic distances; i.e., between 30 to 90° (Figure 4-1). For each earthquake, e , we estimated the cumulative seismic energy at each station, s , before site correction, $E_s^{e,s}(f)$, given by

$$E_s^{e,s}(f) = (1 + q)4\pi(F)^2 \frac{R^2}{F^2} \frac{\rho\alpha}{\pi} \int_0^f |v(\omega)|^2 e^{\pi\omega t^*} d\omega, \quad (4.1)$$

where ρ and α are the density and velocity at the source, respectively; F is the generalized radiation pattern coefficient and $\langle F \rangle$ is the rms radiation pattern; R is the geometrical spreading; $q = 15.58$ is the partitioning of the S to P wave radiated energy.

We also computed the weighted-mean cumulative seismic energy for each event, $E_s^e(f)$, given by

$$E_s^e(f) = (1 + q)G^{-g}\varepsilon^e(f), \quad (4.2)$$

where G^{-g} is given by Equation 2.8; and $\varepsilon^e(f)$ is the cumulative energy flux given by

$$\varepsilon^e(f) = \begin{bmatrix} \varepsilon^{e,1}(f) \\ \vdots \\ \varepsilon^{e,i}(f) \\ \vdots \\ \varepsilon^{e,n}(f) \end{bmatrix} \quad (4.3)$$

where the $i - th$ component is for the $i - th$ station, of a total of n stations and is given by

$$\varepsilon^{e,i}(f) = \frac{\rho\alpha}{\pi} \int_0^f |\dot{u}(\omega)|^2 \hat{A}_0^2(\omega) \exp(\omega\hat{\kappa}) \exp(\omega t_\alpha^*) d\omega. \quad (4.4)$$

This equation is similar to Equation 2.1; however, it includes a site correction, due to a hard rock site effect, given by $\hat{A}_0^2(\omega) \exp(\omega\hat{\kappa})$ (Equation 3.6) (Figure 4-2).

We assumed that this weighted average is the best approximation to the true cumulative seismic energy. As explained in chapter 2, this weighting technique gives less value to the outlier stations, getting a more robust estimate.

We analyze only those 49 stations that recorded 30 or more events in order to have a robust analysis. It is important to include events of varying mechanisms at each station to avoid other possible effects such as directivity or over prediction due to a low radiation pattern coefficient from a near nodal station. These 49 stations are listed on Table 4.1 and mapped on Figure 4-1.

4.4 Ratio: Site Effect

We compare $E_s^{e,s}(f)$ with $E_s^e(f)$, for this comparison we used the ratio the cumulative energy flux for each event e at each station i , given by equation (4.4), and the average of

Table 4.1: GSN stations analyzed.

No.	Code	Location	Lat. [Deg]	Long. [Deg]	Alt. [m]	Events		
						RE	NO	SS
1	KONO	Konsberg, Norway	59.6491	9.5982	216	26	16	18
2	ESK	Eskdalemuir, Scotland	55.3167	-3.2050	242	20	12	13
3	OBN	Obninsk, Russia	55.1138	36.5687	160	28	10	22
4	AAK	Ala-Archa, Kyrgyzstan	42.6390	74.4940	1645	60	11	17
5	KIV	Kislovodsk, Russia	43.8663	42.4393	1054	35	19	17
6	CHTO	Chiang Mai, Thailand	18.7900	98.9769	100	46	15	21
7	PAS	Pasadena, California	34.1483	-118.1717	308	21	11	13
8	CTAO	Charters Towers, Australia	-20.0883	146.2544	357	20	11	12
9	TUC	Tucson, Arizona	32.3096	-110.7846	874	26	11	7
10	ANMO	Albuquerque, New Mexico	34.9462	-106.4567	1740	21	10	6
11	ARU	Arti, Russia	56.4302	58.5625	250	30	20	18
12	LSA	Lhasa, China	29.7000	91.1500	3789	21	12	7
13	WRAB	Tennant Creek, Australia	-19.9336	134.3600	366	11	9	12
14	KBS	Kings Bay, Spitzbergen	78.9175	11.9239	46	18	14	14
15	COR	Corvallis, Oregon	44.5857	-123.3032	121	22	12	11
16	HIA	Heredia, Costa Rica	10.0270	-84.1170	1253.2	17	10	11
17	KIEV	Kiev, Ukraine	50.6944	29.2083	163	17	7	10
18	CMB	Columbia College, California	38.0350	-120.3850	719	32	17	12
19	ANTO	Ankara, Turkey	39.8689	32.7936	883	21	4	8
20	FFC	Fin Flon, Canada	54.7250	-101.9780	338	18	18	19
21	PFO	Pion Flat, California	33.6092	-116.4550	1280	33	15	14
22	GRFO	Grafenberg, Germany	49.6919	11.2217	425	17	10	13
23	ALE	Alert, Canada	82.5033	-62.3500	60	24	10	15
24	PAB	San Pablo, Spain	39.5458	-4.3483	925	12	14	13
25	BRVK	Borovoye, Kazajhstan	53.0581	70.2828	330	20	18	14
26	BJT	Baijiatuan, China	40.0183	116.1679	197	18	8	17
27	XAN	Xi'an, China	34.0394	108.9214	630	18	8	17
28	HRV	Harvard, Massachusetts	42.5060	-71.5580	180	13	8	13
29	KURK	Kurchatov, Kazakhstan	50.7154	78.6202	184	28	13	8
30	WMQ	Urumqi, China	43.8211	87.6950	970	19	10	9
31	LVZ	Lovozero, Russia	67.8979	34.6514	630	21	4	12
32	KEV	Kevo, Finland	69.7553	27.0066	81	17	5	10
33	ABKT	Alibek, Turkmenistan	37.9304	58.1189	678	28	8	13
34	COL	College, Alaska	64.9000	-147.7933	320	36	11	11
35	ADK	Adak, Alaska	51.8837	-176.6844	116	16	9	9
36	COLA	College Output, Alaska	64.8738	-147.8511	194	16	15	10
37	ERM	Erimo, Japan	42.0150	143.1572	40	23	8	11
38	ULN	Ulaanbaatar, Mongolia	47.8652	107.0528	1615	18	15	7
39	PET	Petropavlovsk, Russia	53.0236	158.6500	150	18	13	9
40	MA2	Magadan, Russia	53.0236	158.6500	150	19	20	18
41	NRIL	Norilsk, Russia	69.5049	88.4414	92	23	7	9
42	PMG	Port Moresby, Papua New Guinea	-9.4092	147.1539	167	15	7	11
43	TLY	Talaya, Russia	51.6807	103.6438	579	28	13	16
44	TIXI	Tiksi, Russia	71.6490	128.8665	50	13	11	7
45	YSS	Yuzhno Sakhalinsk, Russia	46.9500	142.7500	100	25	19	14
46	MAJO	Matsushiro, Japan	36.5425	138.2073	405	26	18	25
47	SNZO	South Karori, New Zealand	-41.3101	174.7046	-12	19	8	6
48	NWAO	Narrogin, Western Australia	-32.9268	117.2333	265	24	11	14
49	YAK	Yakutia, Russia	61.0120	129.4300	105	21	14	15

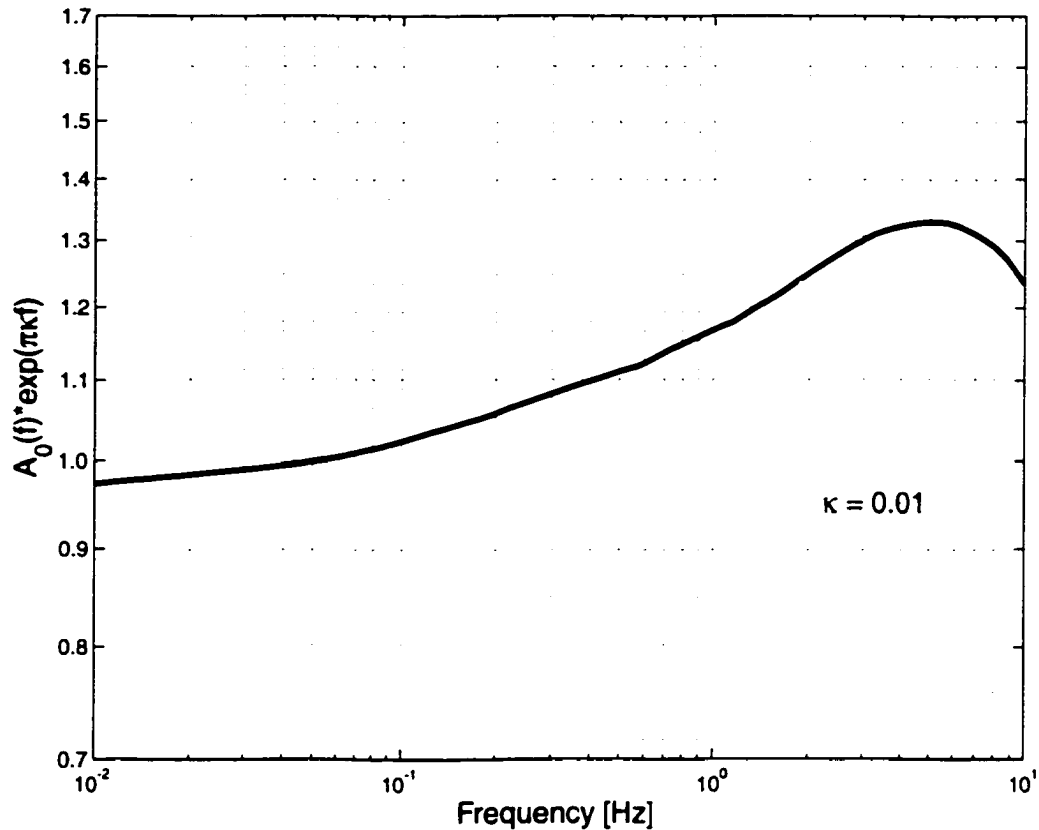


Figure 4-2: Hard-rock site correction [Boore and Joyner, 1997]. The velocity model used for the amplification calculation is given on Table 4.2 and κ was assumed to be 0.01.

the event at all stations (Equation 4.3); i.e.,

$$ratio = \frac{\varepsilon^{e,i}(f)}{\varepsilon^e(f)}. \quad (4.5)$$

Figure 4-3 shows the distribution of the final ratio at each station. Note that some stations, even after the generic hard-rock site correction, are either over or under predicting the seismic energy. In general, the distributions are shifted to values greater to zero, which indicates an over prediction of E_s . The ratio distribution is plotted as a function of frequency, which allows us to detect frequency dependent behavior. In this case a good agreement along the frequency band will be represented as a horizontal line (gray dashed line). However, we observe that for some stations (e.g., stations 3, 5, 13, 15, 22, 35, 37, 39, and 49), there is a clear discrepancy from a ratio equal to one. This discrepancy seems to be frequency

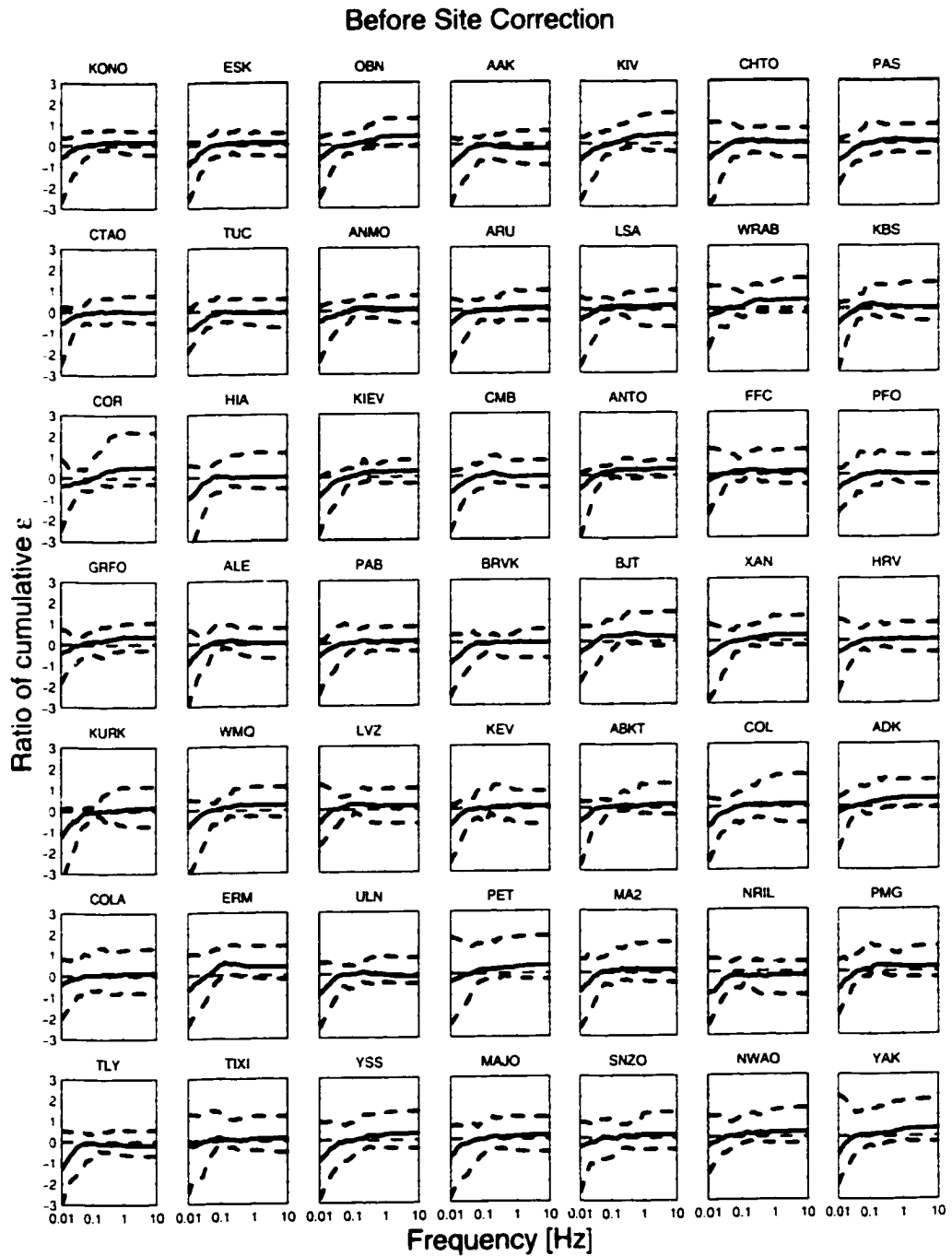


Figure 4-3: Distribution of log-ratio before site correction. Each plot represents a station. The horizontal black line represents the median of the distribution and the black dashed lines represent the 5% and 95% of the distribution. The horizontal green dashed line represents a good agreement between the cumulative energy estimates.

dependent, starting around ~ 0.3 Hz (Figure 4-3). Since the ratio was performed between the cumulative E_s before the site correction and after a generic site correction, we inferred that the frequency dependent differences observed are due to the lack of the site correction. Thus, we seek to find the site correction that produces the least discrepancy.

4.5 Simulated Annealing: Best Site Effect Correction

The Simulated Annealing (SA) algorithm is an optimization method developed as an analogy with annealing in solids, where a liquid is cooled down, in such fashion that in every step there is equilibrium between the liquid and the solid, and that the final result is a perfect crystal that has a minimum energy state. This process is similar to an optimization method where we want to find the minimum of given function depending on many parameters [Kirkpatrick *et al.*, 1983]. Advantages of this probabilistic optimization method over others is its ability to deal with local minima and large number of parameters; however, its sensitivity lies in the "cooling schedule" assumption, if it is too fast, it may not get the global minimum, on the other hand, if it is too slow, it will have a high CPU cost. This technique has been used to solve various problems in Seismology, such as the deconvolution of seismograms [Courboulex *et al.*, 1996] or to estimate the crustal structure [Iglesias *et al.*, 2001].

In this case, we want to invert for the site effect, given by equation (3.6). Previous studies have found κ , a parameter that represents attenuation effects at the station, by comparing observed spectra to model event spectra [Humphrey and Anderson, 1992] or by the linear squares fit of the log linear observed spectra [Castro *et al.*, 2000]. The amplification produced by a site effect has also been estimated using the quarter wave length approximation, first introduced by Joyner *et al.* [1981]. We base our modelling in this approach.

The ratio between equation (4.1) and equation (4.2) will result on the squared site effect, given by equation (3.6). In this study, we follow Boore and Joyner [1997], and Boore's [1996] method, where the frequency dependent amplification is given by the square root of the ratio of the impedances at the source and at a given depth:

$$A_0(f(z_i)) = \sqrt{\frac{\rho c}{\rho(f(z_i)) c(f(z_i))}}, \quad (4.6)$$

Table 4.2: Velocity model for a hard rock.

Depth [km]	Velocity [km/s]	Density [kg/m ³]
0.00	2.00	2.50
0.04	2.72	2.40
0.08	3.08	2.40
0.12	3.76	2.40
0.26	4.50	2.48
0.43	5.11	2.59
0.69	5.37	2.63
1.00	5.54	2.66
2.20	5.80	2.70
8.00	6.23	2.80
17.00	6.50	2.80
26.00	8.08	3.38
35.00	8.06	3.37
44.00	8.05	3.37
53.00	8.03	3.37

where $\rho(z_i)$ and $c(z_i)$ are the density and the wave velocity at frequency $f(z_i)$. The frequency given by the quarter wave length approximation is

$$f(z_i) = \frac{1}{4t_c(z_i)}, \quad (4.7)$$

where the travel time of the wave c at a depth z of the layer i , $t_c(z_i)$, is calculated as

$$t_c(z_i) = t_c(z_{i-1}) + \frac{z_i - z_{i-1}}{c(z_i) - c(z_{i-1})} \ln \left[\frac{c(z_i)}{c(z_{i-1})} \right]. \quad (4.8)$$

We used equations, (4.8), (4.7), (4.6), and (3.6) for the forward model, using as an initial model the density-velocity model for a generic hard rock site (Table 4.2) [Boore, written communication]. Then, we used simulated annealing to find the best density-velocity model that fits the observed site effect. The resulting models are shown in figure 4-4 and the site effect that these models produce are shown in figure 4-5. They differ from the initial models at shallow depths being slower and faster at depth. The density model varied the least. We reach to these model taking into account the physical limits of the P -wave velocity and the density and restrict the deeper layers to be faster and denser.

4.6 Discussion

The modelling of site effects is not a linear problem, we prefer simulated annealing to solve it because the small number of parameters makes the forward model easy to evaluate and

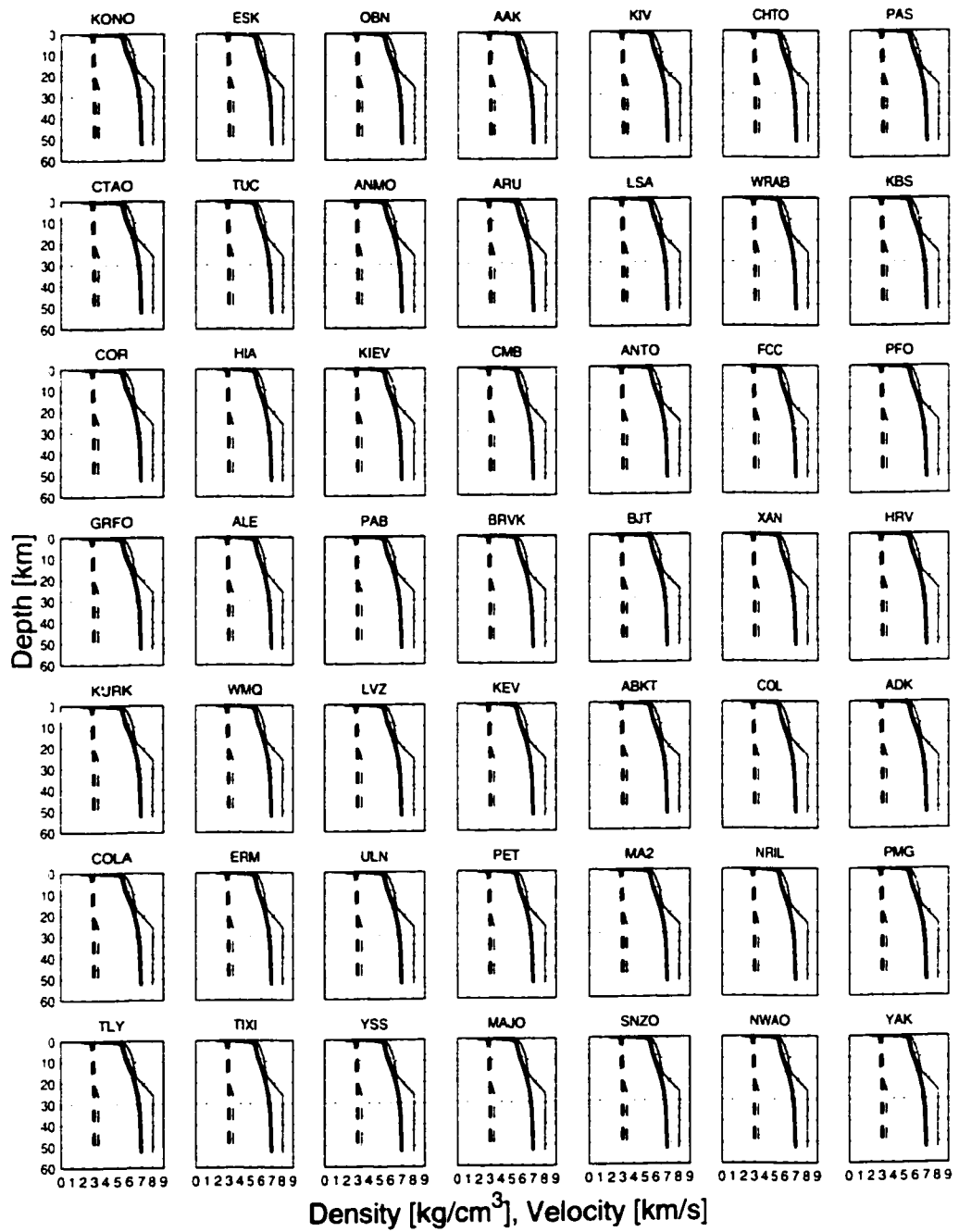


Figure 4-4: Density (dashed lines) and velocity (solid lines) models. The thin green lines represent the initial model (hard rock) and the black thick lines represent the final model. Each plot represents a station.

fast. Furthermore, the implementation of constrains and evaluation of the objective function (error function) is convenient and easy. We calculate the cumulative seismic energy at each station using the site effect models and obtain the ratio against the variance-weighted cumulative seismic energy (Figure 4-6). This ratio shows that using a better site effect correction solves some of the over and under prediction of the seismic energy. As shown in figure 4-7, not only the uncertainty in the estimate of seismic energy at a single stations is reduced by about 4% but most important, the distributions are centered around zero, which indicates that the station will not systematically over- or under-predict E_s . The values of E_s estimated at a single station have been reduced by a factor of about 1.6. This also suggests that the remaining effect is not due to a poor station correction but to other factors, which may include source effects, such as directivity, or path effects, such as attenuation.

4.7 Conclusions

The site effect has been neglected from important source parameter estimations, such as the seismic energy. For this source parameter, a site effect correction that is frequency dependent is very important since the estimation of the seismic energy requires corrections over a broad frequency band. The lack of this correction or a poor choice of it will significantly miss predict the seismic energy estimate.

4.8 Acknowledgments

This research was supported by NSF grant EAR 9909479. Xyoli Pérez-Campos was partially supported by SEP, Mexico and DGAPA, UNAM.

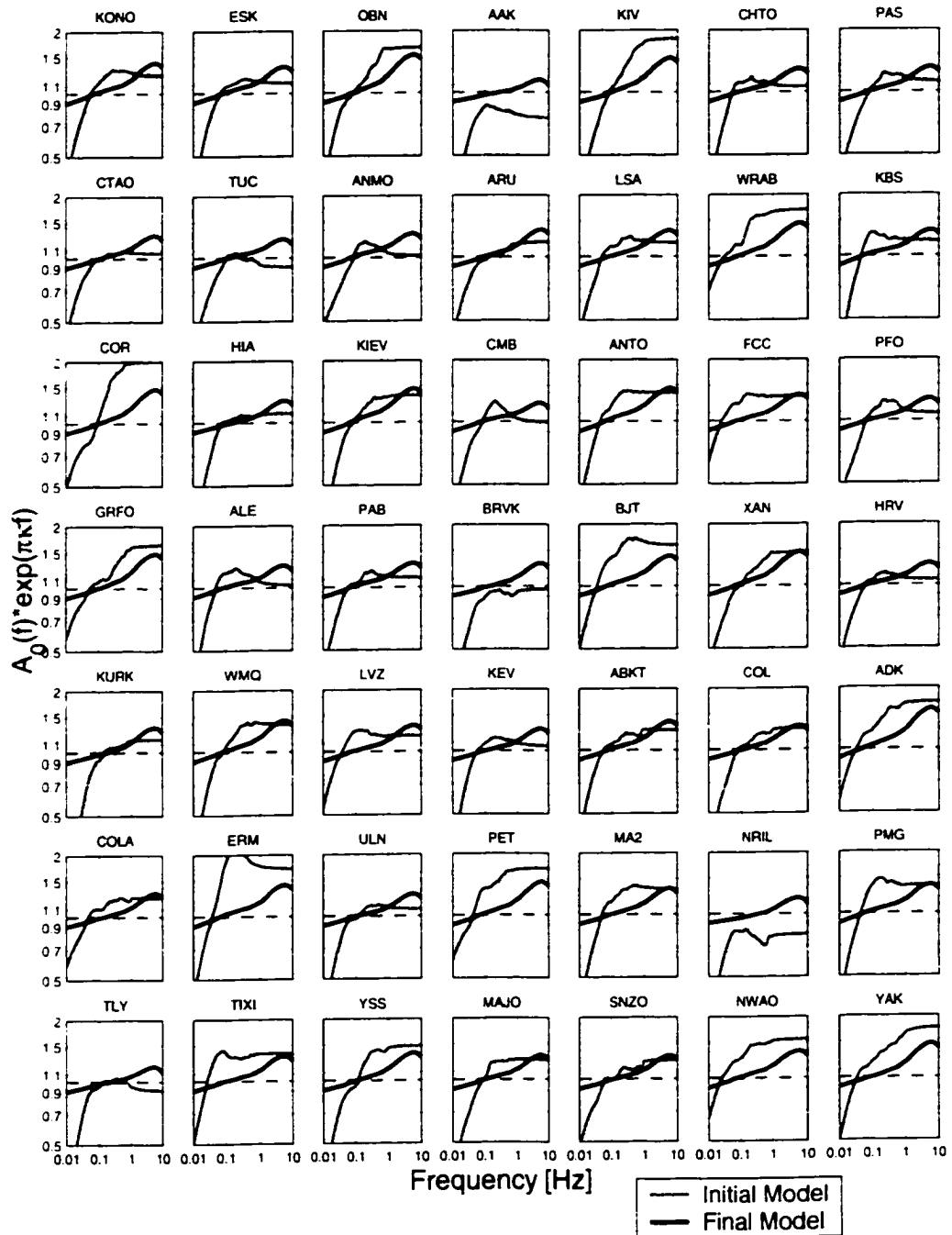


Figure 4-5: Site effect. The green lines represent the squared ratio of equation (4.1), after including the site correction modelled (Figure 4-4), and equation (4.2), and the thick black lines represent the modelled site correction. The red dashed lines represent no site effect. Each plot represents a station.

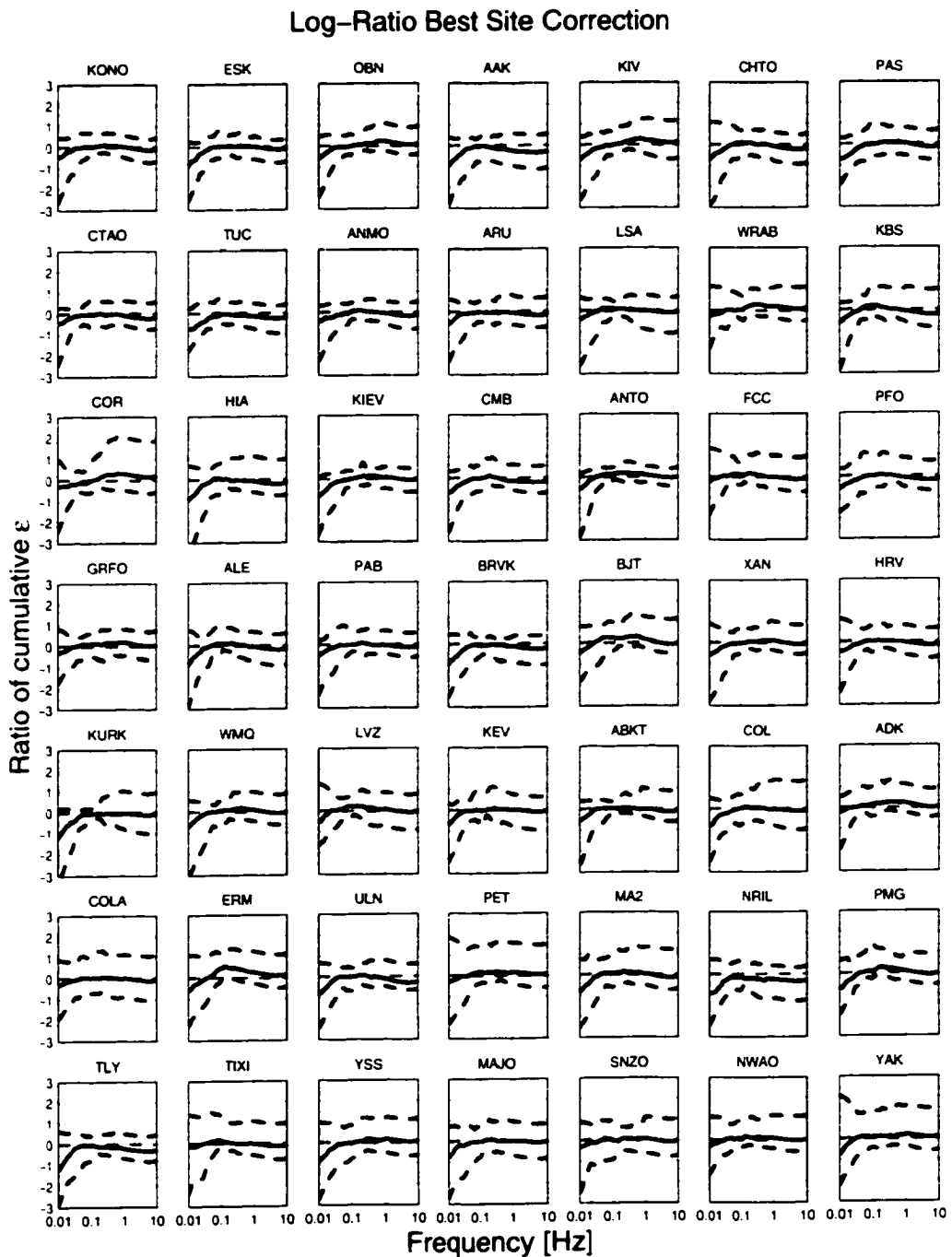


Figure 4-6: Distribution of log-ratio after applying the modelled site correction. Each plot represents a station, the number of the station corresponds to the one listed on Table 4.1. The horizontal black line represents the median of the distribution and the black dashed lines represent the 5% and 95% of the distribution. The horizontal green dashed line represents a good agreement between the cumulative energy estimates.

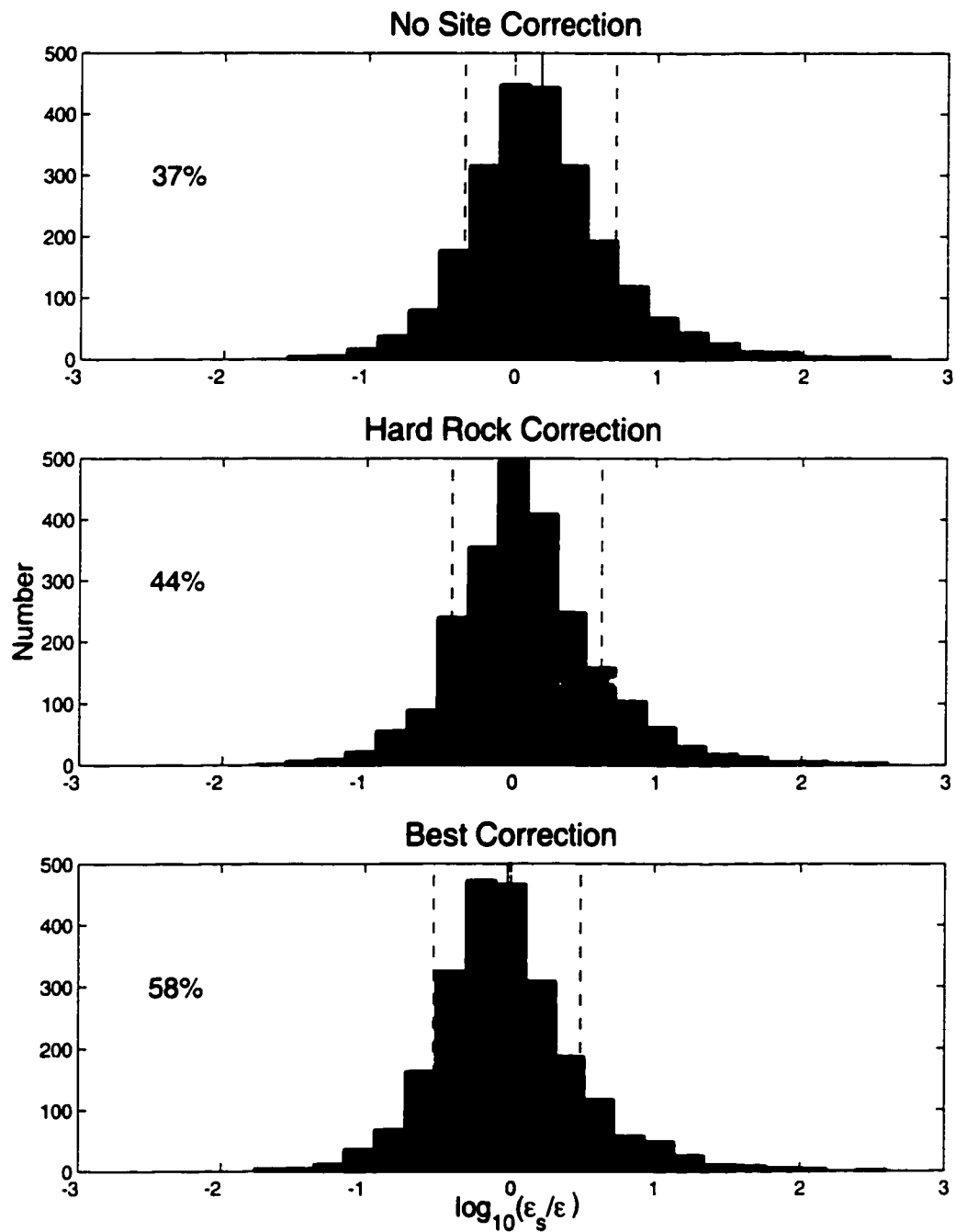


Figure 4-7: Log-ratio distribution. The thick solid lines represent the mean log ratio, the thick dashed lines are the one standard deviation of the mean, and the thin dashed lines represent the values of E_s are equal. The number on the left is the percentage of events (per station) that are under estimated. The top panel is the ratio between the cumulative energy before site correction, the middle panel is after a generic hard-rock correction, and the bottom panel is after the modelled site correction.

Chapter 5

Apparent Stress and Centroid Time Shift: Slow Earthquakes

Pérez-Campos, X, J. McGuire, and G.C. Beroza (2002).

5.1 Abstract

A number of investigators have observed that earthquakes on ocean transform faults are slow, based on the relative amplitude of long period versus short period waves they generated. Moreover, slow precursors, have been identified in some ocean transform earthquakes. Paradoxically, recent studies indicate that ridge-transform events release more seismic energy than other earthquakes of similar size. These two observations seem to contradict each other since the seismic energy is primarily concentrated at and above the corner frequency. In an attempt to reconcile these observations, we analyzed a population of 70 strike-slip earthquakes around the world with moment magnitudes between 5.8 and 8.3. Within this population, we identified a set of events with large centroid time shift given their seismic moment. We also identified four events with exceptionally low apparent stress. These four events were all located on oceanic ridge-transform faults. By including these events in the calculation of the mean apparent stress, we find that the mean apparent stress of continental and oceanic values are not significantly different. We also observe that in contrast to the low correlation between centroid time shift and apparent stress for continental earthquakes, the oceanic ridge-transform earthquakes have a high correlation between these two parameters. Furthermore, for the same ridge transform, there are regular and slow events that occurred at different times. These characteristics imply a significant difference in the faulting process between the oceanic ridge transforms and the continental faults, which might reflect the

different frictional behavior of the ridge-ridge transform faults. We also performed the same analysis for 88 shallow reverse events, identifying only one tsunami earthquake that can be classified as slow, based on its large centroid time shift and low apparent stress.

5.2 Introduction

A number of studies have observed that events located on oceanic transforms are slow. Slow earthquakes are events in which the rupture process is of unusually long duration given the seismic moment. These slow events are identified by their anomalously large amplitudes at low frequencies. This signature has been seen in body waves by *Kanamori and Stewart* [1976] and *Okal and Stewart* [1982] who observed discrepancies between magnitudes measured at long and short periods for events on transform faults; in surface waves by *Shearer* [1994] who noticed that some transform events were anomalously strong relative to their M_S and *Stein and Pelayo*, [1991] who observed that transform-fault events had a larger M_S compared to their body magnitude, m_b ; and in free oscillations by *Beroza and Jordan* [1990] who detected slow earthquakes, with anomalously large characteristic durations, by comparing the spectral levels of the normal mode resonance peaks and those of ambient noise. Also, *Prozorov and Hudson* [1983] defined creepex as the deviation of an earthquake from the orthogonal regression of surface and body magnitudes, a positive creepex denotes similarity to the creep phenomenon. They observed a higher creepex for strike-slip earthquakes than for reverse events; furthermore, they observe high values of creepex in mid-ocean ridges. Some studies have observed an extremely slow rupture component of the order of 100 s for events located on ocean transform [e.g., *Ihmlé and Jordan*, 1994; *McGuire, et al.*, 1996]. All these results suggest that these events were enriched in low-frequency waves and depleted in high frequency waves.

In contrast *Choy and Boatwright* [1995] observed that oceanic transform earthquakes have some of the highest levels of apparent stress, $\tau_\alpha = E_s/M_0$, (rigidity modulus times the ratio between the seismic energy, E_s , and seismic moment, M_0) [*Wyss and Brune*, 1968], for any tectonic regime. Most seismic energy is radiated around and above the corner frequency, so that this result implies that events on ocean transforms are rich in high frequencies. Having both slow earthquakes and high apparent stress for the oceanic transforms seems contradictory.

In this work, we address the origin of this seemingly inconsistent behavior. We estimated

Table 5.1: Ridge-transform earthquakes.

Transform	Date	Lat. [Deg]	Long. [Deg]	ϕ_s, δ, λ [Deg]	M_0 [Nm]	M_w	τ_α [MPa]	Δt [s]
Owen (1)	950526	11.75	57.55	210, 64, 0	6.08E18	6.5	0.01	19.1
Owen (2) [†]	961001	12.30	57.89	207, 73, -7	4.90E18	6.4	20.20	7.8
Romanche	940314	-0.88	-23.03	262, 61, -177	4.11E19	7.0	0.08	25.4
Atlantic	950523	-55.89	-2.14	353, 77, -166	1.48E19	6.7	0.20	15.8
Challenger	970511	-36.46	-98.23	93, 76, 174	6.04E18	6.5	0.17	10.4

Location, focal mechanism, moment, and Δt were obtained from CMT Harvard Catalog. Depth of the events is 15 km, reported by the CMT Harvard Catalog. [†]Event was not identified as slow earthquake.

the apparent stress and obtained the centroid time shift, Δt (centroid time minus the origin time) for a population of 70 strike-slip earthquakes, located in both oceanic and continental crust. The oceanic events occurred either at ridge-ridge transforms or near subduction zones. We found four events with an anomalously large Δt given their M_0 , that are accompanied by a low τ_α (Table 5.1). The low apparent stress is a consequence of their deficiency in high frequency radiation, as reflected in their source spectra. We identify these as slow earthquakes. These events are excluded from the NEIC seismic energy analysis, due to their low signal to noise ratio at ~ 1 Hz. When these events are included in the estimation of the average apparent stress of the oceanic transforms, the value we find is not significantly different than other populations, either in continents or other oceanic zones.

5.3 Large Centroid Time Shift

We used a population of 70 strike-slip earthquakes from 1992 to 2002, with moment magnitudes from 5.8 to 8.3, located both in oceanic or continental crust. These events were selected from the total population of these years based on their magnitude, the number of teleseismic stations that recorded the event (a minimum of five), and a good signal to noise ratio at high frequencies. For each event, we obtained the Δt , location, focal mechanism, and M_0 from the Harvard CMT catalog, identifying candidate slow events by their large centroid time shift for a given seismic moment.

Overall, the centroid time shift scales with seismic moment; as $\Delta t \propto M_0^{1/3}$, as predicted by a constant stress drop assumption; however, it is evident that for a given M_0 , there are some events with an anomalously large Δt (Figure 5-1). From the population of events with large Δt , we find that only four of them have low apparent stress (Table 5.1), i.e. low amplitudes at high frequencies. These events are excluded from the NEIC seismic energy

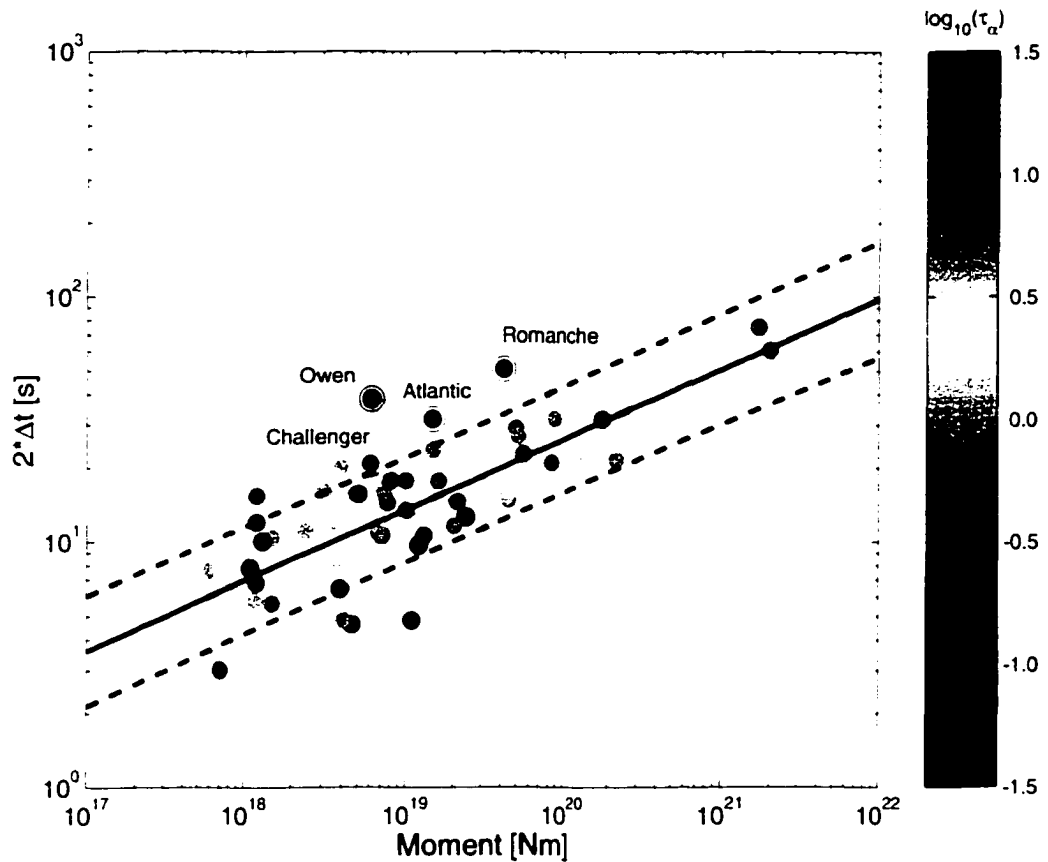


Figure 5-1: Scaling of centroid time shift with moment. The outlined symbols are the events identified as slow. The events are color coded based on their apparent stress, where red is high τ_α and blue is low τ_α . Those events with high Δt given their M_0 are labelled with their source region.

analysis, due to their low signal to noise ratio at ~ 1 Hz. This protocol will bias the dataset to exclude slow events and we believe it is the major source of the slow earthquake and high apparent stress discrepancy for oceanic transform fault events.

5.4 Low Apparent Stress

We estimated E_s for all the events, using the technique described by *Boatwright and Choy* [1986], as revised by *Pérez-Campos and Beroza* [2001], and enhanced in previous chapters of this thesis. We used the IASP91 velocity model [*Kennett*, 1991] for continental earthquakes and an oceanic crustal velocity model for oceanic events. We used a different attenuation

model depending on the source region (Figure 3-2), having a stronger attenuation correction at high frequencies, above 0.3 Hz, for events originating on subduction zones. We used this based on the observation that at subduction zones, such as Japan the attenuation is stronger than the global average [e.g. *Boatwright and Choy, 1989*]. Also, in Chapter 3, we found that to reconcile local and teleseismic seismic energy estimates for events in the subduction zone of Mexico, the attenuation correction had to be stronger at high frequencies than average global models. We also included a site correction, as described in Chapter 4. For the stations listed on table 4.1 we used the site corrections modelled in Chapter 4 and for the rest of the stations, since the GSN stations are mostly located at hard rock sites, we used a site correction for a hard rock environment [*Boore and Joyner, 1997; Boatwright et al., 2002*]. This correction takes into account the amplification and attenuation at the station, is frequency dependent, and can be strong for sites with soft rocks or soils, and tends to lead to over predicting the seismic energy if it is not taken into account.

We calculated τ_α using the corrected E_s estimates, and find that the mean apparent stress for four of the identified earthquakes, $\tau_\alpha = 0.09 + 0.22 / - 0.06$ MPa, is much lower than for the other oceanic events, either ridge-transform or subduction events, $\tau_\alpha = 1.51 + 3.41 / - 1.05$ MPa. However, the mean τ_α for events in continental crust ($2.00 + 4.12 / - 1.35$ MPa) is not significantly different than that for events in oceanic crust ($1.41 + 4.62 / - 1.08$ MPa) or for ridge-transform fault events ($1.22 + 5.71 / - 2.15$ MPa) once we included the four events with low apparent stress. We note that the four slow earthquakes are located on ridge-ridge oceanic transforms not on continents or in other tectonic settings.

Figure 5-2 shows the centroid time shift normalized by the cube root of the seismic moment, and referenced to a $M_0 = 1 \times 10^{18}$ N-m, against the apparent stress. The continental events are indistinguishable from the oceanic (subduction and ridge-transform) events in this plot, with some scatter and a low correlation coefficient (0.1 and 0.2, respectively). However, the ridge-transform events including the four identified earthquakes, represent a different population with a larger correlation coefficient of 0.65. These events are characterized by both a very low apparent stress and a large centroid time shift (Table 5.1), and can be classified as slow earthquakes. Their spectral characteristics indicate that they have a rich low-frequency component.

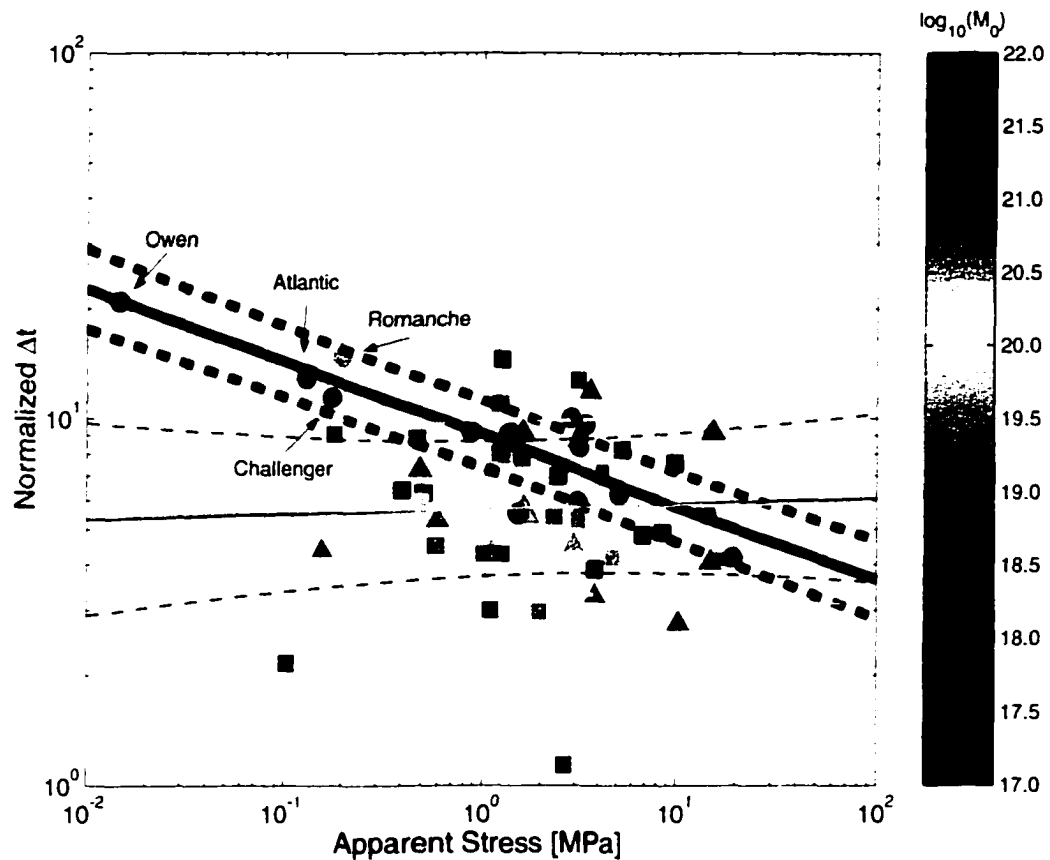


Figure 5-2: Moment normalized centroid time shift vs apparent stress. Triangles are for continental earthquakes; squares are for oceanic events, excluding those at ridge or rise transforms, which are given on circles; the outlined symbols are for the identified slow events. The symbols are color coded proportional to the seismic moment of the event. The solid lines represent the best fit for the respective population and the dashed line is the $\sim 95\%$ confidence intervals of the regression. The thin red lines are for the continental events; the thin blue lines are for the oceanic events excluding the ridge and rise transforms; and the thick dark blue lines are for the ridge and rise transform events, including the slow events.

5.5 Signal Characteristics

For two events with the same moment, we expect to observe very different signals, both in the time and the frequency domain, for a regular event, a multiple event, and a slow event. For the first two, the spectra might be similar, with a similar corner frequency and spectral decay, but the centroid time shift is going to be larger for the multiple event. When we compare against a slow event, the centroid time shift might be as large as that one for a

multiple event; however, the spectrum is going to be different, having a much lower corner frequency than a regular or a multiple event (Figure 5-3).

We compared two events with similar seismic moment, both located in the Arabian Sea, on the Owen transform fault (Figure 5-4). Even though they have similar M_0 , their Δt are very different (Table 5.1); this should be reflected in their corner frequency, and the fact that they also have a different τ_α should be manifested with different amplitudes at high frequency. Comparing the source spectra of these two events, the regular event has a higher corner frequency than the slow event. At ~ 0.05 Hz, the seismic energy is comparable for both events, after that, the slow event is depleted (Figure 5-5).

Comparing the same events at the station ATD (Figure 5-4), in figure 5-6, the broadband signals are very different; however, after applying different low pass filters, up to 20 s, the time signals are similar to each other. Not surprisingly, if we track the cumulative energy with increasing frequency, the signals accumulate energy at the same rate up to 0.05 Hz, but at higher frequencies, the slow event is depleted. It is also interesting to note that after applying the filters of 10 and 20 s, the arrival times are the same but they still present difference on the slope of the first pulse.

Abercrombie and Ekström, [2001] argued that at least some, and perhaps all, previously identification of slow earthquakes on oceanic transforms were suspect. Much of this argument is based on the effect of crustal structure in the source region and the uncertainties in the modelling procedure. Our observations of the Owen transform events suggest that some oceanic transform events are, indeed, slow, since these events occur adjacent to one another. More generally, our teleseismic estimates of seismic energy take into account the uncertainty in location and focal mechanism. We observe that the four selected events have spectra depleted at high frequencies, allowing us to classify them as slow earthquakes.

5.6 Discussion

Ide et al. [2001] observed a good correlation between the apparent stress and the Brune stress drop for small earthquakes. If this were also valid for large earthquakes, our observations would imply that the slow event has a very small Brune stress drop, which seems to be unfeasible, since we would need an unrealistically large source dimension to match the given M_0 .

Another option is that the slip during the earthquake was slow and/or that the rupture

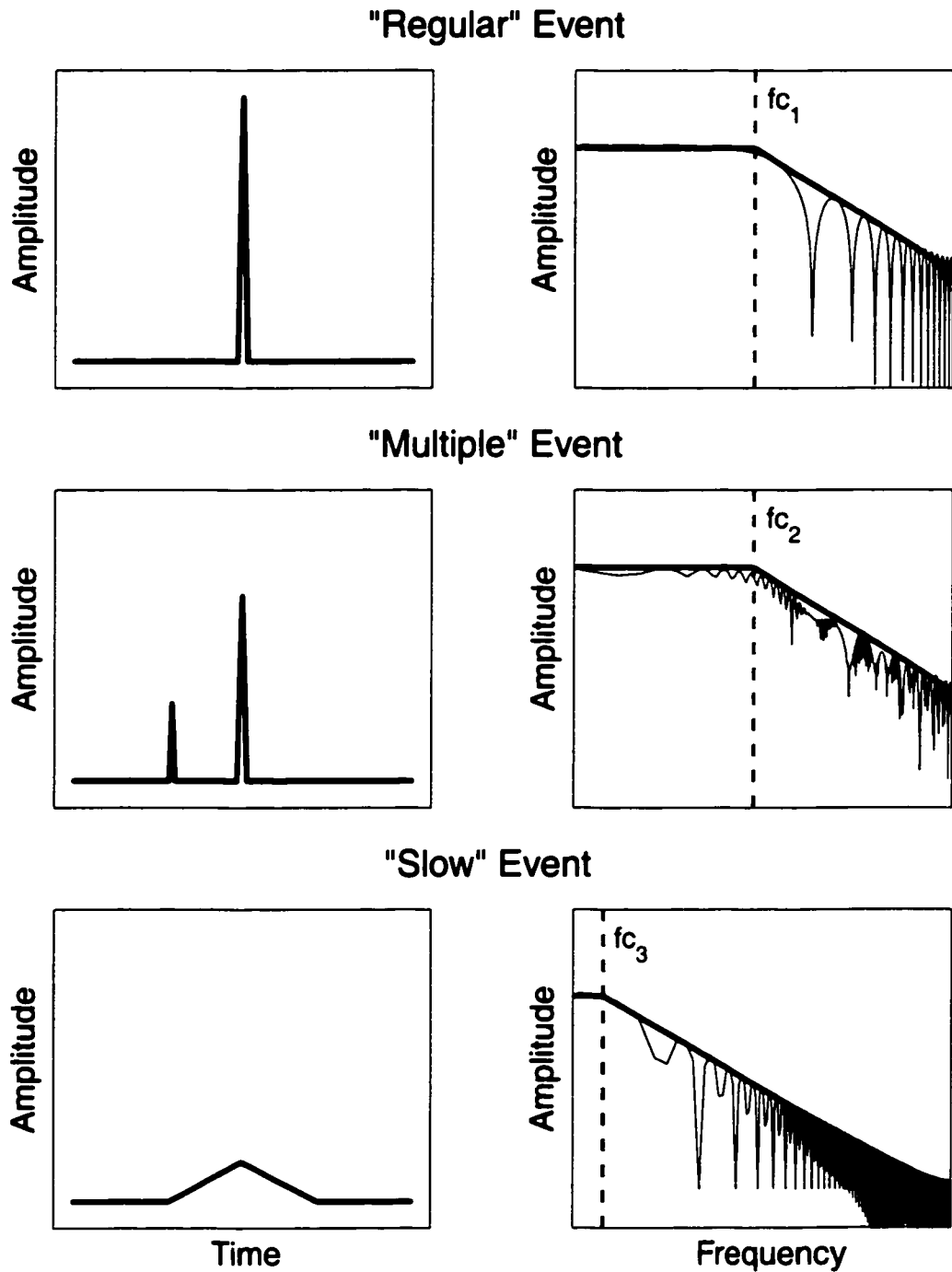


Figure 5-3: Options for having a long centroid time shift. The panels on the left are on the time domain and the right panels are in the frequency domain. The centroid time shift is larger for the multiple and the slow event in contrast to the regular event, but the corner frequencies are different, being $f_{c1} \approx f_{c2} \gg f_{c3}$. This is assuming an omega-square model for the spectral decay [Aki, 1967].

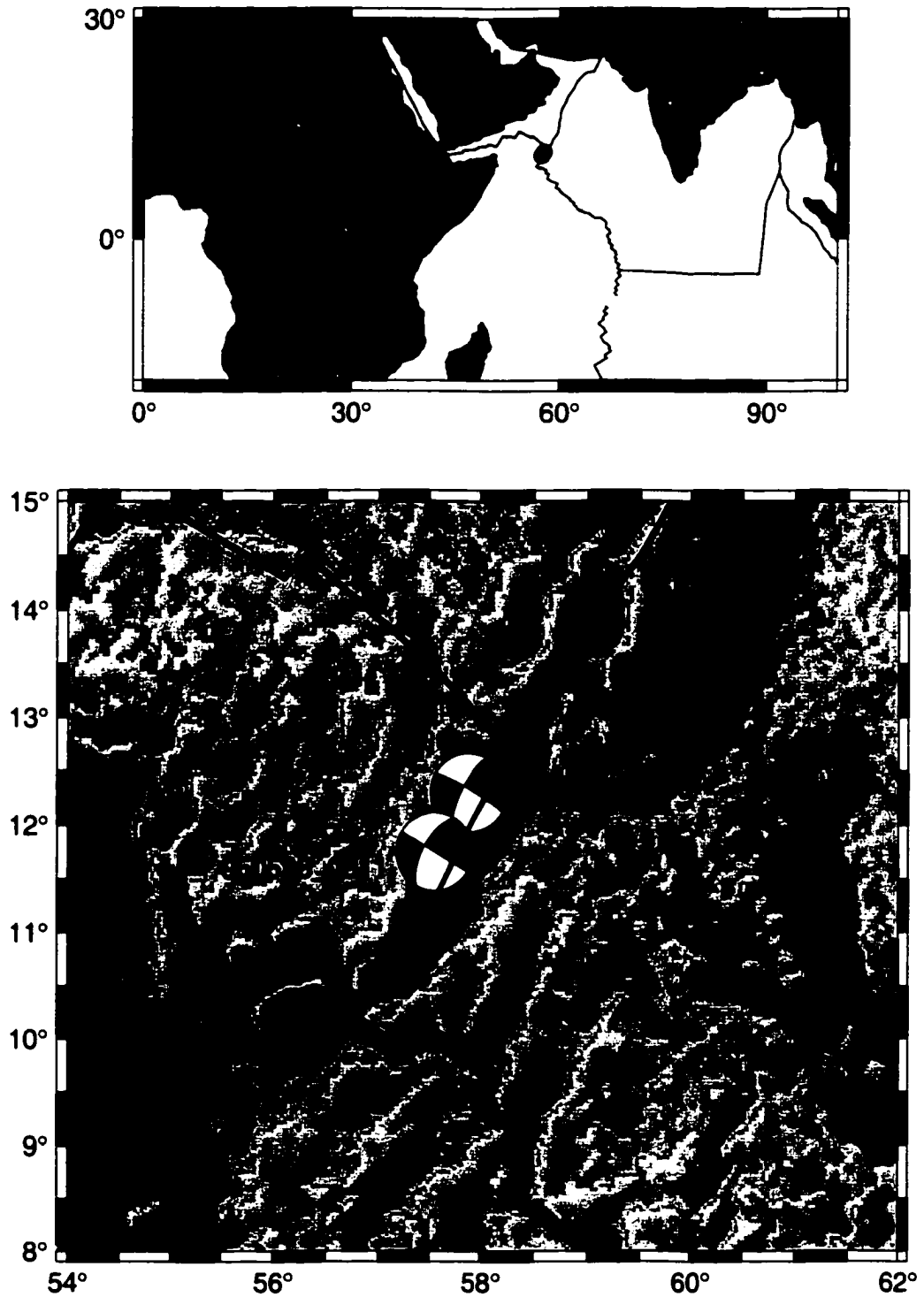


Figure 5-4: Location of the two events on the Owen fault and the location of station ATD.

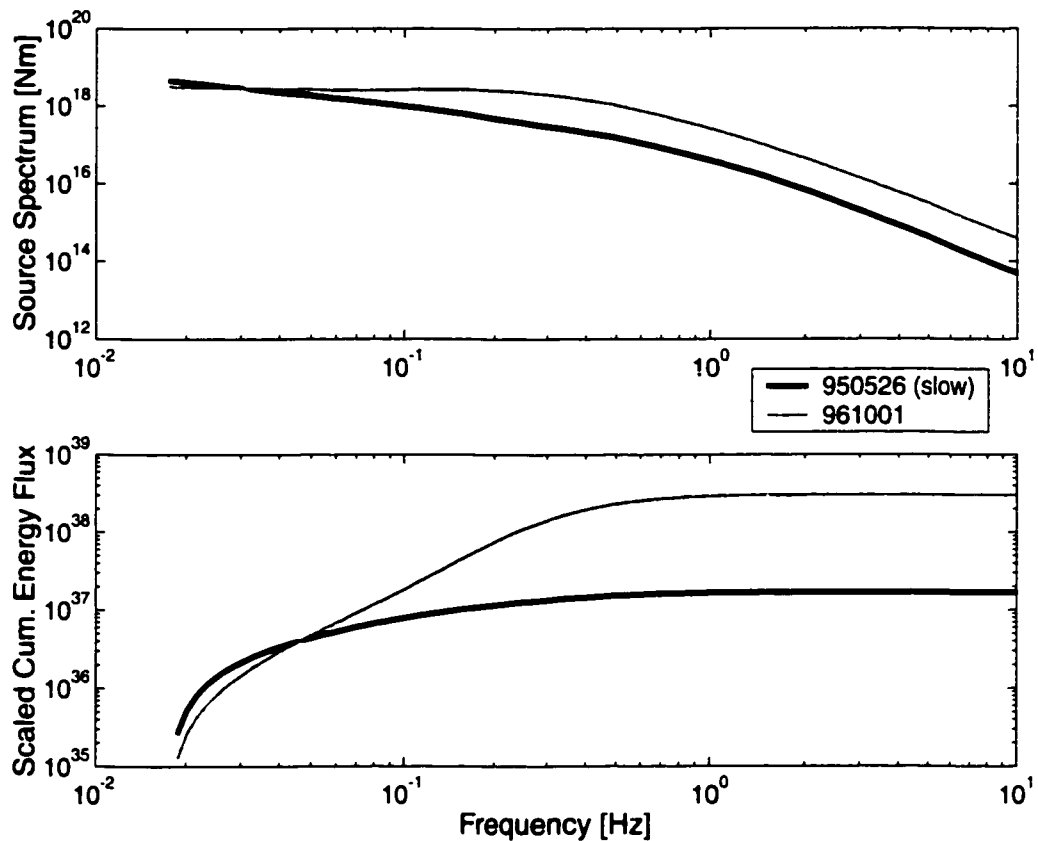


Figure 5-5: The top panel is the comparison of the smoothed source spectrum of the slow event (black) and the regular event (gray) and the bottom panel compares the accumulation of the seismic energy released by each event with respect to frequency. The smoothed spectra were obtained using a loess function, with a linear interpolation for a 0.5 neighborhood parameter [Cleveland, 1993].

velocity is low due to frictional properties of the transform faults. This suggests that the rupture process for transform faults must be different, dissipating less energy radiated as seismic waves and more energy as heat, and/or fracture energy.

Mikumo [1981] discussed the possibility of the occurrence of a slow earthquake and a normal earthquake at different times, arguing that the strength of the asperities would become different at the time of a succeeding earthquake. In the case of the Owen events, given the CMT Harvard Catalog locations, their rupture areas probably did not overlap, making it impossible to rule out absolutely that the fault has strongly different frictional properties in the two places. However, given the similarity of these adjacent fault areas, we consider this unlikely.

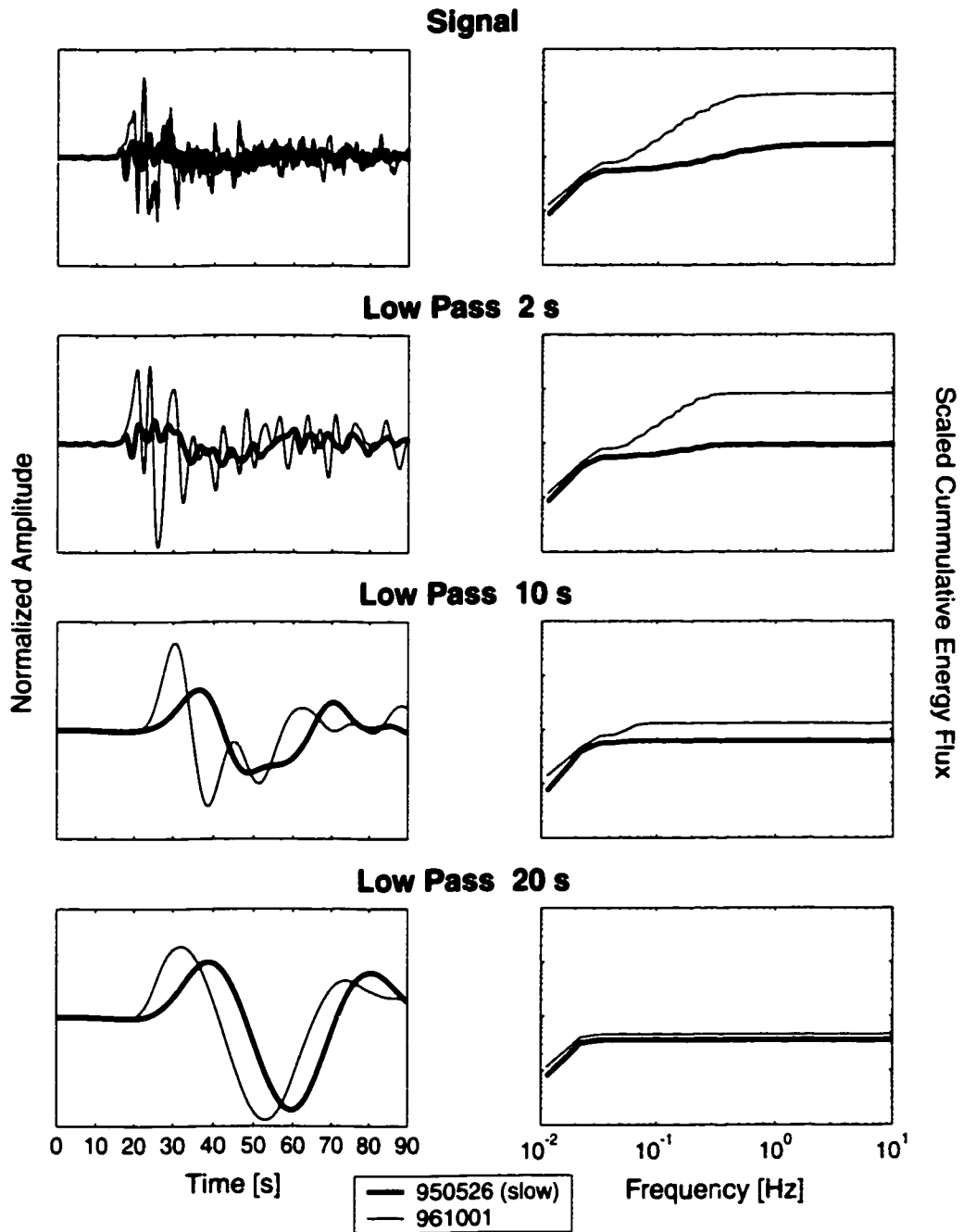


Figure 5-6: Comparison of the slow event (thick black line) and the regular event (thin gray line) at the same station ATD. The left panels are the time domain signals and the right panels are the cumulative seismic energy with frequency. The top panels are the original signals, then after applying a low pass filter at 2 seconds, at 10 seconds and at 20 seconds at the bottom. The original signals are aligned at the arrival times.

The apparent stress is a measure of how energetic an earthquake is with respect to its size. For a given value of M_0 there is a wide range of values of τ_α . This dispersion is at least partially explained by the uncertainty in the estimates of the seismic energy; however, we believe that after the improvements described in this thesis, the uncertainty is substantially reduced and that much of the dispersion observed in τ_α is real, and a signature of the source process.

The four strike-slip events classified here as slow earthquakes are located on ridge-transform faults; however when we include all events on ridge-transform faults systems we find that they are characterized neither by slow events nor by high apparent stress. They have regular events with high apparent stresses but also slow events with low apparent stresses that reduced the characteristic τ_α of the ridge transforms to similar characteristic τ_α of other tectonic settings.

5.7 Tsunami Earthquakes: Slow?

A large magnitude shallow earthquake, located near a subduction zone beneath the ocean floor can produce a tsunami [Shapiro *et al.*, 1998; Polet and Kanamori, 2000], which in that case it is called a tsunamigenic earthquake. The amplitude of the tsunami is proportional to the seismic moment of the earthquake that generated it [Abe, 1979], making the size of the earthquake one of the most important parameters determining its tsunami potential [Polet and Kanamori, 2000]. Kanamori [1972] defined a tsunami earthquake as that one that generates a significantly larger tsunami than predicted. These events have been observed to occur in and near subduction zones [Shapiro *et al.*, 1998]. Anomalously large tsunamis have been explained as the result of an slow earthquake, submarine or land slumping, volcanic activity, rupture reaching the ocean floor in nonaccreting margins where the sediments are subducted along a plate interface, or the subduction of a seamount [Polet and Kanamori, 2000; Abercrombie *et al.*, 2001]. Shapiro *et al.* [1998] used the ratio of the total energy to the high-frequency energy, as a discriminant for tsunamigenic earthquakes, observing that the tsunami events have a high content of low frequencies and are depleted at high frequencies. Previous studies have described tsunami events as slow earthquakes [Kanamori and Kikuchi, 1993; Newman and Okal, 1998; Polet and Kanamori, 2000]. This result has been revised by Abercrombie *et al.* [2001] who argued that while the 1992 Nicaragua earthquake was well described as a slow event, the tsunami genesis of 1994 Java earthquake

Table 5.2: Tsunami earthquakes.

No.	Event	Date	Lat. [Deg]	Long. [Deg]	Depth km	ϕ_s, δ, λ [Deg]	M_0 [Nm]	M_w	τ_α [MPa]	Δt [s]
1	Nicaragua	920902	11.20	-87.81	15	303, 12, 91	2.40E20	7.6	0.017	44.5
2	Indonesia	921212	-8.48	121.90	28	65, 47, 61	1.40E20	7.7	1.72	22.5
3	Java	940602	-10.48	112.84	18	278, 5, 90	5.20E20	7.8	0.35	39
4	Peru	960221	-9.59	-79.59	10	347, 4, 95	1.50E20	7.5	0.01	22.7

Location, focal mechanism, moment, and Δt were obtained from CMT Harvard Catalog. Depth of the events is 15 km, reported by the CMT Harvard Catalog.

could be better described as the result of slip over a subducting seamount.

5.7.1 Tsunami Earthquakes: Data

As noticed from the previous section, the apparent stress and the centroid time shift together appear to be indicative of the events with long duration that are depleted at high frequencies, characteristics of a slow earthquake. We use a set 88 shallow (depth < 35 km) reverse earthquakes around the world with M_w between 5.9 and 8.2 to search for similar behavior (large Δt and low τ_α). This dataset includes four earthquakes (Table 5.2) previously identified as tsunami earthquakes in the literature [*Kanamori and Kikuchi, 1993; Newman and Okal, 1998; Polet and Kanamori, 2000; Abercrombie et al., 2001*]. In a similar fashion as for the strike-slip dataset, we obtained Δt , location, focal mechanism, and M_0 from the Harvard CMT catalog and estimated their τ_α from the values of E_s obtained using teleseismic stations.

5.7.2 Tsunami Earthquakes: Results

Following the same analysis described for the strike-slip events, figure 5-7 shows the centroid time shift against seismic moment, and figure 5-8 shows the normalized centroid time shift against apparent stress. From these figures we find that one of the tsunami events have high apparent stress and large centroid time shift (event 2 in Table 5.2); on the other hand, other three of the tsunami events have a large centroid time shift and low apparent stress (events 1, 3, and 4 in Table 5.2); however, only the 1992 Nicaragua earthquake (event 1 in Table 5.2), previously described as a slow earthquake [*Kanamori and Kikuchi, 1993; Ihmlé, 1996; Polet and Kanamori, 2000; Abercrombie et al., 2001*], is at all exceptional. Other tsunamigenic earthquakes do not deviate greatly from average behavior and can be consider normal events with respect to both Δt and τ_α . The controversial 1994 Java

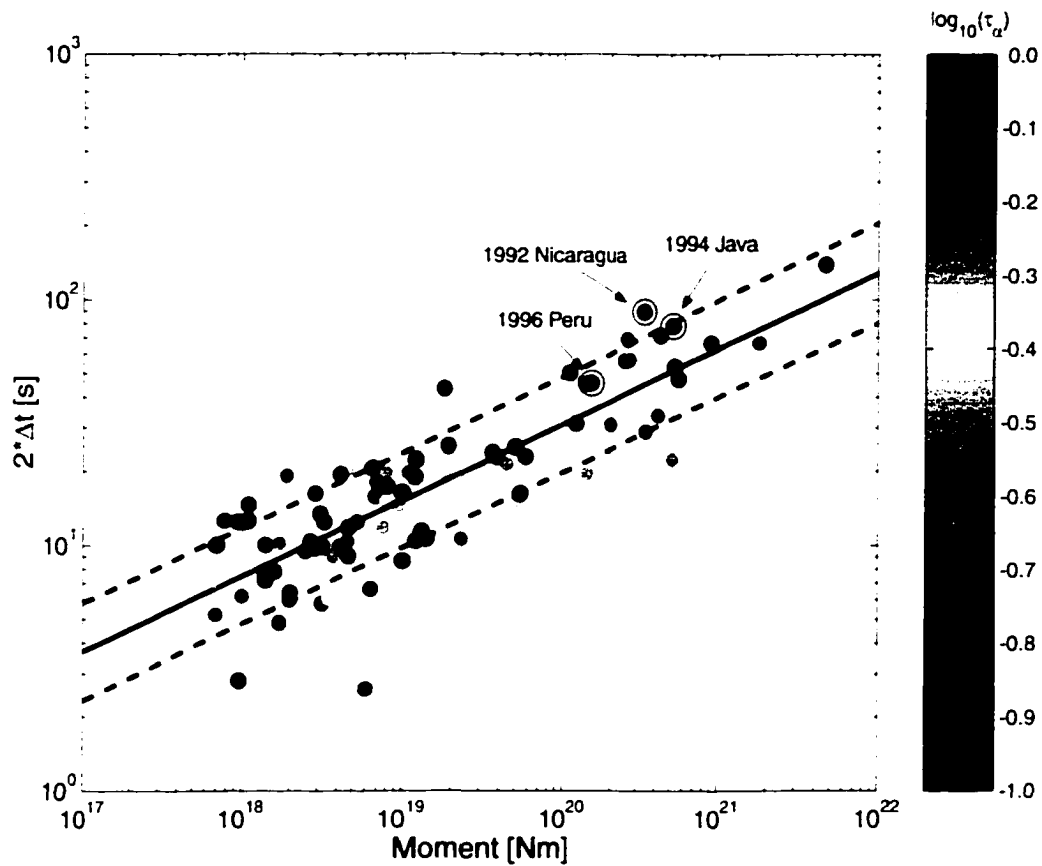


Figure 5-7: Scaling of centroid time shift with moment for shallow reverse earthquakes. The outlined symbols are events identified in the literature as tsunami earthquakes. The events are color coded based on their apparent stress, where red is high τ_α and blue is low τ_α .

earthquake does have a low τ_α but its Δt can be considered normal, such that we do not classify it as a slow earthquake; this agrees with *Abercrombie et al.* [2001] interpretation. The 1996 Peru event has also a low apparent stress, but its centroid time shift could be considered normal, from this we do not classify this event as slow earthquake as well. On the other hand, the 1992 Flores Island, Indonesia earthquake had a large apparent stress and its tsunami was not as a direct result of the earthquake but most likely of a triggered landslide [*Polet and Kanamori, 2000*].

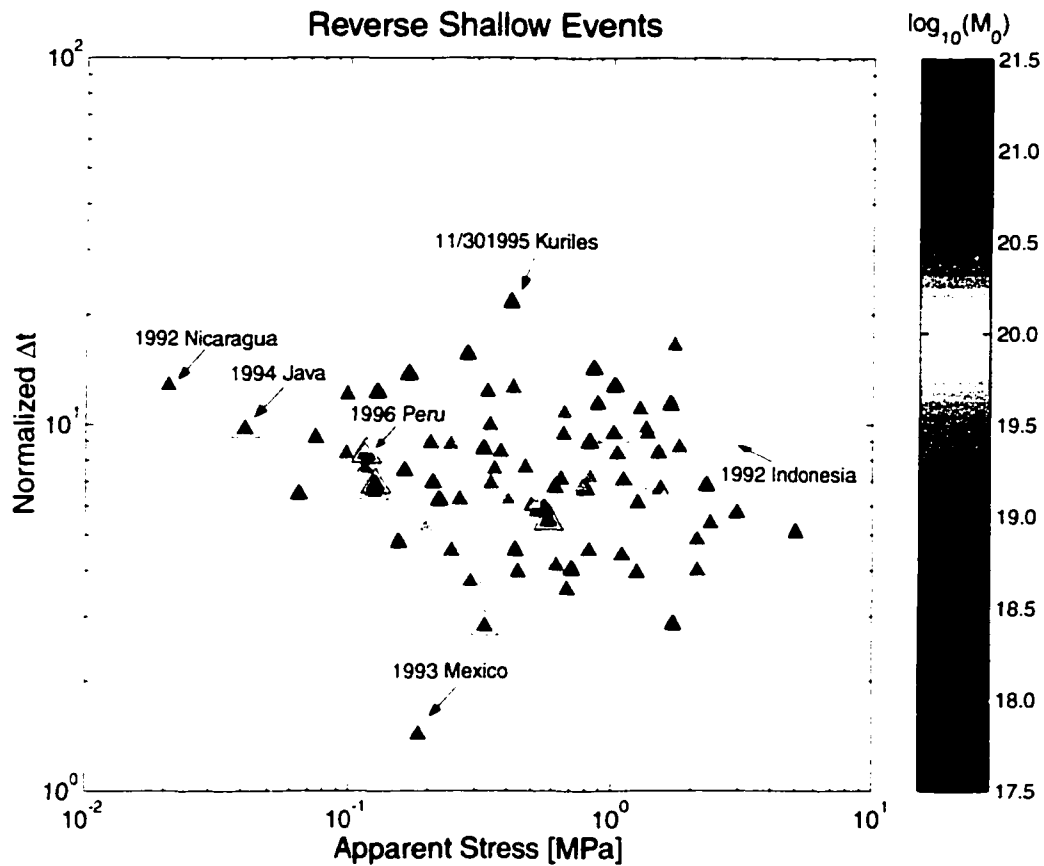


Figure 5-8: Moment normalized centroid time shift vs apparent stress. The outlined symbols are for the tsunami events. The symbols are color coded proportional to the seismic moment of the event. The solid lines represent the best fit for the respective population and the dashed line is the $\sim 95\%$ confidence intervals of the regression.

5.7.3 Tsunami Earthquakes: Discussion

Polet and Kanamori [2001] suggested that the duration and seismic energy could be used as a fast discriminant of a high tsunami potential of an event. From this work we conclude that the apparent stress and the centroid time shift can be used as a discriminant for slow earthquakes. It can also be used as a discriminant of the tsunami potential if we only consider the earthquake as the cause of the tsunami. This can be observed in figure 5-9, which shows only the tsunamigenic events from the dataset of reverse earthquakes. They are color coded by tsunami magnitude [*Iida et al.*, 1967], obtained from tsunami event database of the National Oceanic Atmospheric Agency (NOAA). Two of the highest

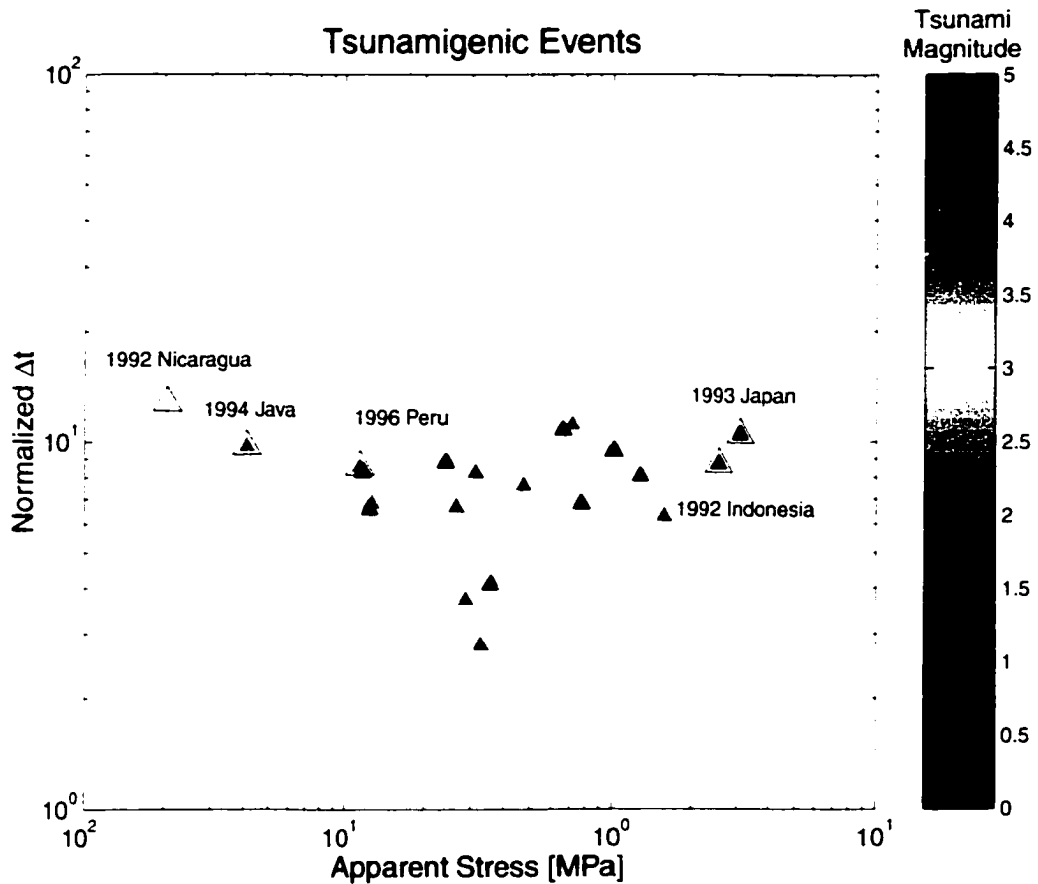


Figure 5-9: Moment normalized centroid time shift vs apparent stress for tsunamigenic earthquakes. The outlined symbols are for the tsunami events. The symbols are color coded proportional to the tsunami magnitude [Iida *et al.* 1967]. The solid lines represent the best fit and the dashed line is the $\sim 95\%$ confidence intervals of the regression.

tsunami magnitudes correspond to the two lowest apparent stresses; however, there are other two events with high tsunami magnitude but with high apparent stress. A low apparent stress together with a large centroid moment shift suggest a slow event, which can generate a tsunami larger than expected. For this reason, these two parameters together should be paid special attention when predicting the size of a tsunami. However, special situations should be taken into consideration, such as the bathymetry of the source region or possible triggered landslides.

5.8 Conclusions

From our analysis we conclude that the events identified as slow earthquakes, all located on oceanic ridge transforms, can be characterized by their large centroid time shift and low apparent stress. These events are deficient in high frequencies. These characteristics distinguish them from regular or multiple events. When these low apparent stress events are included in the calculation of characteristic τ_α , we cannot distinguish the average apparent stress between continental and oceanic events or from ridge transform earthquakes and other tectonic setting events (see Appendix A).

5.9 Acknowledgments

R. Abercrombie for discussion about transform events. This research was supported by NSF grant EAR 9909479. J. McGuire was supported by an NSF Postdoctoral fellowship. Xyoli Pérez-Campos was partially supported by SEP, Mexico and DGAPA, UNAM.

Chapter 6

Seismic Energy Distribution From Strong Motion Models: Scenarios

Pérez-Campos, X, Ide, S., and G.C. Beroza (2002)

6.1 Abstract

The total seismic energy can be estimated directly from seismograms as discussed in chapters 2, 3, and 4; however, this approach does not allow us to study the spatial characteristics of the radiated energy on the fault and how the energy might be dissipated during the rupture process. In this study we use the method of *Ide* [2002] to estimate the radiated energy distribution on the fault plane. We modelled three California earthquakes, the 1984 Morgan Hill ($M=6.2$), the 1992 Landers ($M=7.2$), and the 1999 Hector Mine ($M=7.1$) earthquakes. We find that the radiated energy distributions from these earthquakes have their highest concentration at the main asperities, and that these asperities have energy absorbing regions (sinks) at their edges. We estimate the apparent stress distribution on the fault plane using the moment density, the energy density, and the shear modulus. This distribution shows that the apparent stress is highest at the center of the high slip regions and negative, i.e. showing a stress increase, at regions of energy absorption, primarily the edges of the high slip regions. In general, the total seismic energy estimated from rupture models is underestimated by at least a factor of ~ 2 , this is mainly a result of the frequency range, the rupture velocity, and the grid used in the rupture modelling. However, the spatial distribution of seismic energy highlights the inhomogeneity of fault characteristics and frictional behavior.

6.2 Introduction

In previous chapters we focused on the estimation of the total radiated energy as seismic waves, using the integral of the squared velocity spectrum obtained from seismograms after corrections for radiation pattern, attenuation, geometrical spreading, and site effect. However, this value gives us only the total amount of seismic energy, not where on the fault it was radiated from. Total seismic energy can help us to evaluate the average earthquake properties but not how different parts of the fault might behave. In this chapter I focus on the seismic energy distribution at the source.

Previous studies have also mapped the distribution of seismic energy on the fault, using the slip history on the fault plane. *McGarr and Fletcher* [2000] and *McGarr and Fletcher* [2001] estimated apparent stress for each subfault of the 1994 Northridge earthquake using the slip model of *Wald et al.* [1996]. They observed that the apparent stresses causing the slip were inhomogeneous and concluded they were limited by the strength of the crust. Furthermore, they found that most of the energy was released by only 15% of the fault. *Pulido and Irikura* [2000] calculated the distribution of energy from the moment rate given at each subfault for the 1992 Landers earthquake in order to estimate the apparent stress and the critical slip weakening distance. However, these studies have neglected the effect of slip on neighboring areas of the fault, i.e., the stress change produced by the surrounding subfaults. *Ide* [2002] estimated the distribution of the seismic energy on the fault from the slip and stress histories for the 1995 Kobe earthquake, using the foundation of *Kostrov* [1974] and *Rudinicki and Freund* [1981]. Here, we apply his technique to estimate the distribution of the seismic energy for three California earthquakes: the 1984 Morgan Hill earthquake, the 1992 Landers earthquake, and the 1999 Hector Mine earthquake.

The first two events had predominantly unilateral rupture propagation [*Beroza and Spudich*, 1988; *Cohee and Beroza*, 1994]. The Hector Mine earthquake was bilateral, with slip concentrated beneath and SSE of the hypocenter [*Dreger and Kaverina*, 2000]. We used finite-source models of these earthquakes to determine the distribution of the radiated seismic energy [*Ide*, 2002].

For the three events, we observe that the largest amount of seismic energy radiated coincides with areas of large slip and is not necessarily concentrated near the hypocenter. At the boundaries of the high slip regions, we find areas of energy absorption. We estimate the distribution of the apparent stress on the fault, which is also concentrated at the high

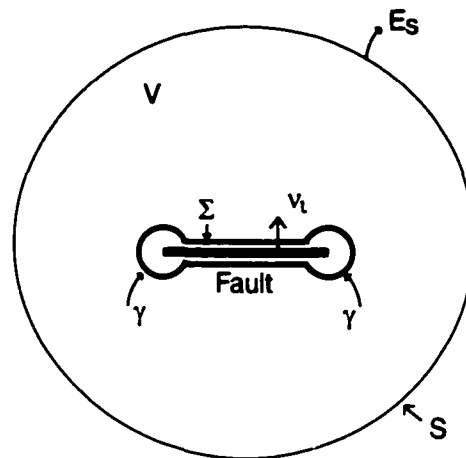


Figure 6-1: Domains of integration for the energy balance.

slip regions, but spread over a larger area than E_s , with regions of negative values where energy is absorbed. We also calculate the static stress drop distribution using the method of *Andrews* [1980]. When comparing the total values of E_s obtained from the rupture model to values estimated previously, we find that the estimate based on the rupture model underpredicts the seismic energy by up to an order of magnitude for the 1992 Landers earthquake by a factor of ~ 2 for the 1999 Hector Mine earthquake. This underprediction is presumably related to the bandlimited nature of the data used in the finite-source rupture modelling on which the estimate is based.

The distribution of the radiated energy suggests that frictional characteristics vary strongly on the fault. Also, there are zones where the stress change is in the opposite direction, i.e. there is a stress increase and a region of energy absorption.

6.3 Energy Balance

We treat an earthquake as a running shear crack. The energy involved in this process is given by the work done by external forces; the change in internal strain energy, U_e ; the surface energy involved in creation of the crack U_s ; the kinetic energy, U_k ; and the work done against friction, U_f . Conservation of energy and choosing a large enough volume, leads to the relation [Scholz, 1990]:

$$E_s = \Delta U_k = -\Delta U_e + \Delta U_f + \Delta U_s \quad (6.1)$$

Choosing a large enough volume, the seismic energy can be expressed in terms of the characteristics of the slip, $\Delta u_i(\mathbf{x}, t)$, and the stress $\sigma_{ij}(\mathbf{x}, t)$ on the fault plane Σ [Kostrov, 1974]:

$$E_s = \frac{1}{2} \int_{\Sigma} (\sigma_{ij}(\mathbf{x}, 0) - \sigma_{ij}(\mathbf{x}, \infty)) \Delta u_i(\mathbf{x}, \infty) \nu_j dS - \int_{\Sigma} \gamma(\mathbf{x}) dS + \int_0^{\infty} dt \int_{\Sigma} \dot{\sigma}_{ij}(\mathbf{x}, t) \Delta u_i(\mathbf{x}, t) \nu_j dS, \quad (6.2)$$

where ν_j is a fault normal vector (Figure 6-1), $\dot{\sigma}$ denotes the time derivative of stress, and $\gamma(\mathbf{x})$ is the surface energy to extend the rupture plane. If there is no stress singularity around the rupture front, $\gamma(\mathbf{x}) = 0$ [Ide, 2002]. If in addition, we assume that the stress drops an amount $\Delta\sigma$, from $\sigma_{ij}(\mathbf{x}, 0)$ to $\sigma_{ij}(\mathbf{x}, t)$, that rapid variations in stress are present during rupture [Kostrov, 1974], that $\sigma_{ij}(\mathbf{x}, t)$ is equal to a constant frictional stress, and neglect the energy in the near-field high-frequency accelerations, the seismic energy can be simply estimated by

$$E_s = \frac{1}{2} \Delta\sigma \overline{\Delta u} A \quad (6.3)$$

where $\overline{\Delta u}$ is the average slip [Kostrov, 1974] and A is the fault area. This shows that the seismic energy contains information related to the stress change during an earthquake. Figure 6-2 shows a simple model of how seismic energy is related to the change of stress, through the slip-weakening model. Macroscopically, the total seismic energy has been related to the total stress drop. This figure depicts an earthquake as a point process; however, in this study, with the slip and stress history along the fault we can detail the fault frictional behavior and how the seismic energy is dissipated in the fault zone.

6.4 Seismic Energy from Rupture Models

In order to calculate the radiated energy from a heterogeneous finite-fault model, we need to use a numerical method. We will follow Ide [2002] using a finite difference method.

First, the elasto-dynamic equations are solved by the finite difference method described by Ide and Takeo [1997], where they used the slip distribution as a boundary condition.

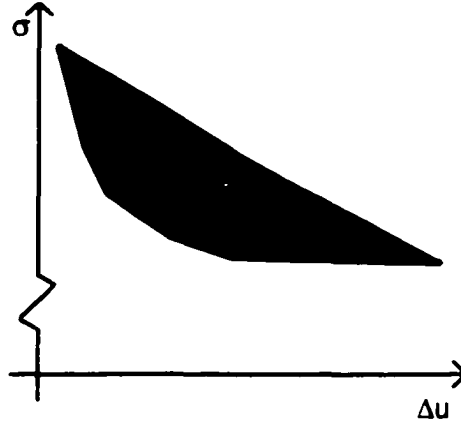


Figure 6-2: Slip-weakening model. The gray area represents the energy released as seismic waves by an earthquake.

Following *Ide and Takeo [1997]*, the equations of motion,

$$\rho \ddot{u}_i = \tau_{ij,j}, \quad (6.4)$$

and Hooke's law,

$$\tau_{ij} = \lambda u_{k,k} \delta_{ij} + \mu (u_{i,j} + u_{j,i}), \quad (6.5)$$

are solved in a 3-D elastic body surrounded by a fault plane, a free surface, and four other rigid boundaries whose effects are negligible. u_i represents the i component of the displacement vector and τ_{ij} , the ij component of the stress tensor; $,j$ means partial derivative in j direction; ρ is density, λ and μ are elastic coefficients, and δ_{ij} is the Kronecker delta. The coordinate system adopted for the case of a vertical strike-slip fault is x in the strike direction, y perpendicular to the fault, and z vertical. Combining equation (6.4) and (6.5), the following wave equations are obtained:

$$\begin{aligned} \ddot{u}_x &= \frac{\lambda + \mu}{\rho} \frac{\partial^2 u_x}{\partial x^2} + \frac{\mu}{\rho} \nabla^2 u_x + \frac{\lambda + \mu}{\rho} \frac{\partial^2 u_y}{\partial x \partial y} + \frac{\lambda + \mu}{\rho} \frac{\partial^2 u_z}{\partial x \partial z}, \\ \ddot{u}_y &= \frac{\lambda + \mu}{\rho} \frac{\partial^2 u_x}{\partial x \partial y} + \frac{\lambda + \mu}{\rho} \frac{\partial^2 u_y}{\partial y^2} + \frac{\mu}{\rho} \nabla^2 u_y + \frac{\lambda + \mu}{\rho} \frac{\partial^2 u_z}{\partial y \partial z}, \\ \ddot{u}_z &= \frac{\lambda + \mu}{\rho} \frac{\partial^2 u_x}{\partial x \partial z} + \frac{\lambda + \mu}{\rho} \frac{\partial^2 u_y}{\partial y \partial z} + \frac{\lambda + \mu}{\rho} \frac{\partial^2 u_z}{\partial z^2} + \frac{\mu}{\rho} \nabla^2 u_z. \end{aligned} \quad (6.6)$$

Given every boundary condition by displacements, equations (6.6) can be solved for each time step. Assuming symmetry across the fault plane ($y = 0$), the displacements in x and z on the plane are given as half of the slip of the kinematic model. The fault normal traction, due to symmetry, reduces to

$$\tau_{yy} = 0, \quad (6.7)$$

which determines the value of u_y on the plane. The free surface has a traction free boundary condition, i.e.,

$$\tau_{xz} = \tau_{yz} = \tau_{zz} = 0, \quad z = 0. \quad (6.8)$$

Once every displacement in the elastic medium is determined, the stress components other than τ_{yy} are calculated using equation (6.5). Now that slip and stresses histories are known on the fault, we can use equation (6.2) to estimate the radiated energy on the fault plane. *Ide* [2002] found that this method underestimates the energy when the grid used is coarse, especially when there are high rupture propagation velocities, close to the S -wave propagation velocity.

6.5 Energy Distribution: Real Earthquakes

Ide [2002] obtained the distribution of seismic energy from the rupture models of the 1995 Kobe earthquake ($M = 6.9$), the 1997 Kagoshima earthquake ($M = 6.1$), and the largest event in the 1998 Hida-Mountain earthquake swarm ($M = 5.1$). He observed that energy was radiated primarily from near the hypocenter and from the initial rupture of asperities; however, for each of these events, most of the slip was concentrated near the hypocenter. In this study we used three California earthquake models, the 1984 Morgan Hill, the 1992 Landers, and the 1999 Hector Mine earthquakes. Each of these events had considerable slip far from the hypocenter. In addition, the 1992 Landers earthquake and the 1999 Hector Mine earthquake ruptured multiple fault segments. For each earthquake we estimated the apparent stress distribution on the fault; for this, we used a shear modulus, μ , dependent on depth, calculated from the velocity models used for the rupture modelling of each earthquake. Also, we calculated the static stress drop distribution using the approach of *Andrews* [1978]. We analyzed the potential energy change, the energy loss (given by the last term of equation (6.2)), and the radiated energy. It is worth mentioning that the values of energy

loss should be interpreted with caution. Energy loss can approximate the fracture energy under certain circumstances. In the figures we plot the negative of this term to compare more easily with the accompanying radiated energy calculation; i.e., the radiated energy will be the sum of potential energy change and energy loss (negative). A negative value of energy loss reflects a positive fracture energy and a positive value of energy loss reflects the situation of stress increasing with some slip occurring (Figure 1-3).

6.5.1 1984 Morgan Hill Earthquake

The 1984 Morgan Hill earthquake was modelled by *Beroza and Spudich* [1988]. This event had a local magnitude of 6.2 and started on April 24, 1984, at 21:15:18.9 UTC, its hypocenter was located near the junctions of the Calaveras and Hayward faults (37.317° N, 121.682° W), at 9 km depth [*Cockerhan and Eaton*, 1987]. Its focal mechanism was right-lateral strike slip, with a strike of 330° , a dip of 85° , and a rake of 180° . The total moment reported was 2.0×10^{18} N-m. From the distribution of the aftershocks, *Cockerhan and Eaton* [1987] suggested that the rupture was unilateral to the southeast. *Beroza and Spudich* [1988] used ground motion data to modelled the rupture history of this earthquake. They assumed variable rupture velocity with an average value of 0.8β , where β is the shear wave velocity, and used the *P*-wave velocity model from *Blumling et al.* [1985] for the region, assuming a Poisson solid for the *S*-wave velocity. Furthermore, they used a rise time of 0.2 s, suggesting that the rupture zone was very narrow, ~ 1 km. The total duration of the rupture was 9.4 s.

This event propagated heterogeneously away from the hypocenter, with an area of highly concentrated slip about 14 km to the southeast of the hypocenter (Figure 6-3) [*Beroza and Spudich*, 1988]. According to *Beroza and Spudich* [1988] the regions of largest slip correspond to a complex left step in the surface trace and had fewer aftershocks than other regions.

For this earthquake, we find that the potential energy change follows the slip distribution, having its highest value at the center of the region of high slip at the southeast. The energy loss distribution mostly present patches of negative values with its largest negative value 15 km away from the hypocenter, at the region of high slip. The seismic energy is high near the hypocenter, but decreases systematically along strike, towards an energy sink where we find the seismic energy is being absorbed, (about 10 km away from the hypocenter). The concentrated source farther along the fault is an area of high energy release. The

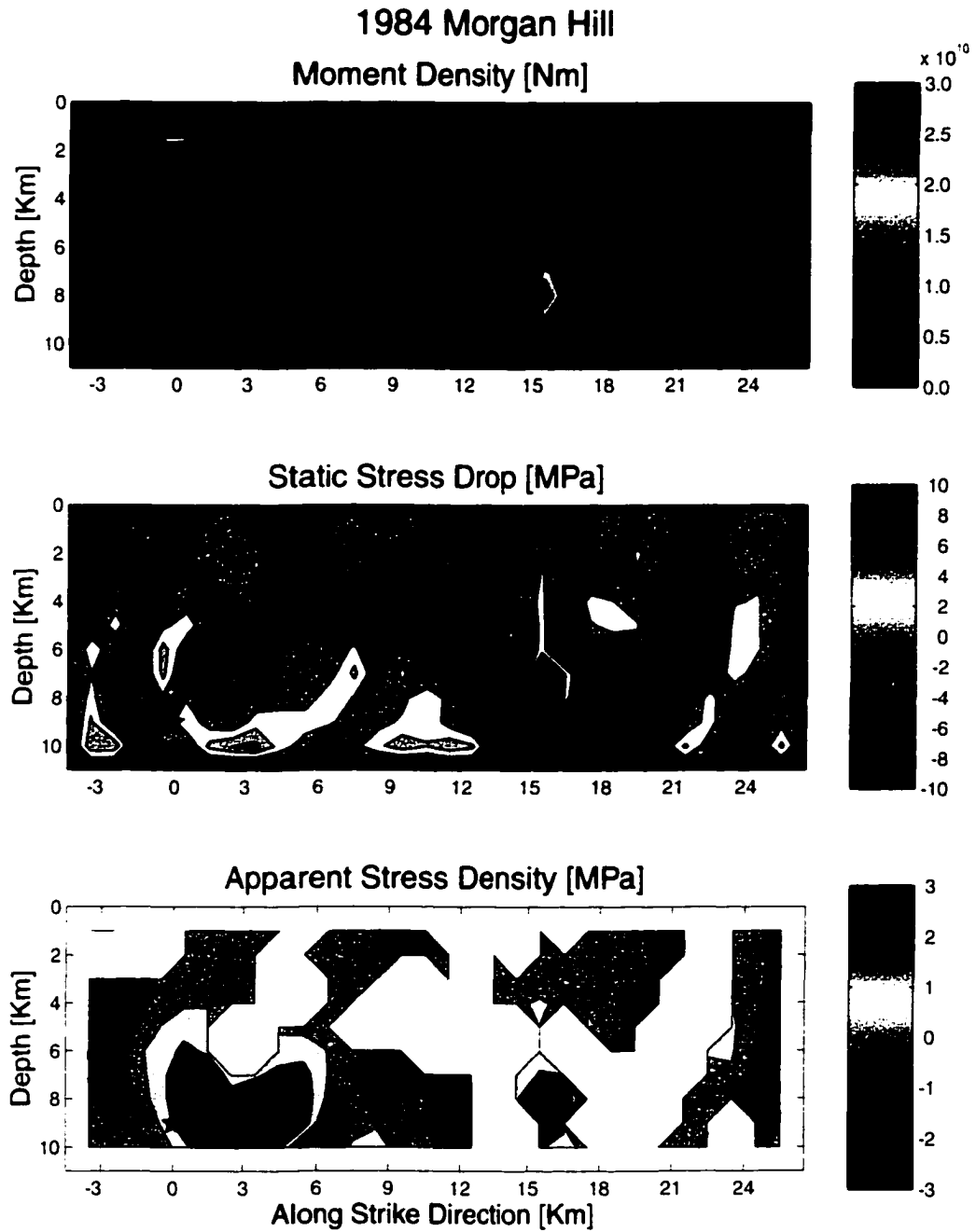


Figure 6-3: 1984 Morgan Hill earthquake. The top panel is the moment density distribution, the center panel is the static stress drop distribution, and the bottom panel is the apparent stress distribution.

largest energy concentrations are located at the center of the high slip regions, which is consistent with *Ide's* [2002] observations. Also, the energy sinks coincide with the edges of these regions, in both directions (Figure 6-4). About 93% of the energy is released from only 14% of the fault. Furthermore, the apparent stress distribution presents two high τ_α patches, located at the high slip regions, in contrast with the energy distribution, these patches are more diffuse (Figure 6-3). There are regions where the stress decreased to negative values that coincide with the energy sink regions. These results agree with the observations of *Beroza and Spudich* [1988] on how the rupture front was slowed down and then proceeded to rupture the region that was resistant to slip, doing it in an energetic fashion. From the static stress drop distribution (Figure 6-3), we observe a close relation of the static stress drop and the slip, with the highest stress drops at the region of high slip, but more interesting is the presence of negative stress drop regions; i.e., regions where the stress increases, surrounding the high slip region located at 15 km away from the hypocenter. This stress increase corresponds to the energy sink regions and negative apparent stress regions. These are slipped only because they were driven to do so by the surrounding areas of high stress drop.

From the rupture model, we obtained a total seismic energy of 3.74×10^{13} J, after 9.9 s. Previously reported values were 1.4×10^{14} J [*Bolt*, 1986] and 2.00×10^{14} J [*Smith et al.*, 1989]. This implies that the value estimated using the rupture model is about four times smaller than the others, which were obtained using ground motion data of near *S*-wave data. The frequency range used in the rupture modelling was between 0.2 and 4.0 Hz [*Beroza and Spudich*, 1988].

6.5.2 1992 Landers Earthquake

The second earthquake modelled was the 1992 Landers earthquake. This event started at 11:57:34.1 UTC on June 28, 1992 in Southern California at 34.20° N latitude, 116.43° longitude, and 4.5 km depth [*Hauksson et al.*, 1993]. It had a moment magnitude of 7.3, with total seismic moment estimates from 7 to 11×10^{19} N-m. The focal mechanism reported by USGS CMT was strike slip with a strike of 343° , a dip of 81° , and a rake of 180° . *Cohee and Beroza* [1994] modelled its rupture distribution along three segments: the southernmost, the Johnson Valley fault, strikes 354° , with a length of 27 km; the second one in the middle, the Homestead Valley fault, is 30-km long, with a strike of 331° ; and the third segment to the north, the Camp Rock-Emerson fault, is 45 km length with a strike

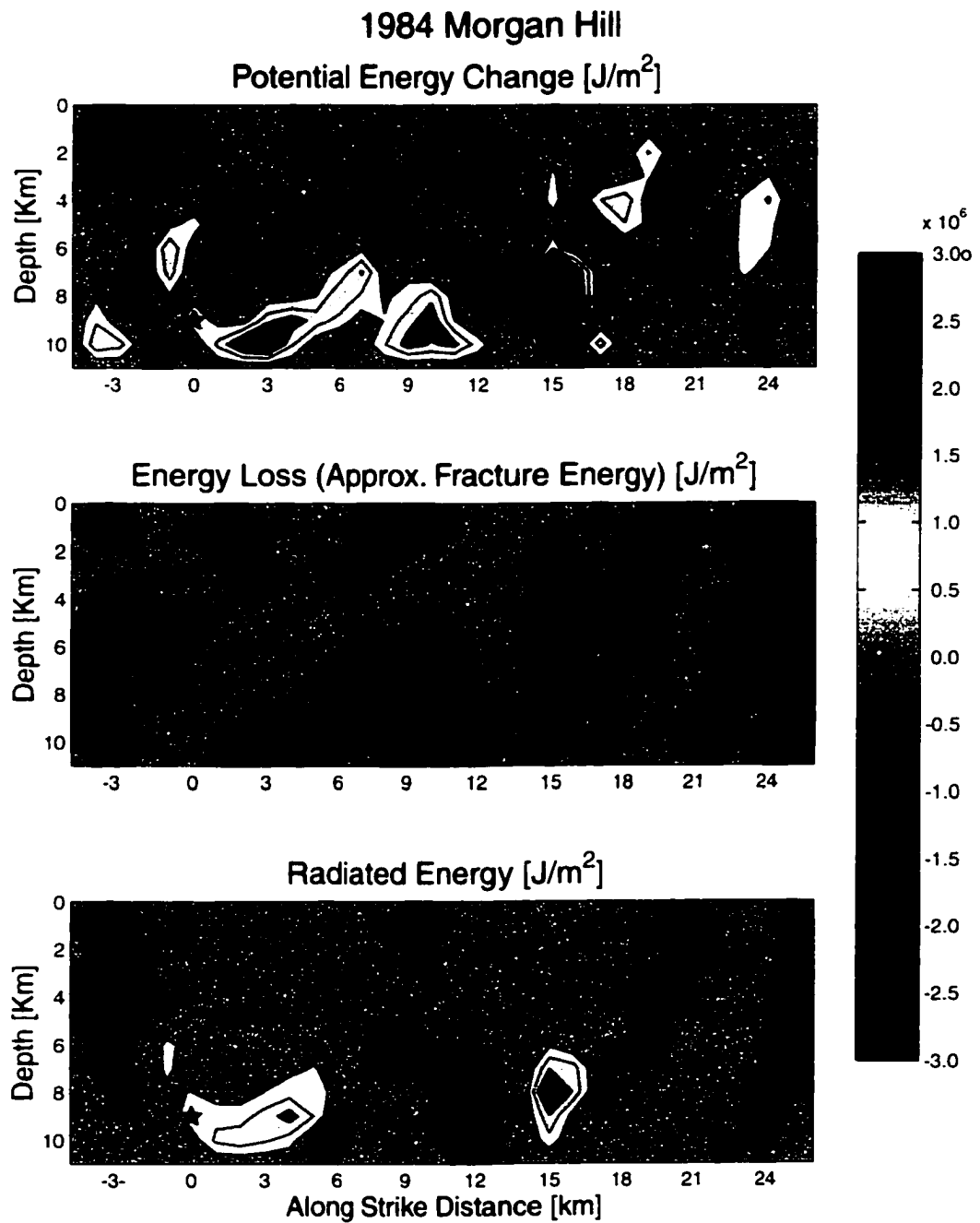


Figure 6-4: 1984 Morgan Hill earthquake. The radiated energy density (bottom panel) can be obtained by summing the potential energy change (upper panel) with the energy loss density (middle panel).

of 332° . *Cohee and Beroza* [1994] assumed variable rupture velocity with an average value of 2.5 km/s. and a rise time of 3 s, and obtained a total duration of the rupture of 22 s; they used the velocity model from *Hauksson et al.* [1993]. A similar result was obtained by *Wald and Heaton* [1994].

The rupture started at the Johnson Valley fault, where *Cohee and Beroza* [1994] obtained low slip ≤ 2 m (Figure 6-5). Then slip propagated to the North, to the Homestead Valley fault, where there was a patch of high slip (as much as 6 m) distributed over a wide region (Figure 6-6), which had low aftershock activity. Finally, the rupture propagated to the Camp Rock-Emerson fault (Figure 6-7), where it had another patch of high slip (as much as 6 m). Along this segment *Cohee and Beroza* [1994] noticed a clear anticorrelation between slip and aftershock activity.

We calculated the radiated energy distribution using the rupture model of *Cohee and Beroza* [1994]. As mentioned before, the rupture model of this earthquake is along three fault segments; for our energy distribution calculation each segment was modelled individually. By doing this we neglect the effects of each segment on the others. We find that for the Johnson Valley fault, close to the hypocenter, both the potential energy change and the energy loss have high values (positive and negative, respectively) in the region of high slip. In fact, these three distributions are well correlated to each other. However, the radiated energy density was modest and centered on the slip patch beneath the hypocenter. There is an energy sink at the northern edge of this region near the end of this fault segment (Figure 6-8). This segment released only 10% of the energy of the entire earthquake. On the Homestead Valley segment, the potential energy change has its highest positive value centered on the high slip region, this is the same situation for the apparent fracture energy. The seismic energy is concentrated at the center of the high slip region. A pronounced energy sink occurs at the northern end of this region, this sink can be understood as the effect of the energy loss dominating in that region (Figure 6-9). Here again a large energy sink occurs at a segment boundary. In the case of this segment, the slip distribution and the radiated energy density distribution are not well correlated, this is possible an effect of the segmentation. This segment released $\sim 60\%$ of the total energy released by this earthquake. On the Camp Rock-Emerson fault, the potential energy change is concentrated at the center of the high slip region. On this segment, the seismic energy distribution is dominated by the potential energy change, given that the energy loss is minimum. The patch with high seismic energy is surrounded by energy sinks (Figure 6-10). This behavior is consistent

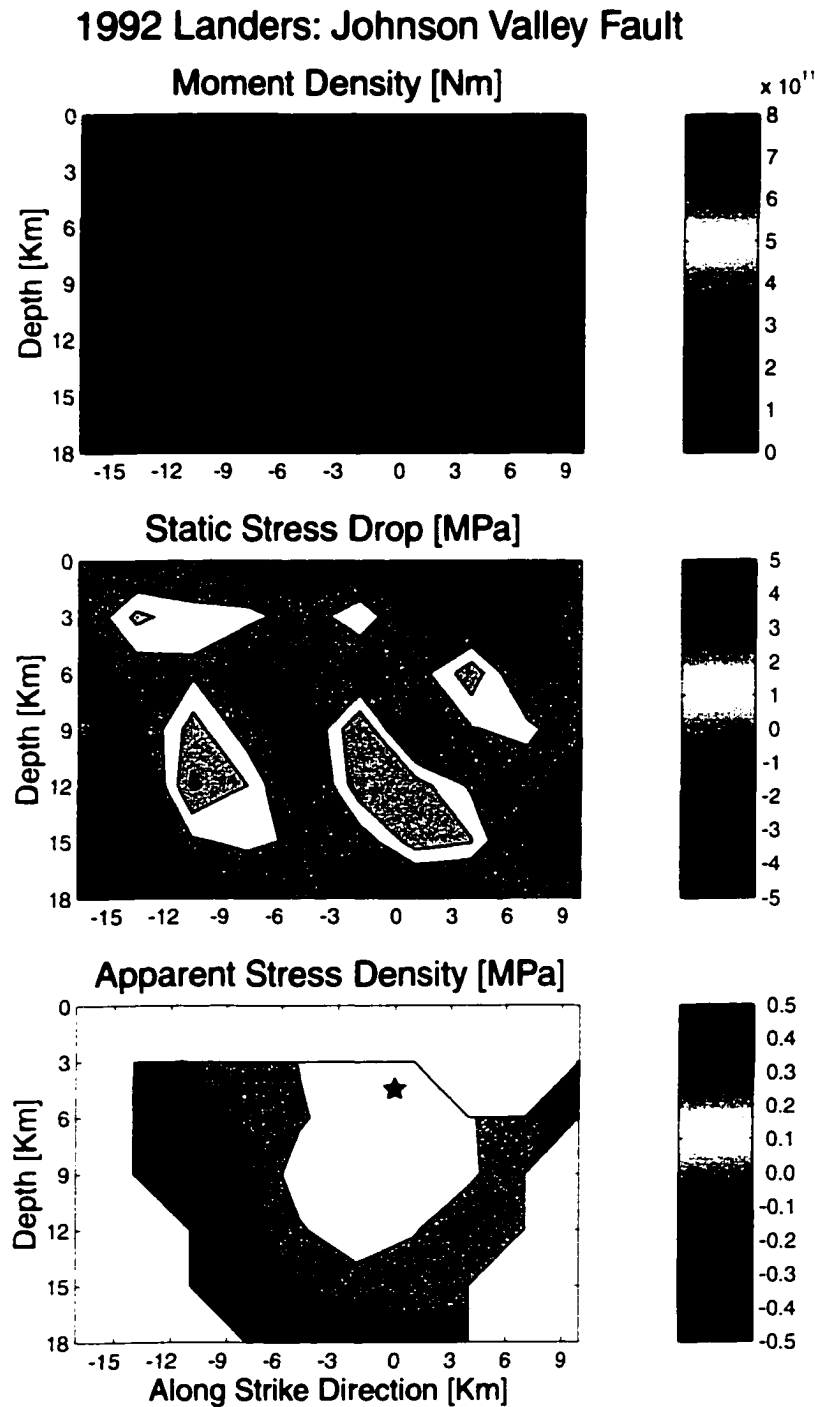


Figure 6-5: 1992 Landers earthquake, Johnson Valley Fault segment. The top panel is the moment density distribution, the center panel is the static stress drop distribution, and the bottom panel is the apparent stress distribution.

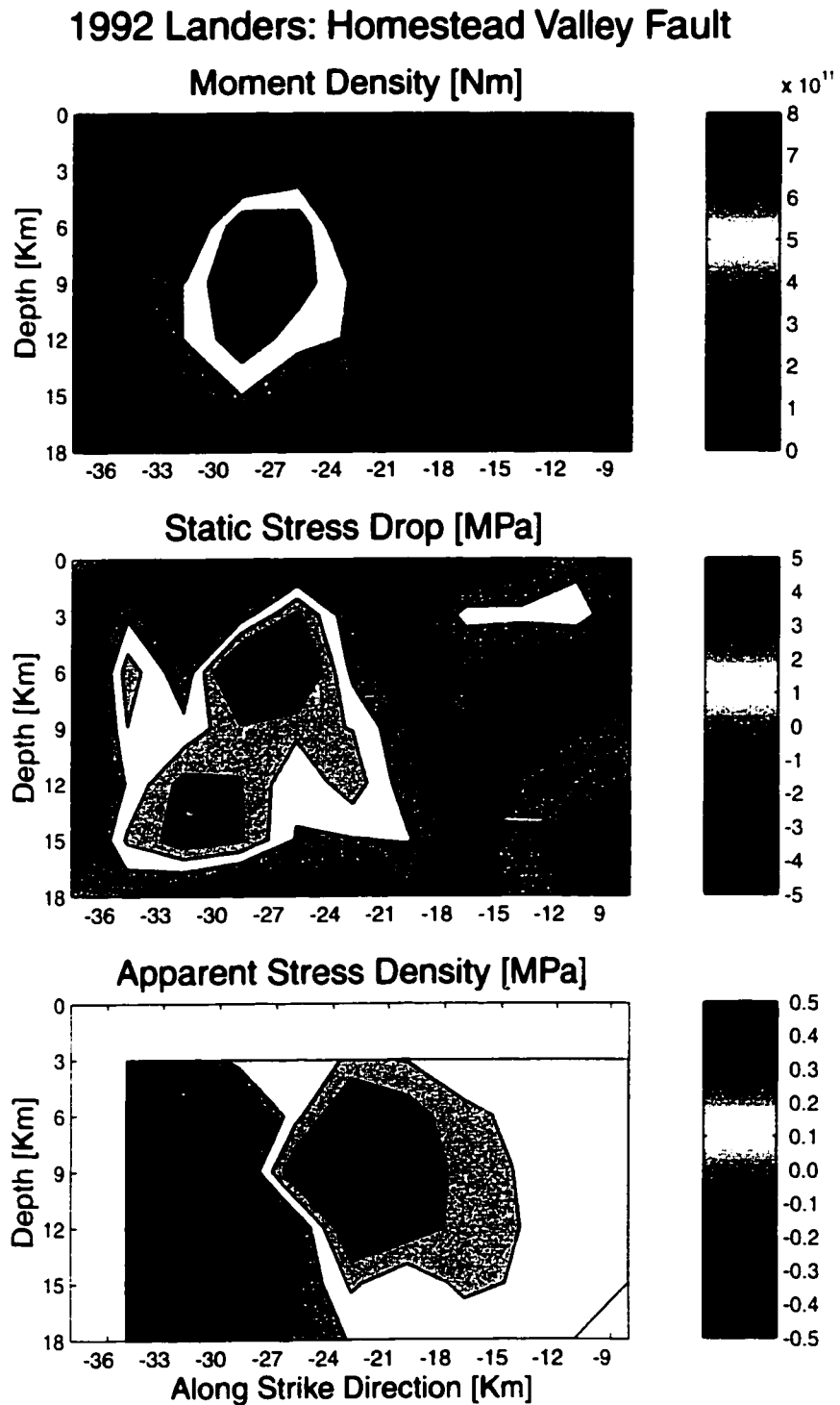


Figure 6-6: 1992 Landers earthquake, Homestead Valley Fault segment. The top panel is the moment density distribution, the center panel is the static stress drop distribution, and the bottom panel is the apparent stress distribution.

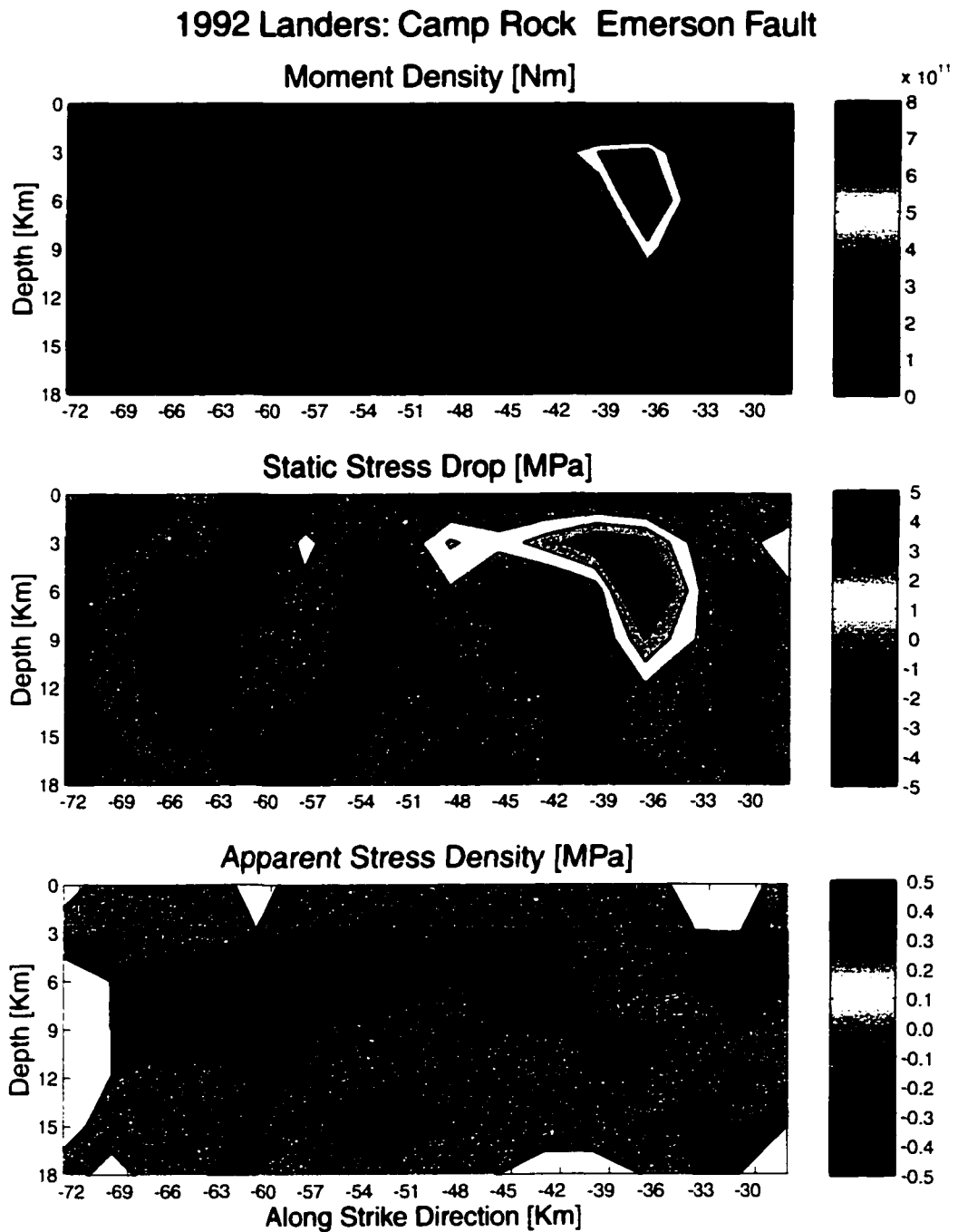


Figure 6-7: 1992 Landers earthquake, Camp Rock-Emerson Fault segment. The top panel is the moment density distribution, the center panel is the static stress drop distribution, and the bottom panel is the apparent stress distribution.

with the findings of *Felzer and Beroza* [1999] who concluded that rupture terminated on this fault segment because it was far from failure prior to the mainshock. This segment released $\sim 30\%$ of the energy. Overall, about 75% of the energy was released by only 14% of the fault, primarily on the Homestead Valley fault.

In this case, the apparent stress was larger in the Homestead Valley fault (Figure 6-6), reaching values of 0.45 MPa. Similar to the Morgan Hill event, there are negative apparent stresses corresponding to the energy sinks. On the Camp Rock-Emerson fault segment, most of the apparent stress is close to zero (Figure 6-7). It was in this segment where the rupture stopped. Having small radiated energy and apparent stress in this fault segment but still having slip occurring suggests that this slip was driven by the dynamic load imposed by the adjacent segment and not because the segment had the conditions for failure. The static stress drop maps the slip distribution. For the Johnson Valley fault the apparent stress and the static stress drop distributions are well correlated (Figure 6-5); however, for the other two segments, the distributions differ greatly (Figures 6-6 and 6-7).

The total energy for this earthquake estimated using the rupture model is 1.34×10^{15} J. Previous results are 1.0×10^{16} J [*Kanamori*, 1994, personal communication in *Singh and Ordaz*, 1994], 10 times larger than the estimated here; and 2.57×10^{16} J [*Mayeda and Walter*, 1996], which is 19 times larger than the former one. The underestimation of the total energy might be as a result of various factors. First, the regional estimates might be higher than the actual value as suggested by *Boatwright et al.* [2002] in their study of the Hector Mine earthquake, reducing this the difference. Another factor is the bandlimited frequency range used in the rupture modelling (0.08 to 0.25 Hz) [*Cohee and Beroza*, 1994]; furthermore, the grid size [*Ide*, 2002] and the fact that the estimation of the radiated seismic energy was done for each segment independently may play an important role in underestimating the seismic energy.

6.5.3 1999 Hector Mine Earthquake

The third event analyzed is the 1999 Hector Mine earthquake that started at 02:46:44 UTC on October 16, 1999, located in Southern California at 34.594° N, 116.271° W, and 6 km depth. It had a moment magnitude of 7.1, a total moment of 4.01×10^{19} N-m, and a strike-slip focal mechanism with a strike of 343° , a dip of 70° , and a rake of 175° , reported from the Berkeley Digital Seismic Network [*Dreger and Kaverina*, 2000].

We used the rupture distribution modelled by *Dreger and Kaverina* [2000], for which

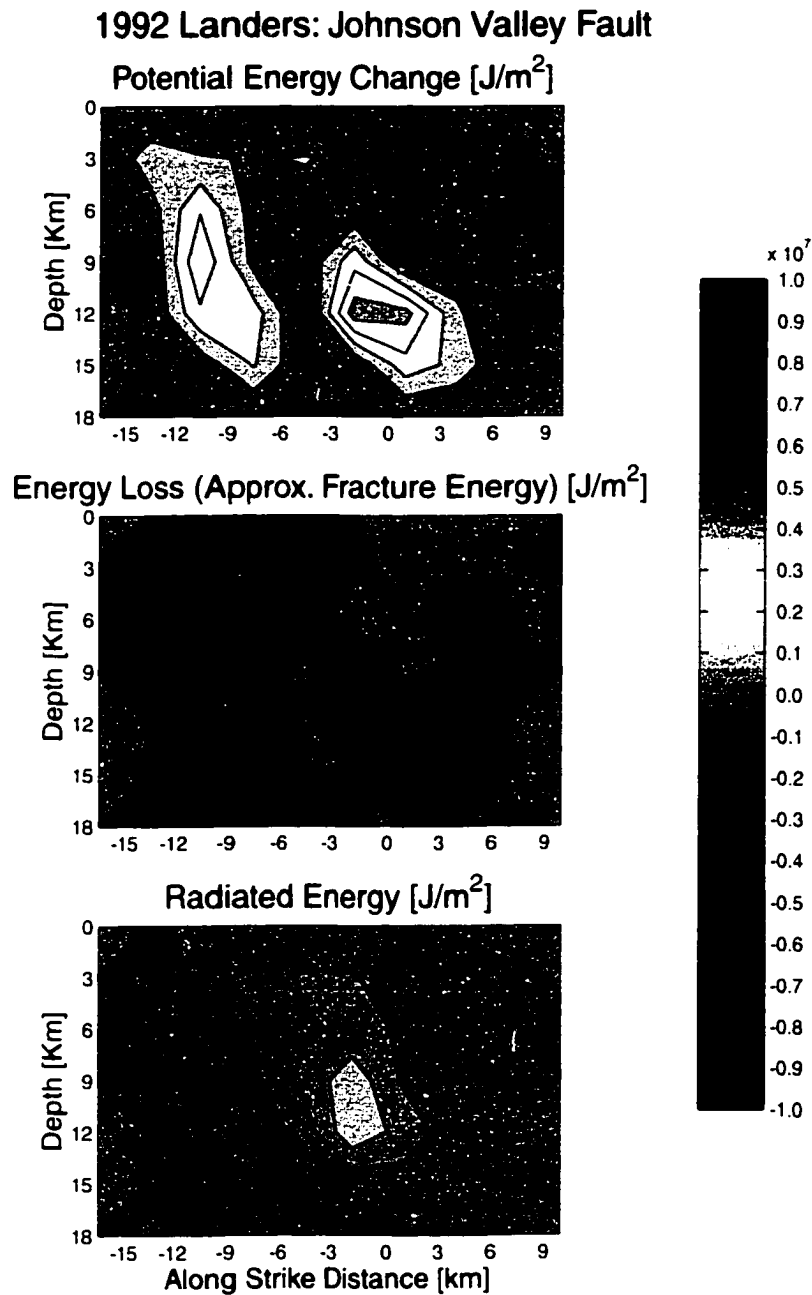


Figure 6-8: 1992 Landers earthquake, Johnson Valley Fault segment. The radiated energy density (bottom panel) can be obtained by summing the potential energy change (upper panel) with the energy loss density (middle panel).

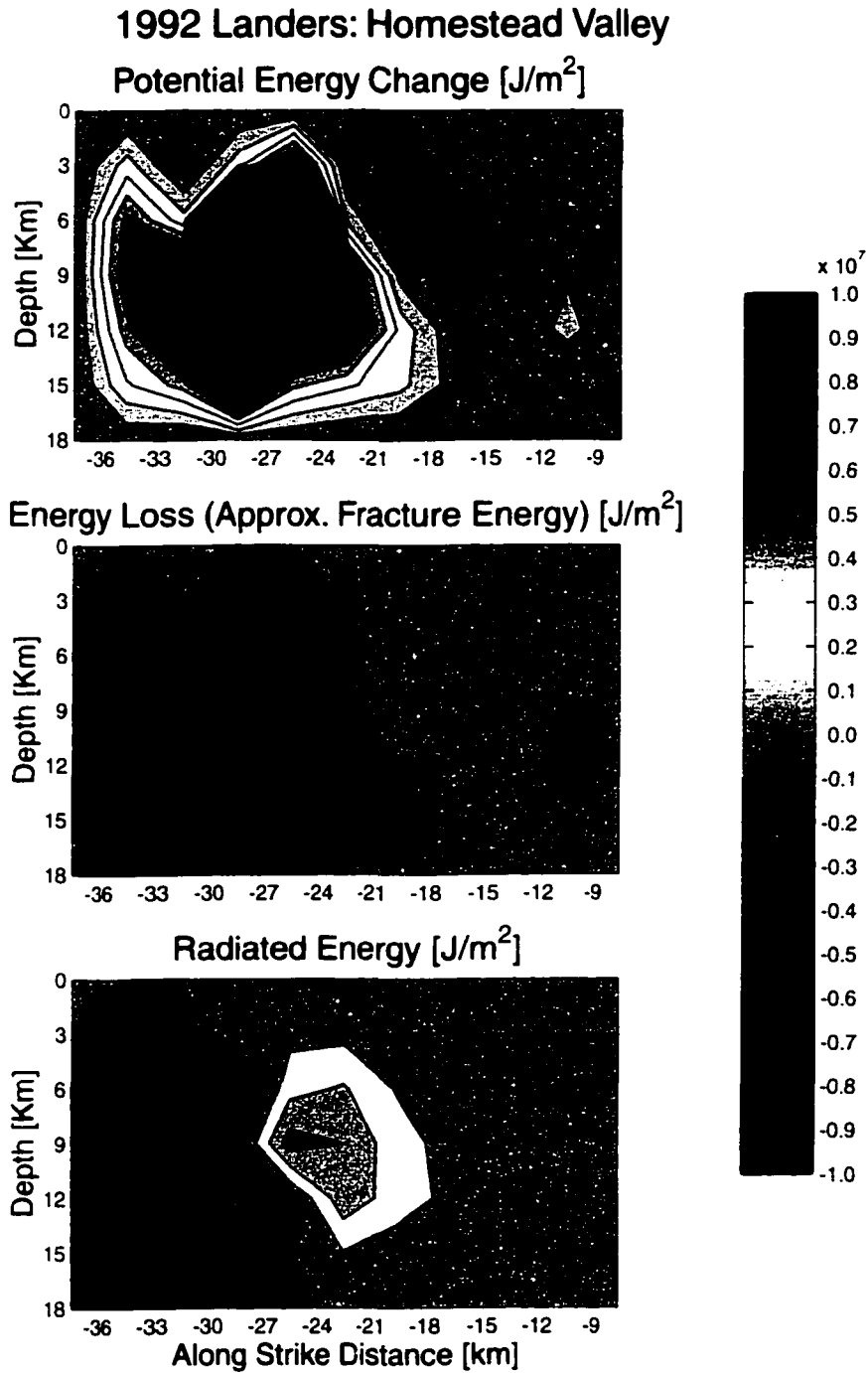


Figure 6-9: 1992 Landers earthquake, Homestead Valley Fault segment. The radiated energy density (bottom panel) can be obtained by summing the potential energy change (upper panel) with the energy loss density (middle panel).

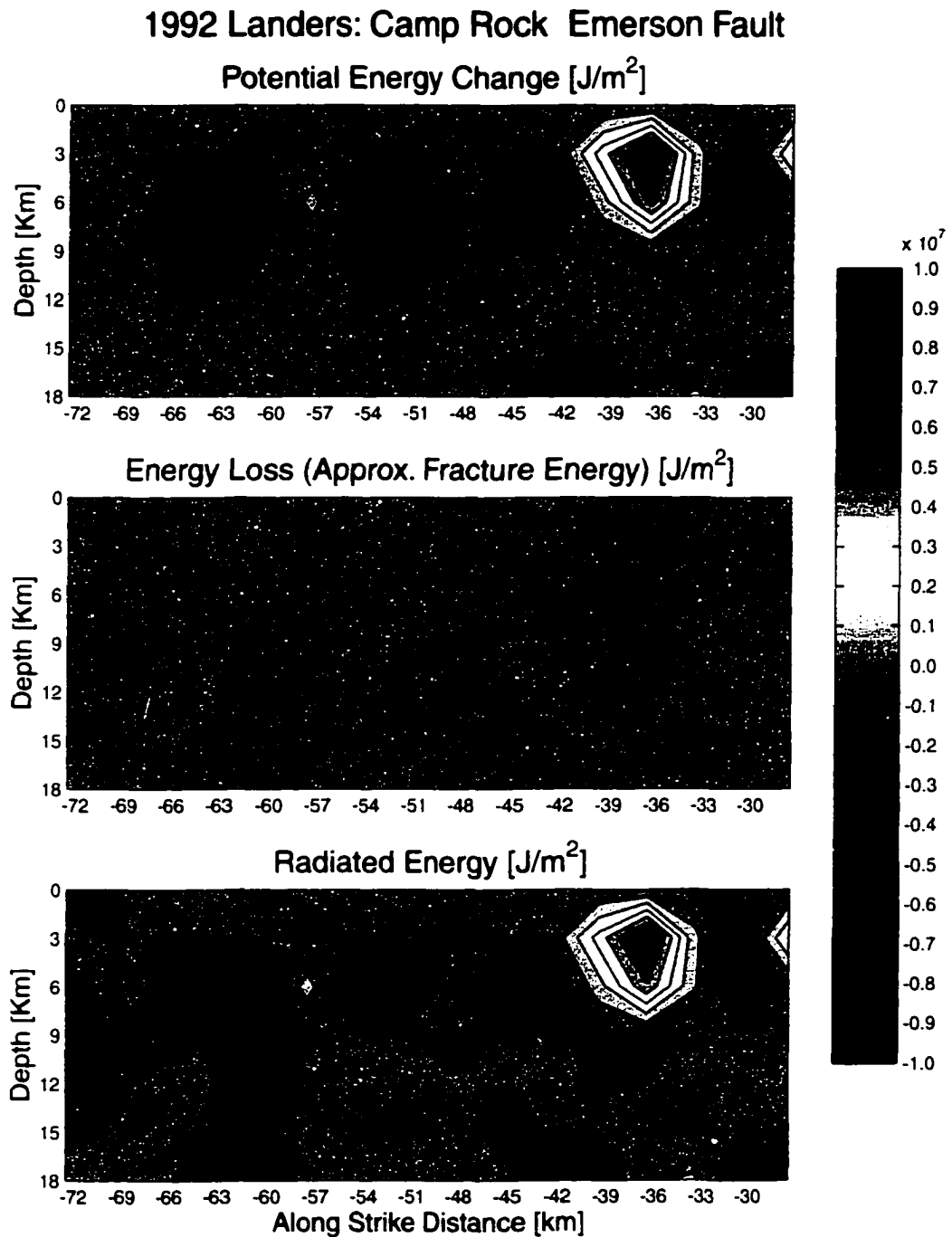


Figure 6-10: 1992 Landers earthquake, Camp Rock-Emerson Fault segment. The radiated energy density (bottom panel) can be obtained by summing the potential energy change (upper panel) with the energy loss density (middle panel).

they assumed a constant rise time of 1.7 s, for a total duration of 16.8 s. They assumed a constant rupture velocity of 2.2 km/s. In this case, we used the velocity model for the crust from *Hauksson et al.* [1993].

Dreger and Kaverina [2000] observed that the slip was bilateral, with most of the slip from 5 to 33 km to the SSE of the hypocenter and high slip region between 11 to 18 km to the NW (Figure 6-11).

From this rupture model, the highest positive values of potential energy change and the largest negative values of energy loss follow the slip distribution. It is important to observe the presence of both positive and negative values for the energy loss distribution (middle panel of Figure 6-12). This distribution is given by the last term of equation (6.2) and represents the situation of stress increasing with some slip occurring (Figure 1-3). This feature dominates in the radiated energy calculation. We observed that similar to the other events, the seismic energy is concentrated at the high slip regions. In this case, the largest energy released is beneath the hypocenter, and most of the energy is released to the SSE, this effect is a result of a patch of high positive values on the energy loss distribution. Also, this event presents an energy sink at the SSE edge of the main region of high slip as a result of the large negative values of the energy loss distribution in this region (Figure 6-12). About 88% of the energy is released by only 16% of the fault.

For this event, the apparent stress is higher close to the hypocenter and it is negative at the energy sink. In contrast to the Morgan Hill and Landers events, its distribution is concentrated at the hypocenter and surrounded by negative values. This observation is similar to the results of *Ide* [2002] for the three events he studied. Also for this event, the static stress drop maps the slip distribution but in this case is not well correlated with the apparent stress.

In this case, *Boatwright et al.* [2002] obtained from regional *S*-wave data a value of 3.3×10^{15} J, and a value of 3.2×10^{15} J from teleseismic *P* wave data; *Venkataraman et al.* [2002] obtained from regional data a value of 3.0×10^{15} J; from previous chapters in this work, using teleseismic *P* waves, we obtained a value of 3.1×10^{15} J. The total energy estimated from the rupture model was 1.38×10^{15} J after 20 s, which is about two times smaller than the regional and teleseismic estimates. In this case, *Dreger and Kaverina* [2000] used data from 0.05 to 5 Hz. Despite the bandlimited nature of the rupture model, the bandwidth used for this event is wider, including most of the seismic energy information. Furthermore, this event was modelled with a constant low rupture velocity using a $1 \times 1\text{-km}^2$

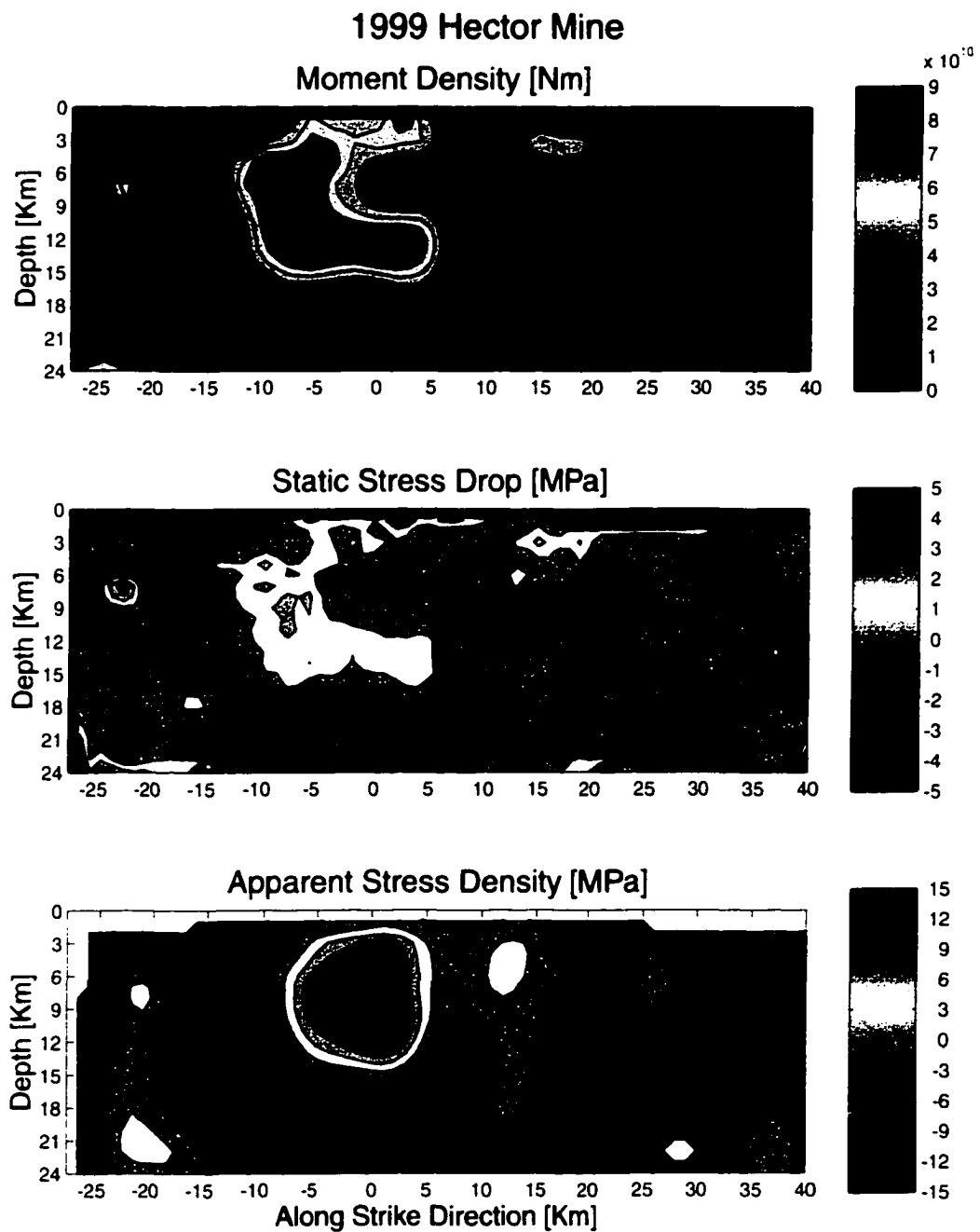


Figure 6-11: 1999 Hector Mine earthquake. The top panel is the moment density distribution, the center panel is the static stress drop distribution, and the bottom panel is the apparent stress distribution.

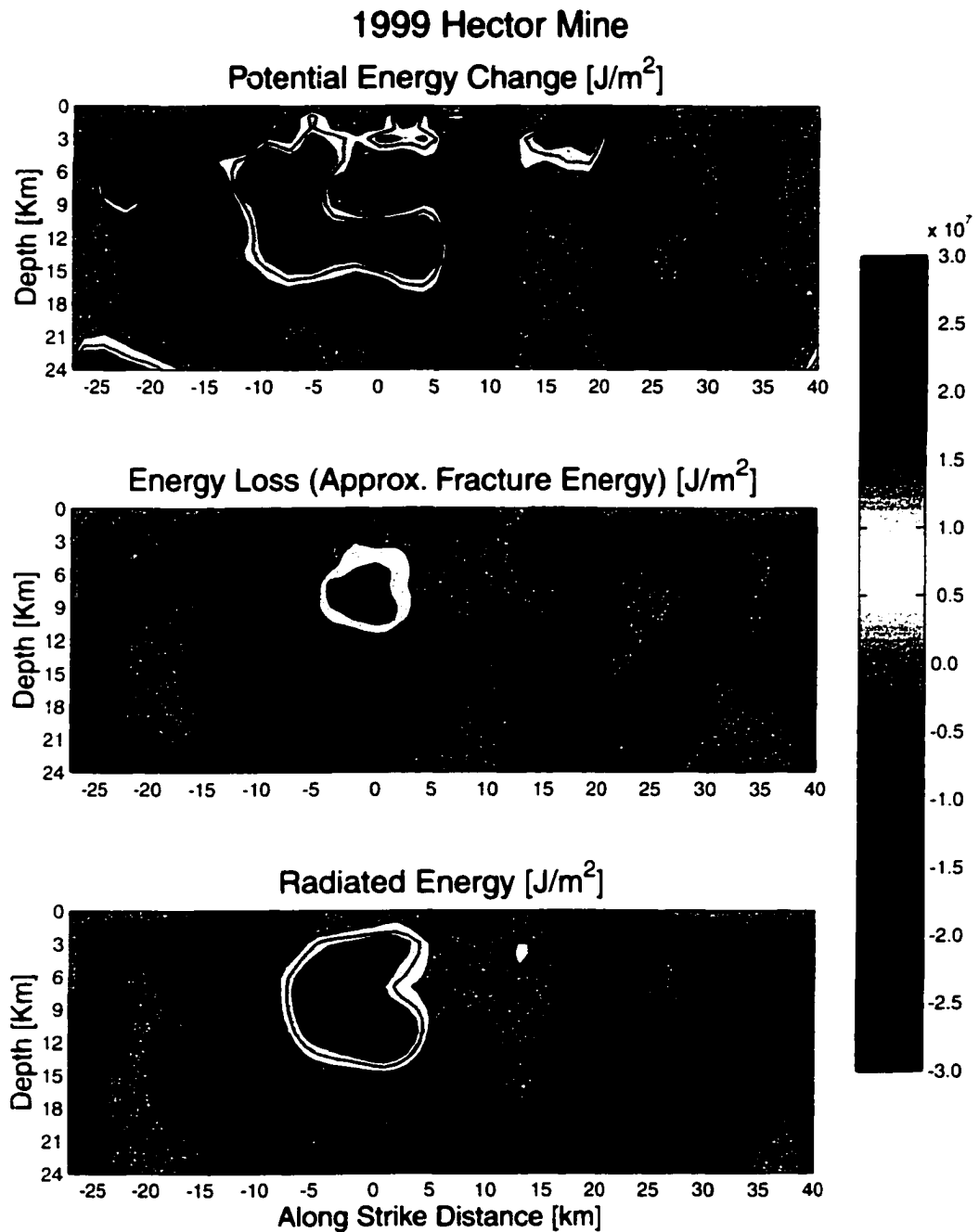


Figure 6-12: 1999 Hector Mine earthquake. The radiated energy density (bottom panel) can be obtained by summing the potential energy change (upper panel) with the energy loss density (middle panel).

grid. These two facts probably help in obtaining a better estimate of seismic energy [Ide, 2002].

6.6 Discussion

The total seismic energy has been related to stress drop and slip in a macroscopic point of view described by the slip-weakening model (Figure 6-2). However, this model does not account for spatial variations in fault characteristics. Following Ide [2002], we analyzed the energy distribution on the fault for the 1984 Morgan Hill, the 1992 Landers, and the 1999 Hector Mine earthquakes. The results suggest that the energy is dissipated according to the frictional properties of the fault. The energy is released mainly at the high slip regions with the highest values of E_s , with regions of largest slip. These high slip regions present at their edges energy sinks or regions of energy absorption. Thus, considerable slip occurs in areas that are absorbing seismic energy. Most of the energy is released from a small portion of the fault, coming mainly from the high slip regions.

In these three earthquakes, the potential energy change, the energy loss, and the radiated energy are of comparable magnitude. Given that energy loss is approximately equal to the apparent fracture energy suggests that fracture energy is of the same order as radiated energy and we cannot neglect it. In fact, the values of energy loss obtained for the 1984 Morgan Hill earthquake are comparable to the fracture energy of 2×10^6 J/m² estimated by Beroza and Spudich [1988]. Also, this is consistent with findings of other authors, such as Guatteri *et al.* [2001] and Ide, [2002], who suggested that the fracture energy is not negligible.

The apparent stress distribution shows that the asperities present the highest values of apparent stress, negative values at the edges of the high slip regions and null values where the rupture stops.

The static stress drop maps the slip distribution, being highest at high slip regions and negative at their edges or between them. The apparent stress was well correlated with the static stress drop for the 1984 Morgan Hill earthquake and for the Johnson Valley fault segment of the 1992 Landers earthquake; however, for the other cases, where fault segmentation is important, this was not the case.

The total E_s is underestimated using the rupture model. Ide [2002] found that the underestimate could be larger when the grid was coarse especially when the rupture velocity

was close to the shear wave velocity. In our analysis, the estimate closest to independently determined estimates of the seismic energy is for the Hector Mine earthquake which was modelled with a low constant rupture velocity of 2.2 km/s. The largest difference is for the Landers earthquake, which was modelled with variable rupture velocity and an average value of 2.5 km/s (plus the grid size is larger (3×3 km)). This under estimation could also be as a result of the lack of high frequency information for the rupture modelling. Since most of the energy is concentrated around and above the corner frequency, the bandlimited nature of the data used in the modelling will miss some energy, especially from high frequencies. The underestimate can be more dramatic for small earthquakes, with large corner frequencies.

There is a clear correlation between the frequency band used in the modelling of the three earthquakes analyzed in the work and the amount of under estimation of E_s . For the 1984 Morgan Hill earthquake, the bandwidth used was from 0.2 to 4.0 Hz; from the total duration the upper limit of the corner frequency is about 0.1 Hz; in this case we are missing some information around the corner frequency, while at high frequencies we are including information from frequencies up to 4 Hz. For our worst case, the 1992 Landers earthquake, the frequency range utilized was from 0.08 to 0.25 Hz. Based on its total duration, the upper limit of the corner frequency is 0.04 Hz. Again, in this case we are missing some information around the corner frequency as well as information at high frequencies, since the highest frequency is only 6 times the corner frequency. For our best scenario, the 1999 Hector Mine earthquake, *Dreger and Kaverina [2000]* used a frequency range between 0.05 and 5 Hz. In this case, the upper limit of the corner frequency is 0.06, which is higher than the lower limit of the frequency range used and two orders of magnitude smaller than the upper limit, so we will be including most of the energy. Other sources for underestimating seismic energy from rupture models are the grid used in the calculation and the effect of segmentation. These two effects could lead to the largest discrepancy observed for the 1992 Landers earthquake.

6.7 Conclusions

The seismic energy can be estimated directly from the seismograms to obtain the total seismic energy released by an earthquake. This value alone will not give us enough information about the source characteristics. Although this technique generally underestimates the total seismic energy, which is probably due to the bandlimited frequency range utilized

in the rupture modelling, it allows us to obtain a spatial distribution of the seismic energy dissipation, leading to the description of important features on the fault such as asperities, energy sinks, or the apparent stress variation on the fault. The seismic energy released is closely related to the slip distribution, being higher at high-slip regions. Energy is also absorbed at the edges of these high-slip regions.

6.8 Acknowledgments

Satoshi Ide for his codes and Martin P. Mai for his help with the rupture models and his code for calculating static stress drop. This research was supported by NSF grant EAR 0208499. Xyoli Pérez-Campos was partially supported by SEP, Mexico and DGAPA, UNAM.

Appendix A

Focal Mechanism Dependence and Scaling: Revisited

The results presented on chapter 2 were obtained before performing the modifications and enhancements to the teleseismic technique, described in chapters 3 and 4. In this appendix, I present the results using an extended dataset, including significant events in 2000 and 2001, and using the updated teleseismic estimation technique.

The question of the focal mechanism dependence of seismic energy is important to resolve since this will be indicative of differing behavior in the rupture processes of strike-slip earthquakes and dip-slip earthquakes. Also, the question of how the apparent stress is scaled with M_0 will tell us if small earthquakes release energy differently than large earthquakes.

Before, we were not able to make a definite conclusion on these matters since the uncertainty in the estimates was very large, and different techniques will produce an estimate up to an order of magnitude different than other technique. After the corrections made in chapters 3 and 4, this problem has been reduced and the uncertainty in the E_s estimate is considerably smaller, allowing us to revisit the question of focal mechanism dependence and scaling.

A.1 Focal Mechanism Dependence

Using 244 events from around the world that occurred between 1992 and 2002, with moment magnitudes between 5.5 and 8.3. We obtained a mean τ_α , for the 108 reverse earthquakes analyzed, of $0.46 + 0.11 / - 0.09$ MPa; of $0.92 + 0.33 / - 0.24$ MPa, for the 67 normal earthquakes; and of $1.52 + 0.59 / - 0.42$ MPa, for the 70 strike-slip events analyzed. Performing

Table A.1: Best Fit Results.

Variable	Estimates (Standard Error)		
	Model 1	Model 2	Model 3
β_0	-2.48(0.84)		
β_1	0.89(0.04)		
β_{0S}		-4.32(0.07)	-3.17(1.68)
β_{0R}		-4.83(0.05)	-3.73(1.08)
β_{0N}		-4.52(0.07)	-0.52(1.90)
β_{1S}			0.94(0.09)
β_{1R}			0.94(0.06)
β_{1N}			0.79(0.10)
RSS	66.38	68.02	77.88
Degrees of freedom	236	239	240

the same statistical analysis described in Chapter 2, we conclude that the three populations are statistically different from each other, with strike-slip events having the highest apparent stress with their mean ~ 3.3 times larger than the reverse events, and only ~ 1.7 times larger than the normal events (Figure A-1).

From the strike-slip population, the event with the smallest apparent stress is recognized as a slow earthquake in chapter 5.

A.2 Scaling of Apparent Stress

We analyzed the events, using equations (2.12), (2.13), and (2.14). The results are shown in Table A.1. We find that for a constant slope equal to one (Equation (2.13)) we can reject the null hypothesis at a 95% confidence level that reverse, normal, and strike-slip events come from the same population. For the full model (Equation (2.14)) we find that strike-slip events scale as $M_0^{0.94}$, reverse events as $M_0^{0.94}$, and normal events as $M_0^{0.79}$ (Figure A-1). An F test between models based on (2.12) and (2.13) reveals that the three populations are inconsistent with mechanism-independent constant apparent stress. Comparing models (2.13) and (2.14), we cannot reject the null hypothesis of the slope being equal one for the strike-slip events, for the normal events, nor for the reverse events.

A.3 Tectonic Setting

So far, we have analyzed all events together. It has been suggested that different tectonic settings might radiate energy differently. It has been argued that ridge transform events were more energetic than others [Choy and Boatwright, 1995], so we separate events into

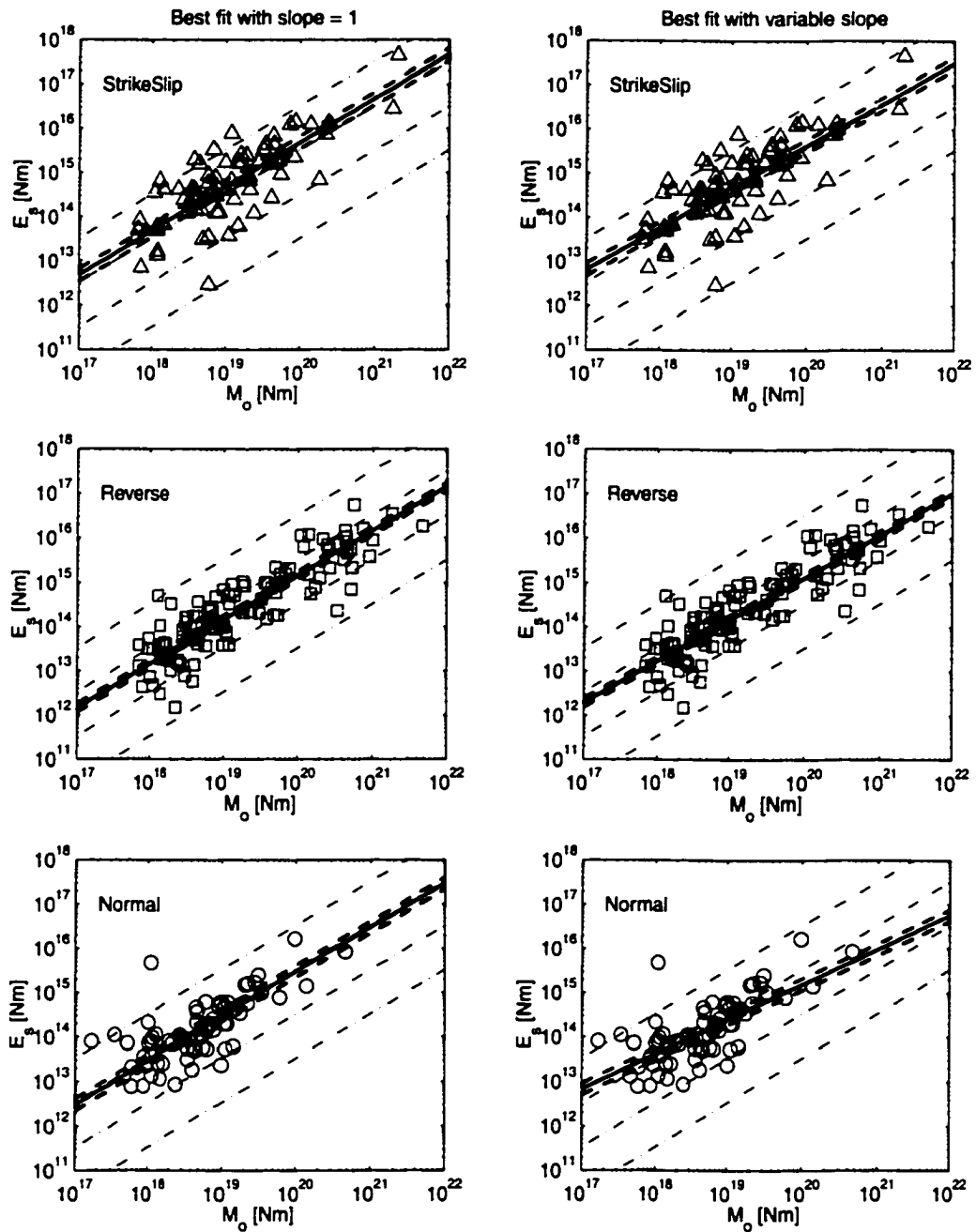


Figure A-1: Best fit for average apparent stress using enhance teleseismic technique. (left) Bootstrap replications for the best fit assuming a fixed slope equal to one and (right) pair-wise bootstrap replications for the best fit, varying both slope and intercept. The solid lines represent the best fit, and the dashed lines indicate the 95% confidence interval for the mean.

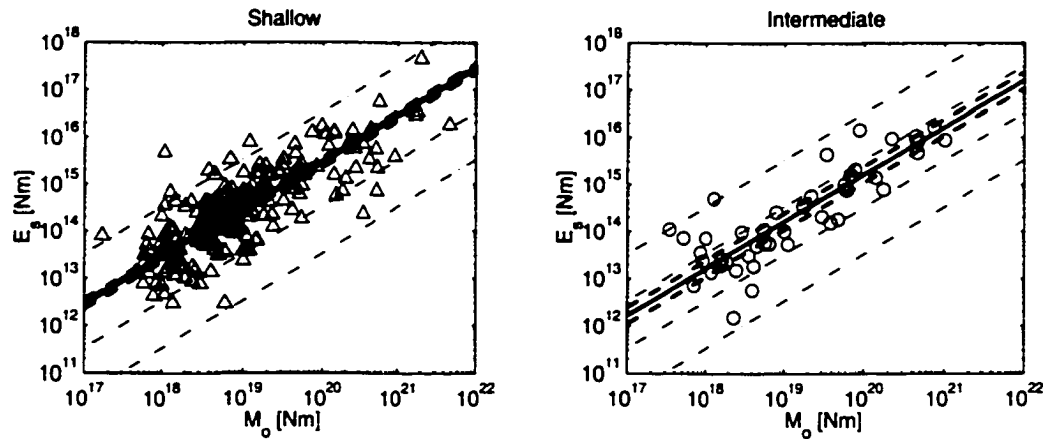


Figure A-2: Continental vs Oceanic. (left) Best fit for continental earthquakes. (right) Best fit for oceanic earthquakes. The solid lines represent the best fit, and the dashed lines indicate the 95% confidence interval for the mean.

different categories and compare their mean apparent stresses.

The first comparison is between continental and oceanic earthquakes. As mentioned in chapter 3, we use the IASP95 velocity model for the continental events and a velocity model with oceanic crust for the oceanic events. We observed that both populations are undistinguishable, having mean apparent stress of $0.97 + 0.35 / - 0.25$ MPa and $0.82 + 0.21 / - 0.17$ MPa, for the continental and the oceanic, respectively (Figure A-2).

The second comparison is between shallow and intermediate earthquakes, considering shallow those at depths shallower than 35 km, and intermediate those with depths between 35 and 70 km. In this case, the intermediate events have a smaller apparent stress ($0.49 + 0.24 / - 0.16$ MPa) than the shallow events ($0.87 + 0.17 / - 0.15$ MPa) (Figure A-3).

The last comparison is between five different tectonic settings for shallow events: subduction ($0.77 + 0.21 / - 0.16$ MPa), collision ($1.29 + 5.46 / - 1.04$), ridge and rise ($0.96 + 1.22 / - 0.54$ MPa), interplate ($1.01 + 0.41 / - 0.29$ MPa), and intraplate ($1.12 + 3.12 / - 0.82$ MPa). Observing that there is no significant difference between the populations (Figure A-4). Populations with small number of events (e.g., collision or intraplate) present a wider distribution for the mean apparent stress. All populations have a wide scatter in apparent stress.

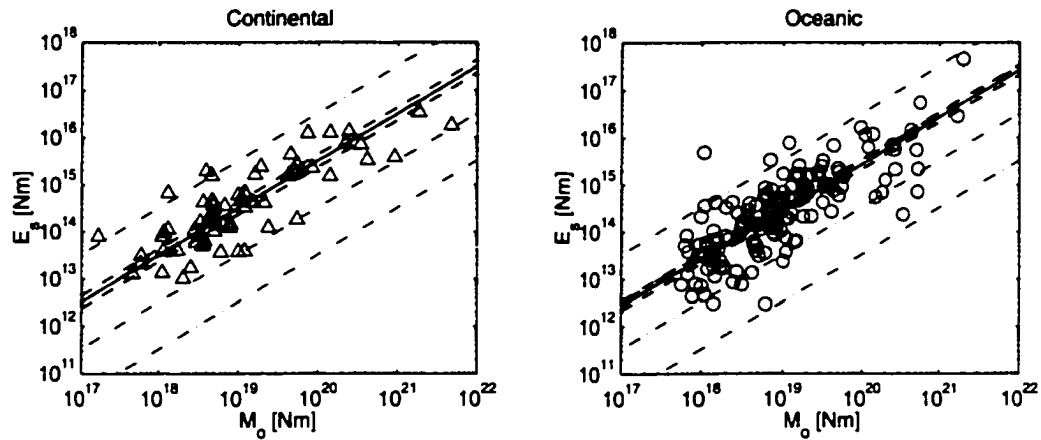


Figure A-3: Shallow vs Intermediate. (left) Best fit for shallow earthquakes (depth ≤ 30 km). (right) Best fit for intermediate depth earthquakes (depth between 30 and 70 km). The solid lines represent the best fit, and the dashed lines indicate the 95% confidence interval for the mean.

A.4 Discussion

We still observe a difference between the mean apparent stress for the three focal mechanisms. The strike-slip events have highest mean apparent stress, ~ 3.3 times larger than the one of reverse events, and only ~ 1.7 times larger than the normal events. The difference has been reduced between the strike-slip events and the reverse events (~ 5 before, chapter 2). This reduction could be a result of the updates in the seismic energy estimation at teleseismic distances described in this thesis. This includes the use of a different attenuation model for subduction zones, where most reverse events occur, and the utilization of a frequency dependent site correction.

We also show no significant difference between the mean apparent stresses of the different populations. For each tectonic setting population we include all three types of mechanism. This suggests that regardless the tectonic setting where they originate, earthquakes radiate energy in the same fashion macroscopically. Any differences would likely be due to local conditions.

Finally, although there is a great range of apparent stress in our observations, we observe no significant systematic scaling of the apparent stress with seismic moment, at least for the range of seismic moments in this study, which suggest that earthquakes behave the same in terms of their stress drop regardless their size.

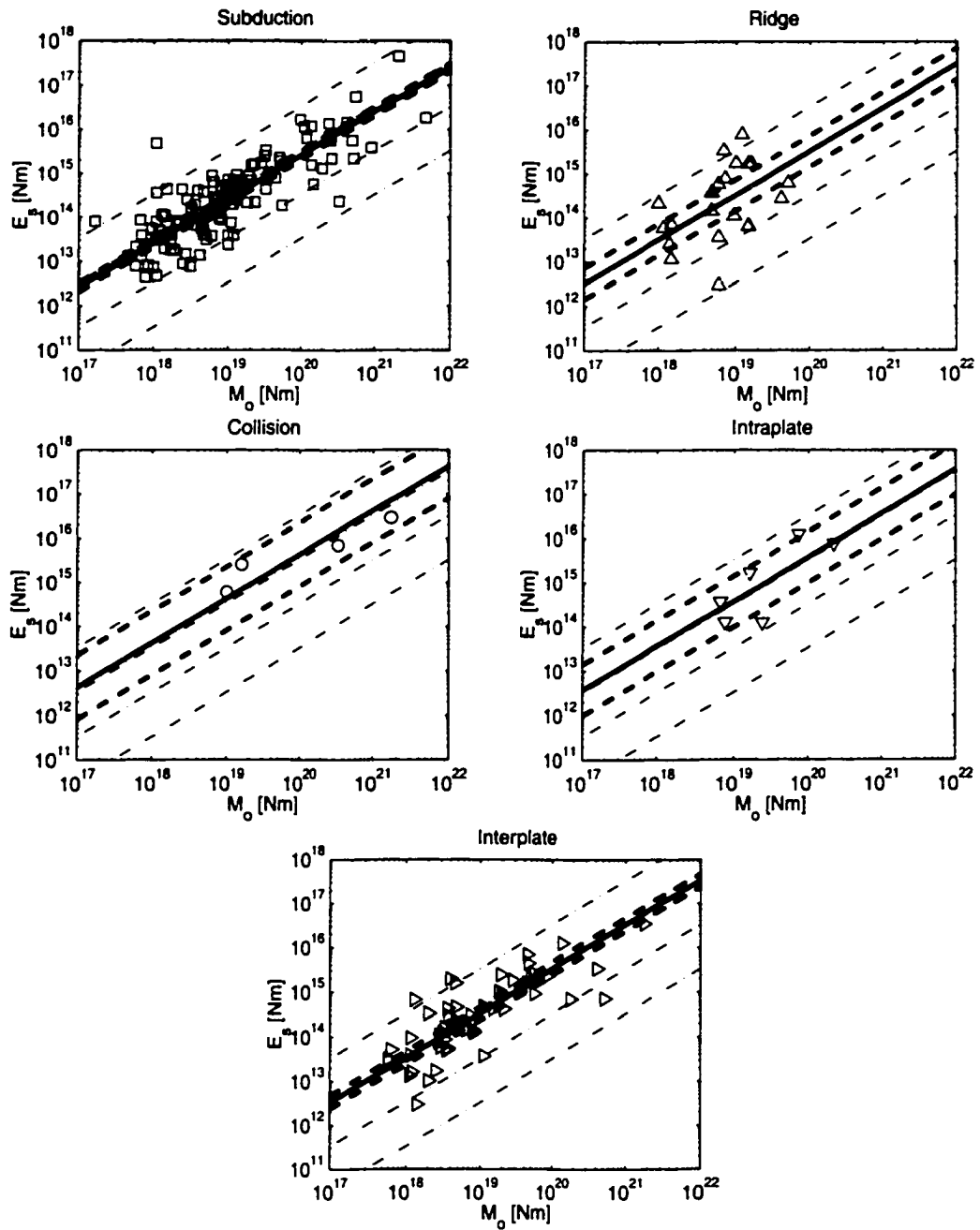


Figure A-4: Tectonic Setting. The solid lines represent the best fit, and the dashed lines indicate the 95% confidence interval for the mean.

Appendix B

Bibliography

- Abe, K. (1979). Size of great earthquakes of 1837-1974 inferred from tsunami data, *J. Geophys. Res.*, **84**, 1561-1568.
- Abercrombie, R. E. (1995). Earthquake source scaling relationships from -1 to 5 M_L using seismograms recorded at 2.5-km depth, *J. Geophys. Res.*, **100**, 24,015-24,036.
- Abercrombie, R. E., M. Antolik, K. Felzer, and G. Ekström (2001). The 1994 Java tsunami earthquake: Slip over a subducting seamount, *J. Geophys. Res.*, **106**, 6595-6607.
- Abercrombie, R. E., and G. Ekström (2001). A reassessment of the rupture characteristics of oceanic transform earthquakes, *J. Geophys. Res.*, (submitted).
- Aki, K. (1967). Scaling law of seismic spectrum, *J. Geophys. Res.*, **72**, 1217-1231.
- Aki, K., and P.G. Richards (1980). *Quantitative Seismology, Theory and Methods*, W.H. Freeman and Company, New York.
- Anderson, J. G., and S. E. Hough. (1984). A model for the shape of the Fourier amplitude spectrum of acceleration at high frequencies, *Bull. Seismol. Soc. Am.*, **74**, 1969-1993.
- Andrews, D. J. (1976). Rupture velocity with finite stress in antiplane strain, *J. Geophys. Res.*, **81**, 3575-3582.
- Andrews, D. J. (1976). Rupture velocity of plain strain shear cracks, *J. Geophys. Res.*, **81**, 5679-5687.
- Andrews, D. J. (1980). Fault impedance and earthquake energy in the Fourier transform domain, *Bull. Seismol. Soc. Am.*, **70**, 1,683-1,698.
- Atkinson, G. M. (1993). Notes on ground motion parameters for eastern North America: duration and H/V ratio, *Bull. Seismol. Soc. Am.*, **83**, 587-596.
- Beeler, N. M., T. F. Wong, and S. H. Hickman (2002). On the expected relationships between apparent stress, static stress drop, effective shear fracture energy, and seismic efficiency, *Bull. Seismol. Soc. Am.*, [submitted]

- Beroza, G. C., and T. Jordan (1990). Searching for slow and silent earthquakes using free oscillations, *J. Geophys. Res.*, **95**, 2485-2510.
- Beroza, G. C., and P. Spudich (1988). Linearized inversion for fault rupture behavior: application to the 1984 Morgan Hill, California earthquake, *J. Geophys. Res.*, **93**, 6275-6296.
- Blumling, P., W. D. Mooney, and W. H. K. Lee (1985). Crustal structure of the southern Calaveras fault zone, central California, from seismic refraction investigations. *Bull. Seismol. Soc. Am.*, **75**, 193-209.
- Boatwright, J. (1980). A spectral theory for circular seismic sources; simple estimates of source dimension, dynamic stress drop, and radiated seismic energy, *Bull. Seismol. Soc. Am.*, **70**, 1-27.
- Boatwright, J. (1985). Characteristics of the aftershock sequence of the Borah Peak, Idaho, earthquake determined from digital recordings of the events, *Bull. Seismol. Soc. Am.*, **75**, 1265-1284
- Boatwright, J., and G. L. Choy (1986). Teleseismic estimates of the energy radiated by shallow earthquakes, *J. Geophys. Res.*, **91**, 2095-2112.
- Boatwright, J., and G. L. Choy (1989) Acceleration spectra for subduction zone earthquakes, *J. Geophys. Res.*, **94**, 15,541-15,553.
- Boatwright, J., G. L. Choy, and L. C. Seekins (2002). Regional estimates of the radiated seismic energy, *Bull. Seismol. Soc. Am.*, **92**, 1241-1255.
- Boatwright, J., and J. B. Fletcher (1984). The partition of radiated energy between *P* and *S* waves, *Bull. Seismol. Soc. Am.*, **74**, 361-376.
- Bolt, B. A. (1986). Seismic energy release over a broad frequency band, *Pageoph.*, **124**, 919-930.
- Boore, D. M., (1996). SMSIM-Fortran programs for simulating ground motions from earthquakes: version 1.0. U.S. Geol. Surv. *Open-File Rept.* **96-80A**, **96-80-B**, 69 pp.
- Boore, D. M., and W. B. Joyner (1997). Site amplifications for generic rock sites. *Bull. Seismol. Soc. Am.*, **87**, 327-341.
- Bracewell, R.N. (1986). *The Fourier Transform and its Applications*, McGraw-Hill, New York.
- Brune, J. N. (1996). Particle motions in a physical model of shallow angle thrust faulting, *Earth Planet. Sci. Lett.*, **105**, L197-L206.
- Castro, R. R., J. G. Anderson, and S. K. Singh (1990). Site response, attenuation and

- source spectra of S waves along the Guerrero, Mexico subduction zone, *Bull. Seismol. Soc. Am.*, **80**, 1481-1503.
- Castro, R. R., L. Trojani, G. Monachesi, M. Mucciarelli, and M. Cattaneo (2000). The spectral decay parameter κ in the region of Umbria-Marche, Italy, *J. Geophys. Res.*, **105**, 23,811-23,823.
- Chen and Atkinson (2002). Global comparison of earthquake source spectra, *Bull. Seismol. Soc. Am.*, **92**, 885-895.
- Choy, G.L., and J. Boatwright (1995). Global patterns of radiated seismic energy and apparent stress, *J. Geophys. Res.*, **100**, 18,205-18,226.
- Choy, G.L., and V. F. Cormier (1986). Direct measurement of the mantle attenuation operator from broadband P and S waveforms, *J. Geophys. Res.*, **91**, 7326-7342.
- Cleveland, W. S. (1993). Visualizing data, Hobart Press, 360 pp.
- Cocco and Rovelli (1989). Evidence for the variation of stress drop between normal and thrust faulting earthquakes in Italy, *J. Geophys. Res.*, **94**, 9399-9416.
- Cockerhan, R. S., and J. P. Eaton (1987). The earthquake and its aftershocks, April 24 through September 30, 1984, *U. S. Geol. Surv. Bull., The Morgan Hill, California, Earthquake of April 24, 1984*, USGS Bull., **1639**, 15-28.
- Cohee B. P., and G. C. Beroza (1994). Slip distribution of the 1992 Landers earthquake and its implications for earthquake source mechanics, *Bull. Seismol. Soc. Am.*, **84**, 692-712.
- Courboux, F., J. Virieux, and D. Gilbert (1996). On the use of simulated annealing method and cross-validation theory for deconvolution of seismograms, *Bull. Seismol. Soc. Am.*, **86**, 1187-1193.
- Dahlen, F. A. (1976). The balance of energy in earthquake faulting, *Geophys. J. R. Astron. Soc.*, **48**, 239-261.
- Day, S. M. (1982). Three-dimensional simulation of spontaneous rupture: the effect of nonuniform prestress, *Bull. Seismol. Soc. Am.*, **72**, 1881-1902.
- Dreger, D., and A. Kaverina (2000). Seismic remote sensing for the earthquake source process and near-source strong shaking: a case study of the October 16, 1999 Hector Mine earthquake, *Geophys. Res. Lett.*, **27**, 1941-1944.
- Efron, B., and R. J. Tibshirani (1993). *An Introduction to the Bootstrap*, Chapman and Hall, New York.
- Felzer, K. R., and G. C. Beroza (1999). Deep structure of a fault discontinuity, *Geophys. Res. Lett.*, **26**, 2121-2124.

- García Jiménez, D. (2001). *Atenuación sísmica. Aplicación a terremotos intrapaca en México Central, Ph. D. Thesis*, Facultad de Ciencias Físicas, Universidad Complutense de Madrid.
- Guatteri, M., P. Spudich, and G. C. Beroza (2001). Inferring rate and state friction parameters from a rupture model of the 1995 Hyogo-ken Nanbu (Kobe) earthquake, *J. Geophys. Res.*, **106**, 26511-26522.
- Gutenberg, B., and C. F. Richter (1942). Earthquake magnitude, intensity, energy and acceleration, *Bull. Seismol. Soc. Am.*, **32**, 163-191.
- Gutenberg, B., and C. F. Richter (1956). Earthquake magnitude, intensity, energy and acceleration (second paper), *Bull. Seismol. Soc. Am.*, **46**, 105-145.
- Haskell, N. A. (1964). Total energy and energy spectral density of elastic wave radiation from propagating faults, *Bull. Seismol. Soc. Am.*, **54**, 1811-1841.
- Haskell, N. A. (1966). Total energy and energy spectral density of elastic wave radiation from propagating faults. Part II. A statistical source model, *Bull. Seismol. Soc. Am.*, **56**, 125-140.
- Hauksson, E., L. M. Jones, K. Hutton, and D. Eberhart-Phillips (1993). The 1992 Landers earthquake sequence: seismological observations, *J. Geophys. Res.*, **98**, 19,835-19-858.
- Hough, S. E., J. G. Anderson, J. Brune, F. Vernon III, J. Berger, J. Fletcher, L. Haar, T. Hanks, and L. Baker (1990). Attenuation near Anza, California, *Bull. Seismol. Soc. Am.*, **78**, 672-692.
- Huang, H., and T. Teng. (1999). An evaluation on H/V ratio vs. spectral ratio for site-response estimation using the 1994 Northridge earthquake sequence, *Pure appl. geophys.*, **156**, 631-649.
- Humphrey, J. R. Jr., and J. G. Anderson (1992). Shear-wave attenuation and site response in Guerrero, Mexico, *Bull. Seismol. Soc. Am.*, **81**, 1622-1645.
- Ida, Y.. (1972). Cohesive force across the tip of a longitudinal shear crack Griffith's specific surface energy, *J. Geophys. Res.*, **84**, 3796-3805.
- Ide, S. (2002). Estimation of radiated energy of finite-source earthquake models, *Bull. Seismol. Soc. Am.*, [submitted].
- Ide, S., and G. C. Beroza (2001). Does apparent stress vary with earthquake size?, *Geophys. Res. Lett.*, **28**, 3349-3352.
- Ide, S., G. C. Beroza, S. G. Prejean, and W. L. Ellsworth (2001). Earthquake scaling down to $M1$ observed at 2 km depth in the Long Valley Caldera, California, *J. Geophys. Res.*, [submitted].

- Ide, S., and M. Takeo (1997). Determination of constitutive relations of fault slip based on seismic wave analysis *J. Geophys. Res.*, **102**, 27,379-27,391.
- Iida, K., D. C. Cox, and G. Pararas-Carayannis (1967). Preliminary catalog of tsunamis occurring in the Pacific Ocean, *U. S. Geological Survey Professional Paper*, Report: P 0400-B, pp.67-10
- Iglesias, A., V. M. Cruz-Atienza, N. M. Shapiro, S. K. Singh, and J. F. Pacheco (2001). Crustal structure of south-central Mexico estimated from the inversion of surface-wave dispersion curves using genetic and simulated annealing algorithms, *Geofísica Internacional*, **40**, 181-190.
- Ihmlé, P. F., and T. H. Jordan (1994) Teleseismic search for slow precursors to large earthquakes, *Science*, **266**, 1547-1551.
- Ihmlé, P. F. (1996) Monte Carlo slip inversion in the frequency domain: Application to the 1992 Nicaragua slow earthquake, *Geophys. Res. Lett.*, **23**, 913-916.
- Joyner, W. B., R. E. Warrick, and T. E. Fumal (1981). The effect of Quaternary alluvium on strong ground motion in the Coyote Lake, California, earthquake of 1979, *Bull. Seismol. Soc. Am.*, **71**, 1333-1349.
- Kanamori, H. (1972). Mechanism of tsunami earthquakes, *Phys. Earth Planet. Interiors*, **6**, 346-359
- Kanamori, H., and T. H. Heaton (2000). Microscopic and macroscopic physics of earthquakes, *GeoComplexity and the Physics of Earthquakes*, J. B. Rundle, D. L. Turcotte, and W. Klein (Editors), *Geophys. Monogr. Ser.*, **120**, 147-163.
- Kanamori, H., and M. Kikuchi (1993). The 1992 Nicaragua earthquake: A slow earthquake associated with subducted sediments, *Nature* **361**, 714-716.
- Kanamori, H., J. Mori, E. Hauksson, T. H. Heaton, L. K. Hutton, and L. M. Jones (1993). Determination of earthquake energy release and ML using terrascope, *Bull. Seismol. Soc. Am.*, **83**, 330-346.
- Kanamori, H., and G. S. Stewart (1976). Mode of the strain release along the Gibbs fracture zone, Mid-Atlantic Ridge, *Phys. Earth Planet. Inter.* **11**, 312-332.
- Kennett, B. L. N. (1991). IASPEI 1991 seismological tables, *Research School of Earth Sciences Australian National University*, 167 pp.
- Kikuchi, M., and Y. Fukao (1988). Seismic wave energy inferred from long-period body wave inversion, *Bull. Seismol. Soc. Am.*, **78**, 1707-1724.
- Kirkpatrick, S., C. D. Gelatt Jr., and M. P. Vecchi (1983). Optimization by simulated annealing, *Science*, **220**, 671-680.

- Kostrov, B. V. (1974). Seismic moment and energy of earthquakes and seismic flow of rock, *Izv. Earth Phys.*, **1**, 23-40.
- Lermo and Chávez-García (1993). Site effect evaluation using spectral ratios with only one station, *Bull. Seismol. Soc. Am.*, **83**, 1574-1594.
- Mai, P.M., and G.C. Beroza (2000). Source scaling properties from finite-fault rupture models, *Bull. Seismol. Soc. Am.*, **90**, 605-614.
- Mayeda, K., and W. R. Walter (1996). Moment, energy, stress drop, and source spectra of western United States earthquakes from regional coda envelopes, *J. Geophys. Res.*, **101**, 11,195-11,208.
- McGarr, A. (1984). Scaling of ground motion parameters, state of stress, and focal depth, *J. Geophys. Res.*, **89**, 6969-6979.
- McGarr, A. (1999). On relating apparent stress to the stress causing earthquake fault slip, *J. Geophys. Res.*, **104**, 3003-3011.
- McGarr, A., and J. B. Fletcher (2000). A method for mapping apparent stress and energy radiation applied to the 1994 Northridge earthquake fault zone, *Geophys. Res. Lett.*, **27**, 1953-1956.
- McGarr, A., and J. B. Fletcher (2001). A method for mapping apparent stress and energy radiation applied to the 1994 Northridge earthquake fault zone-revisited, *Geophys. Res. Lett.*, **28**, 3529-3532.
- McGuire, J. J., P. F., Ihmlé, P. F., and T. H. Jordan (1996). Time domain observations of a slow precursor to the 1994 Romanche transform earthquake, *Science*, **274**, 82-85.
- Mikumo, T. (1981) A possible rupture process of slow earthquakes on a frictional fault, *Geophys. J. R. astr. Soc.*, **65**, 129-153.
- Mori, J., R. Abercrombie, and H. Kanamori (2000) Stress drops and radiated energies of aftershocks of the 1994 Northridge, California earthquake, *J. Geophys. Res.*, , submitted.
- Newman, A. V., and E. A. Okal (1998). Teleseismic estimates of radiated seismic energy: The E/M_0 discriminant for tsunami earthquakes, *J. Geophys. Res.*, **103**, 26,885-26,898.
- Ni, S., J. N. Brune, G. Choy, J. G. Anderson, and Y. Zeng (1999). Local and teleseismic estimates of radiated energy and apparent stress from the Chichi, Taiwan earthquake: Evidence for inertial detachment of the hanging wall from the foot wall in thrust faulting, *EOS, transaction, Am. Geophys. Union*, **v**, p.
- Okal, E., and L. M. Stewart (1982). Slow earthquakes along oceanic fracture zones: evidence

- for asthenospheric flow away from hotspots?, *Earth and Planetary Science Letters*, **57**, 75-87.
- Ordaz, M., and S. K. Singh (1992). Source spectra and spectral attenuation of seismic waves from Mexican earthquakes, and evidence of amplification in the hill zone of Mexico City, *Bull. Seismol. Soc. Am.*, **82**, 24-43.
- Ordaz, M., S. K. Singh, E. Reinoso, J. Lermo, J. M. Espinosa, and T. Dominguez (1988). The Mexico earthquake of September 19, 1985 - Estimation of response spectra in the lake bed zone of the Valley of Mexico, *Earthquake Spectra*, **4**, 815-834.
- Orowan, E. (1960). Mechanism of seismic faulting, *Geol. Soc. Am. Mem.*, **79**, 323-345.
- Pérez-Campos, X., and G.C. Beroza (2001). Mechanism dependent scaling of radiated seismic energy, *J. Geophys. Res.*, **106**, 11,127-11,136.
- Polet J., and H. Kanamori (2000). Shallow subduction zone earthquakes and their tsunami-genic potential, *Geophys. J. Int.* **142**, 684-702.
- Prejean, S. G., and W. L. Ellsworth (2001). Observations of earthquake source parameters and attenuation at 2 km depth in the Long Valley Caldera, eastern California, *Bull. Seismol. Soc. Am.*, **91**, 165-177.
- Prozorov, A. G., and J. A. Hudson (1983). Creepex variation before strong earthquakes, *Computation Seismology* **15**, 27-36.
- Pulido, N., and K Irikura (2000). Estimation of dynamic rupture parameters from the radiated seismic energy and apparent stress, *Geophys. Res. Lett.*, **27**, 3945-3948.
- Quaas, R., J. A. Otero, S. Medina, J. M Espinosa, H. Aguilar, and M. González(1993). *Base nacional de datos de sismos fuertes, Catálogo de estaciones acelerogáficas 1960-1992*, Sociedad Mexicana de Ingeniería Sísmica, AC.
- Rice, J. A. (1995) *Mathematical Statistics and Data Analysis, 2nd ed.*, Duxbury, Boston, Mass.
- Rudinicki, J. W., and L. B. Freund (1981) On energy radiation from seismic sources, *Bull. Seismol. Soc. Am.*, **71**, 583-595.
- Scholz, C.H. (1990). *The Mechanics of Earthquakes and Faulting*, Cambridge University Press, New York.
- Shapiro, N. M., S. K. Singh, and J. Pacheco (1998) A fast and simple diagnostic method for identifying tsunamigenic earthquakes, *Geophys. Res. Lett.*, **25**, 3911-3914.
- Shearer, P. M. (1994) Global seismic event detection using a matched filter on long-period seismograms, *J. Geophys. Res.*, **99**, 13,713-13,725.

- Shi, J., P. G. Richards, and W. Kim (2000). Determination of seismic energy from L_g waves, *Bull. Seismol. Soc. Am.*, **90**, 483-493.
- Shoja-Taheri, J., and J. G. Anderson (1988). The 1978 Tabas, Iran, earthquake: an interpretation of the strong motion records, *Bull. Seismol. Soc. Am.*, **78**, 142-171.
- Singh, S. K., et al. (1988). The Mexico Earthquake of September 19, 1985 - A study of amplification of seismic waves in the Valley of Mexico with respect to a hill zone site, *Earthquake Spectra*, **4**, 653-673.
- Singh, S. K., and M. Ordaz (1994) Seismic energy release in mexican subduction zone earthquakes, *Bull. Seismol. Soc. Am.*, **84**, 1533-1550.
- Singh, S. K., R. Quass, M. Ordaz, F. Mooser, D. Almora, M. Torres, and R. Vásquez (1995) Is there truly a "hard" rock site in the Valley of Mexico?, **22**, 481-484.
- Smith, K. D., J. N. Brune, and K. F. Priestley (1989) Seismic energy, spectrum, and the Savage and Wood inequality for complex earthquakes, **22**, 481-484.
- Stein S., and A. Pelayo (1991) Seismological constraints on stress in the oceanic lithosphere, *Phil. Trans. R. Soc. Lond. A*, **337**, 53-72.
- Street R. L., R. B. Herrman, and O. W. Nuttli (1975). Special characteristics of the L_g wave generated by central United States earthquakes, *Geophys. J. R. Astron. Soc.*, **41**, 51-63.
- Tarantola, A., and B. Valette (1982). Generalized non-linear inverse problems solved using the least squares criterion, *Rev. Geophys.*, **20**, 219-232.
- Thatcher, W., and T. C. Hanks (1973). Source parameters of southern California earthquakes, *J. Geophys. Res.*, **78**, 8547-8576.
- Theodulidis, N, P. Y. Bard, R. Archuleta, and M. Bouchon (1996). Horizontal-to-vertical spectral ratio and geological conditions; the case of Garner Valley downhole array in Southern California, *Bull. Seismol. Soc. Am.*, **86**, 306-319.
- Vassilou and H. Kanamori (1982). The energy release in earthquakes, *Bull. Seismol. Soc. Am.*, **72**, 371-387.
- Venkataraman, A., L. Rivera, and H. Kanamori (2002). Radiated energy from the October 16, 1999 Hector Mine Earthquake: Regional and teleseismic estimates, *Bull. Seismol. Soc. Am.*, **92**, 1256-1265.
- Wald, FD. J., and T. H. Heaton (1994). Spatial and temporal distribution of slip for the 1992 Landers, California earthquake, *Bull. Seismol. Soc. Am.*, **84**, 668-691.
- Wald, FD. J., T. H. Heaton, and K. W. Hudnut (1996). The slip history of the 1994

- Northridge, California, earthquake determined from strong motion, teleseismic, GPS, and leveling data, *Bull. Seismol. Soc. Am.*, **86**, S49-S70.
- Weisberg, S. (1985). *Applied Linear Regression, 2nd ed.*, John Wiley, New York.
- Wyss, M., and J. N. Brune (1968). Seismic moment, stress, and source dimensions for earthquakes in the California-Nevada region, *J. Geophys. Res.*, **73**, 4681-4694.
- Yuncha, Z. A., and F. Luzon (2000). On the horizontal-to-vertical spectral ratio in sedimentary basins, *Bull. Seismol. Soc. Am.*, **90**, 1101-1106.